University of Potsdam
Faculty of Mathematics and Natural Sciences
Institute of Environmental Science and Geography

Alfred Wegener Institute
Helmholtz-Centre for Polar and Marine Research

Master Thesis

Carbon storage, Carbon degradation and sediment transport mechanisms in a changing coastal thermokarst landscape
-
Case study for a land - near shore transect in the Teshekpuk Lake Region, Alaska, USA

Master Program:
Geoecology

Submission Date:
16.11.2023

Submitted by: Frieda Giest

Matriculation Number: 809935

E-Mail: giest1@uni-potsdam.de

1st Supervisor: Dr. Jens Strauss

2nd Supervisor: Prof. Dr. Guido Grosse

Table of Contents

List of figures

List of tables

Abstract

One impact of climate change is the rapid warming of the Arctic, resulting in the thawing of permafrost and associated processes like thermokarst. This leads to the development of thermokarst features, like thermokarst lakes, thermokarst lagoons, and drained thermokarst lake basins. Since permafrost is one of the largest climate sensitive carbon reservoirs of the world, its thaw can possibly lead to the release of substantial amounts of greenhouse gases, thus further exacerbating climate warming. To predict future impacts of permafrost thaw it is of interest to understand how the characteristics of the soils change with a changing permafrost landscape.

The aim of this master thesis is the comparison of different landscape features in a dynamic coastal thermokarst landscape, focusing on three main objectives: (1) the quantification and characterization of organic carbon, (2) the sedimentological and depositional characterization, and (3) the quantification of the mercury content in the profiles. The analysis involves six cores, ranging from 12 to 219 cm in length, from six different landscape units within a land-sea transect in Alaska. A multi-proxy approach, including a hydrochemical, a geochronological, a sedimentological, a biogeochemical, and a bio-marker analysis was used to analyse the samples in the laboratory. The results show variations in the total organic carbon (TOC) content within the profiles and across the different landforms. The highest TOC contents were measured in the sediments of the drained thermokarst lake basin and the thermokarst lake. Sites influenced by saltwater have significantly lower TOC contents than the sites not influenced by saltwater, with the semi-drained lagoon and the marine deposits showing the lowest TOC contents. The biomarker analysis indicates a higher level of organic matter degradation in saltwater influenced soil profiles and fresh undegraded organic matter in the thermokarst lake and drained thermokarst lake basin deposits. Moreover, it shows a varying degree of aquatic influence on the source of organic matter in the deposits of the different landscape units. Additionally, the biomarker indices (average chain length, P_{aq}, P_{wax}) reveal significant differences between the saltwater influenced deposits and the deposits not influenced by saltwater, as well as between the unfrozen and frozen profiles. The sedimentological and depositional characterization shows different characteristics of the grain size distribution across the different soil profiles, with coarser grain sizes in the upland permafrost deposits and finer lacustrine deposits in the thermokarst deposits. The analysis of the profile of the semi-drained lagoon shows deposits similar to upland permafrost samples in the deeper layers and to thermokarst deposits in the upper layer. The quantification of mercury in the soil samples shows higher contents in the thermokarst deposits compared to the upland

permafrost profile, with the highest mean mercury content in the thermokarst lake deposits, indicating an increased accumulation of mercury with higher input of organic matter and with permafrost thaw.

Zusammenfassung

Eine Folge des Klimawandels ist die starke Erwärmung der Arktis, die zu tauenden Permafrostböden und zu einem verstärkten Auftreten von damit verbundenen Prozessen wie Thermokarst führt. Dadurch kommt es zu einer Ausbreitung von Thermokarst-Landschaften, die unter anderem aus Thermokarst-Seen, Thermokarst-Lagunen und drainierte Thermokarst-See-Becken bestehen. Permafrostböden sind einer der größten, klimasensitiven Kohlenstoffspeicher der Erde, wodurch das Tauen dieser Böden potenziell zur Freisetzung erheblicher Mengen an Treibhausgasen führen kann, was den Klimawandel weiter verstärken würde. Um zukünftige Auswirkungen von großflächigem Permafrost-Tau einschätzen zu können, ist es von großem Interesse zu verstehen, wie sich die Eigenschaften der Böden mit den Veränderungen der Permafrost-Landschaften verändern.
Das Ziel dieser Masterarbeit ist der Vergleich verschiedener Landschaftseinheiten in einer dynamischen, von Thermokarst beeinflussten Küstenlandschaft. Der Fokus liegt dabei auf den drei folgenden Zielen: (1) die Quantifizierung und Charakterisierung des organischen Kohlenstoffs, (2) die sedimentologische Charakterisierung und (3) die Quantifizierung des Quecksilbergehalts in den Bodenprofilen. Die Analyse umfasst insgesamt sechs Bodenprofile (Kerne) mit einer Länge zwischen 12 und 219 cm, aus sechs verschiedenen Landschaftseinheiten innerhalb eines Land-Meer-Transekts in Alaska. Zur Analyse der Proben im Labor wurde ein Multiproxy-Ansatz gewählt, der eine hydrochemische, eine geochronologische, eine sedimentologische, eine biogeochemische und eine Biomarker-Analyse umfasste. Die Ergebnisse zeigen, dass der Gehalt an organischem Kohlenstoff (TOC) innerhalb der Bodenprofile und zwischen den verschiedenen Landschaftsformen variiert. Die höchsten TOC-Gehalte wurden in den Sedimenten des drainierten Thermokarst-See-Beckens und des Thermokarst-Sees gemessen. Die salzwasserbeeinflussten Standorte wiesen niedrigere TOC-Gehalte auf als die nicht salzwasserbeeinflussten Standorte, wobei die niedrigsten TOC-Gehalte in den Ablagerungen der halbdrainierten Lagune und der marinen Probe gemessen wurden. Die Biomarker-Analyse deutet auf ein höheres Degradationslevel der organischen Substanz in den salzwasserbeeinflussten Bodenprofilen hin. Dagegen wiesen die entsprechenden Indizes auf frische organische Substanz in den Ablagerungen des Thermokarst-Sees und des drainierten Seebeckens hin. Darüber hinaus zeigte sich ein unterschiedlicher Grad an aquatischem Einfluss auf den Ursprung des organischen Materials in den Ablagerungen der verschiedenen Landschaftseinheiten. Die entsprechenden Biomarker Indizes (Durchschnittliche Kohlenstoff-Kettenlänge, P_{aq}, P_{wax}) zeigen außerdem signifikante Unterschiede zwischen den salzwasserbeeinflussten und nicht salzwasserbeeinflussten Ablagerungen, sowie zwischen den

ungefrorenen und den gefrorenen Profilen. Die sedimentologische Charakterisierung zeigt unterschiedliche Merkmale der Korngößenverteilung in den verschiedenen Bodenprofilen, mit gröberem Material in den Permafrost-Ablagerungen und feinerem Material in den Thermokarst-Ablagerungen. Das Profil der halbdrainierten Lagune weist Ablagerungen auf, die in den unteren Schichten denen der Permafrost-Ablagerungen und in den oberen Schichten denen der Thermokarst-Ablagerungen ähneln. Die Quantifizierung von Quecksilber in den Bodenproben zeigt höhere Werte in den Thermokarst-Ablagerungen im Vergleich zum Permafrost-Profil, mit den höchsten Quecksilbergehalten in den Thermokarst-See Ablagerungen, was auf eine verstärkte Akkumulation mit höherem Eintrag von organischem Material und durch das Auftauen von Permafrost hinweist.

1. Introduction

1.1. Scientific Relevance of Permafrost

Climate change represents one of the most pressing global environmental challenges of our time. Especially the Arctic regions are currently changing rapidly, since they experience among the highest rates of impacts from climate change (IPCC, 2019; IPCC, 2022). Surface air temperatures in the Arctic increased double to four times the rate the global mean air temperature did over the last decades, a phenomenon referred to as Arctic amplification (Cohen et al., 2020; Rantanen et al., 2022; Richter-Menge et al., 2017). The local drivers of this amplification include the decrease of sea ice and snow cover, resulting in a decreased albedo, and a shift of cloudiness over the Arctic (Richter-Menge et al., 2017). Moreover, there are remote drivers which contribute to the amplification, including an increased total water vapor in the Arctic atmosphere, due to an increased evapotranspiration and atmospheric moisture transport from the mid-latitudes and tropics, and accelerated heat from the atmosphere and the ocean (Cohen et al., 2020). As a result, surface temperatures in the Arctic during the winters in 2016 and 2018 were 6 °C above the average temperatures between 1981-2010 (IPCC, 2019).

One impact as well as a reinforcing mechanism of this warming is the thaw of permafrost, which underlies large areas of the Arctic (IPCC, 2022). In some locations a total increase of 2-3 °C in the last 30 years was found within 10-20 m soil depth (IPCC, 2019). Permafrost has been identified as a large reservoir of organic carbon and with climate change a major vulnerable carbon source in the earth system (Jones et al., 2012). It is estimated that soils in permafrost regions store approximately 1400-1600 Gt carbon, which is about twice as much currently present in the atmosphere (Schuur & Mack, 2018). As permafrost thaws the soils can turn from a carbon sink to a carbon source (Schuur et al., 2009). With increased temperatures there is an acceleration of microbial activity and thus an increased decomposition of organic carbon in the deposits, leading to the release of greenhouse gases in form of carbon dioxide and methane to the atmosphere, and thus further exacerbating climate change (Miner et al., 2022). Another consequence of permafrost thaw is the change of the landscape, for example due to melting ground ice causing surface subsidence and the development of thermokarst features (Grosse et al., 2013). Around 20 % of the permafrost regions are affected by thermokarst processes, including thermokarst lakes and drained lake basins (Grosse et al., 2013; Olefeldt et al., 2016). In a coastal environment an increased coastal and riverbank erosion, sea level rise, higher water temperatures, and a reduced sea ice cover can lead to the flooding of thermokarst lakes and drained thermokarst lake basins by ocean water and the formation of

thermokarst lagoons (Jenrich et al., 2021; Schirrmeister et al., 2018). They add another complex setting of biogeochemical and hydrochemical processes in the transitional stage between terrestrial and marine environments, to the already diverse thermokarst landscapes (Schirrmeister et al., 2018). Moreover, permafrost thaw can possibly lead to the release and relocation of mercury (Hg). Permafrost soils sequestered Hg bound in organic matter over centuries, and it is estimated that the amount of Hg retained in permafrost regions is twice as high as in all other soils, the atmosphere, and the ocean combined (Schuster et al., 2018). Therefore, Hg is a notable environmental concern in the Arctic region for both humans and wildlife, as elevated exposure can impact human health and have negative effects on the ecosystems (Rydberg et al., 2010; Smith-Downey et al., 2010).

1.2. Research Objectives

This study, framed within the context of these climatic and environmental transformations, aims to assess the biogeochemical characteristics of different thermokarst features within a dynamic coastal thermokarst landscape. I focused on comprehending the transitional dynamics between terrestrial and marine permafrost and thermokarst, particularly concerning the influence of factors such as the inundation of seawater on soil properties. The detailed objectives of this master thesis are as follows:

(1) **Quantification and Characterization of Organic Carbon:** This objective seeks to determine the quantity, quality, and source of the organic carbon within the sediments. It aims to address the questions:

(I) How much organic carbon is stored in the different landscape units compared to one another?

(II) What are the primary sources of the organic carbon, and how do they differ across the landscape units?

(III) What is the potential quality of the organic carbon, and can distinctions in the levels of organic carbon degradation within the sample sites of the transect be identified?

(2) **Sedimentological and Depositional Characterization:** This objective aims to provide a sedimentological description of the six soil profiles, addressing the question:

(I) What are the predominant depositional processes characterizing the different landscape features, and where do similarities and differences in these processes across the landscape units exist?

(3) **Quantifying Mercury Content:** This objective focusses on the quantification of the mercury content in the soil profiles and addresses the following questions:

(I) Are there differences in the mercury content among the soil profiles studied?

(II) Is there a correlation between permafrost degradation and the accumulation of mercury within the soil profiles?

2. Scientific Background

2.1. Periglacial Environments and Permafrost

Periglacial environments are unique and dynamic regions, characterized by cold, non-glacial climates and influenced by intensive frost action and freeze-thaw processes (French, 2007). The Pleistocene, the most recent geological epoch that experienced multiple glacial cycles, is the period during which most of the glacial and periglacial landforms and sediments found today were formed. However, the ongoing warming of the climate throughout the Holocene has led to a reduction in these environments, resulting in a smaller periglacial area compared to the past (Hughes, 2013).

Presently, periglacial environments cover approximately 20 % of the Earth's land area (French, 2011). They are primarily located in high latitudes of the northern hemisphere, including northern deserts, high Arctic semi deserts, tundra zones and northern regions of boreal forests. Additionally periglacial features can be found on mountainous regions, ice free areas of Antarctica and on some oceanic islands in high latitudes (French, 2011). The characteristics of periglacial environments and their associated land features are linked to the abundance of ice and snow, encompassing processes such as freezing, including frost action, frost heaving or frost cracking, as well as thawing processes leading among others to thermal erosion, and repetitive freeze-thaw processes which can result for example in solifluction (Dixon, 2013). The mean annual temperature of periglacial areas must remain below 3 °C, although the ground temperature holds greater significance for the landscape dynamics than the air temperature (French, 2011). Periglacial environments typically include two components of the cryosphere, namely snow or sea ice and frozen ground, and thus is often underlain by permafrost (French, 2007; Murton, 2021)

Permafrost refers to any ground with temperatures that remain at or below 0 °C for two or more consecutive years (van Everdingen, 1998). Being strictly defined by temperature, not aggregate state, permafrost does not necessarily imply frozen ground, because the freezing point can be decreased for example due to salt enriched porewater. This is likely in coastal regions, like the study area.

Permafrost underlies extensive areas with an estimated coverage of approximately 15 % of the northern hemisphere (Obu et al., 2019). It can be categorized into various types, including terrestrial, submarine and mountain permafrost, each exhibiting distinctive characteristics (Schirrmeister et al., 2011b). As illustrated in figure 2.1 four different permafrost zones are defined (Obu et al., 2019). The first zone is continuous permafrost, referring to regions where more than 90 % of the area is underlain by permafrost (van Everdingen, 1998). Continuous permafrost is most prevalent in high latitudes in Alaska,

Siberia, and Canada, as shown in figure 2.1. The second zone is discontinuous permafrost, which encompasses regions that are 50-90 % underlain by permafrost. The third zone is sporadic permafrost, assigned to areas with 10-50 % permafrost coverage. The fourth zone represents isolated patches of permafrost, referring to areas where permafrost occurs but underlies less than 10 % of the region, surrounded by unfrozen ground (van Everdingen, 1998). Generally, there is a decrease in the spatial extent of permafrost with decreasing latitude, without distinct boundaries separating the different permafrost zones.

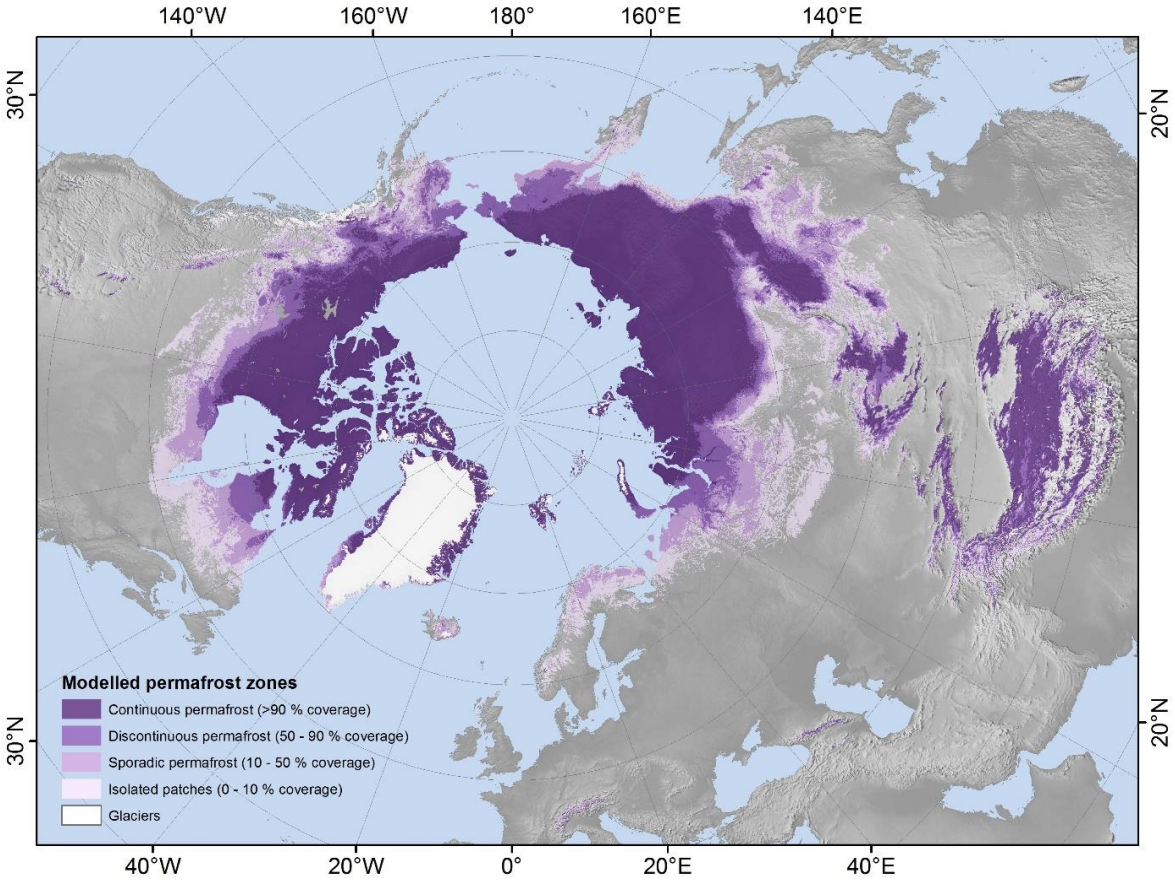

Figure 2.1: Permafrost distribution in the northern hemisphere (Obu et al., 2019)

The vertical extent and the growth of permafrost is influenced by both air temperature from above and the geothermal gradient from below. Its extent can range from several centimetres to 1500 meters (Schirrmeister et al., 2011b). Due to the cold continental climate and a low earth interior heat flux, the thickest permafrost layers are found in Siberia. Additionally, the horizontal extent of continuous permafrost towards lower latitudes is largest in Siberia, as depicted in figure 2.*1*.

Permafrost ground can be vertically divided into different layers. The uppermost layer is the active layer, which experiences seasonal temperature changes, thawing during summer and refreezing during winter (French, 2011). The vertical extend of the active layer

varies with a decrease of latitude between several decimetres to more than two meters (Schirrmeister et al., 2011b). Below the active layer is the permafrost zone. Within this zone unfrozen areas called taliks, may occur. Taliks often develop beneath waterbodies but can also be enclosed by Permafrost (Schirrmeister et al., 2011b). Moreover, the lateral intrusion of saltwater to thermokarst features in coastal regions can create marine cryopegs, cryotic layers of unfrozen ground, in which freezing is prevented by a decreased freezing point due to high salt contents (Angelopoulos et al., 2021; Gilichinsky et al., 2005).

Permafrost is characterized by the presence of ground ice in various forms and sizes. It can appear as microscopic inclusions, but also as large masses with a size up to 50 m (Jorgenson et al., 2011). In northern Alaska mainly two forms of ground ice exist: (1) porous and segregated ice forming the cryostructure of the soil and (2) massive ground ice bodies, including ice wedges, thermokarst-cave ice, and ice cores of pingos (Jorgenson et al., 2011).

2.2. Permafrost Degradation, Thermokarst and Coastal Permafrost Landscapes

Permafrost degradation is the result of complex interactions influenced by various biophysical factors, including climate, hydrology, ecology, and geology, as well as short-term disturbances (Olefeldt et al., 2016). These interactions lead to changes of the thermal regime of the ground (Jorgenson et al., 2010). When the mean ground temperature exceeds the melting point of water, which can occur with temperatures below 0 °C, permafrost soils begin to thaw and undergo degradation.

One of the most significant effects of permafrost degradation is the formation of thermokarst features (Dixon, 2013; Murton, 2021). Thermokarst refers to the process of ice-rich permafrost thawing, leading to land subsidence and ground sinking (Kokelj & Jorgenson, 2013). This process results in various characteristic landforms, including wetlands, lakes, pounds, and drained lake basins (Coulombe et al., 2022). During the late Pleistocene and throughout the Holocene, intense permafrost degradation occurred, leading to the formation of tens of thousands thermokarst lakes and drained lake basins in northern lowland permafrost regions (Grosse et al., 2013). It is estimated that approximately 20 % of the permafrost regions are covered by thermokarst landscapes today (Olefeldt et al., 2016). Geomorphic processes primarily drove this genesis of thermokarst and its features in the past. However, in recent decades, anthropogenic

influences, and disturbances such as global warming, wildfires, and animal activities have increasingly affect the process (Shur & Jorgenson, 2007; Murton, 2021).

As mentioned earlier, permafrost degradation and the development of thermokarst often involve the formation of thermokarst lakes (Grosse et al., 2013). These lakes occupy depressions in the ground formed by the thawing of ice-rich permafrost and the melting of massive ground ice (van Everdingen, 1998). Typically, thermokarst lakes are shallow and change and evolve over time. During this evolution, the lake undergoes various stages. In the first stage a talik forms beneath the lake. This body of unfrozen ground can lead to further thawing of the permafrost surrounding the lake, increased ground subsidence, and vertical growth of the lake (Grosse et al., 2013). When the depth of the lake exceeds the thickness of the winter ice cover of the lake, the thaw of permafrost around the lake and growth of the talik is accelerated due to water temperatures above 0 °C all year around. In addition to vertical growth, the lakes can also expand horizontally through thermal and mechanical erosion of the adjacent permafrost (Grosse et al., 2013). The final stage of the thermokarst lake evolution is the drainage, which typically occurs through horizontal outflow. It can result from different causes, as for example a changed water balance, a melting ice wedge network creating a drainage pathway, gully erosion toward another waterbody or coastal erosion (Hinkel et al., 2007; Lijedahl et al., 2016). Another possible drainage process is a vertical outflow of the water through an open talik, especially in discontinuous permafrost (Arp et al., 2011). After a drainage event, the now subaerial taliks refreeze. Then the drained lake basins can become vegetated again, which leads to the possibility of the accumulation of organic material at least on the short term and the formation of peat in the permafrost soils over time (Jones et al., 2012).

Particularly vulnerable to permafrost degradation and thawing processes are coastal permafrost landscapes. This vulnerability is further accelerated by the warming of the Arctic Ocean, warming nearly 4 times the speed of the global average (Rantanen et al., 2022), the reduction of sea ice cover, and longer ice-free periods, all of which contribute to increased erosion along the permafrost coastline (Jenrich et al., 2021). Consequently, thermokarst lakes in nearshore areas can evolve into thermokarst lagoons, because of the coastal erosion (Ruz et al., 1992).

Thermokarst lagoons are shallow waterbodies with intermittent or permanent connections to the sea, but separated, at least partially, by barriers from the open ocean. They represent a transitional zone between marine and non-marine realms (Romanovskii et al., 2000). The formation and evolution of thermokarst lagoons along Arctic coasts is a dynamic process, influenced by local conditions and geography, but following several general stages.

Initially, there is a nearshore thermokarst freshwater lake on land. Ongoing coastal erosion causes the coastline to migrate inland, therefore the lake becomes situated closer to the sea and eventually entering the flooding area. Subsequently, the initial thermokarst lake becomes intersected and breached by the advancing sea. This leads to the formation of an intermittent or permanent connection between the lake and the ocean, for example through a drainage channel. In case multiple lagoons and lakes become interconnected through horizontal erosion and drainage channels, lagoon systems develop. Over time, continuing coastal erosion strengthens the connection of Arctic lagoons to the ocean, potentially leading to a complete inclusion of the lagoon, due to incorporation.

The intrusion of marine waters into the lagoons implements high concentrations of ions, among other sulfates, creating a salt gradient across several meters of sediment in the originally freshwater environments (Yang et al., 2023). As a result, microbial processes, carbon cycling, and overall ecosystem dynamics undergo changes compared to the initial state as a thermokarst lake. Depending on their connection with the sea, Arctic thermokarst lagoons can experience high seasonal fluctuations in temperature and salinity over the course of a year (Harris et al., 2017). During winter, when both the ocean and lagoons are covered by ice for 8-9 month, hyper-saline conditions can develop. In contrast, during the 3-4 month open water period, the lagoons experience a notable decrease in salinity due to an intense freshwater discharge form rivers and melting sea ice (Harris et al., 2017).

2.3. Carbon Accumulation in Permafrost Soils

Permafrost is recognized today as one of the largest climate-sensitive carbon reservoirs on Earth. The characteristic low temperatures and poor drainage of permafrost soils result in minimal microbial activity and consequently reduced decomposition rates of organic material (Hugelius et al., 2014). This kind of environment allowed for long-term accumulation of organic material and carbon within the permafrost over thousands of years (Strauss et al., 2021). As shown in figure 2.2 it is estimated that soils in permafrost regions store approximately 1400-1600 Gt soil organic carbon (SOC), which is around twice the amount currently present in the atmosphere (Schuur & Mack, 2018). Although northern areas account for only 15 % of the global soil area, they contain between 42-50 % of the global SOC (Schuur et al., 2015). Moreover, Miesner et al. (2023) recently quantified an

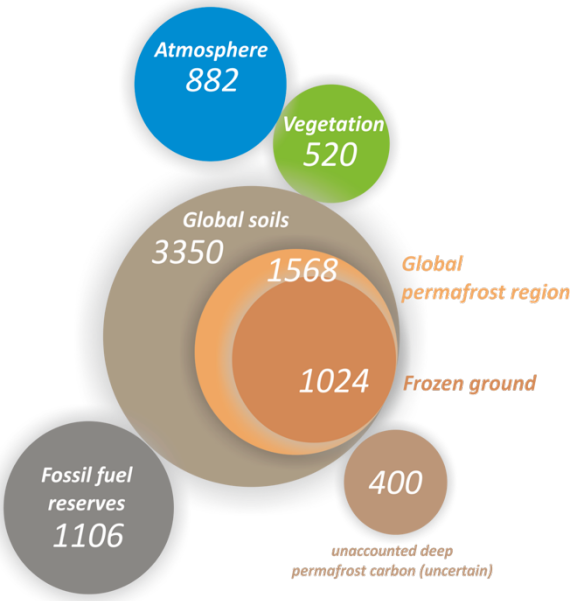

Figure 2.2: Terrestrial and atmospheric carbon stocks [Gt] (Strauss et al., 2021)

additional carbon pool of 2822 Gt in subsea permafrost, making the permafrost domain the largest terrestrial carbon pool on the planet.

As permafrost thaws, the stored organic material becomes available for microbial decomposition, thereby the accumulated organic carbon gets reintroduced into the recent carbon cycle, primarily in form of carbon dioxide (CO_2) and Methane (CH_4) (Strauss et al., 2017). The global increase in permafrost thaw due to climate warming leads to increased greenhouse gas fluxes from permafrost soils to the atmosphere, consequently exacerbating climate warming and initiating a positive feedback loop (Hugelius et al., 2014).

Greenhouse gas emissions resulting from thawing permafrost vary depending on whether aerobic or anaerobic conditions are predominate in the soils (Schuur et al., 2015). Under aerobic conditions, typically found in upland permafrost and drained thermokarst lake basins, the main greenhouse gas released is CO_2. Whereas under anaerobic conditions, developing in water-saturated soils such as those beneath thermokarst lakes and wetlands, microbial decomposition leads to the release of both CO_2 and CH_4 (Schuur et al., 2015).

When studying carbon distribution and cycles within permafrost landscapes, particular attention should be given to thermokarst landscapes, such as the study area around the Teshekpuk Lake in northern Alaska, since these regions are estimated to store approximately 50 % of the total SOC within permafrost, while covering 20 % of the northern permafrost regions (Olefeldt et al., 2016).

3. Study Area – Teshekpuk Lake Region

The research area of this study is located in the Arctic coastal plain of northern Alaska, north of the Teshekpuk Lake, as a part of the *National Petroleum Reserve* (figure 3.1). Bordered in the north by the Beaufort Sea, the region is characterized by a high abundance of thermokarst lakes, with the Teshekpuk Lake being the world's largest thermokarst lake, and equally numerous drained lake basins (Arp et al., 2011). The surrounding area,

including the northern coast, represents one of the largest contiguous wetland complexes in the Arctic. The formation and preservation of these wetlands is mainly due to the comprehensive presence of continuous permafrost beneath the ground surface in the area (Jorgenson et al., 2011).

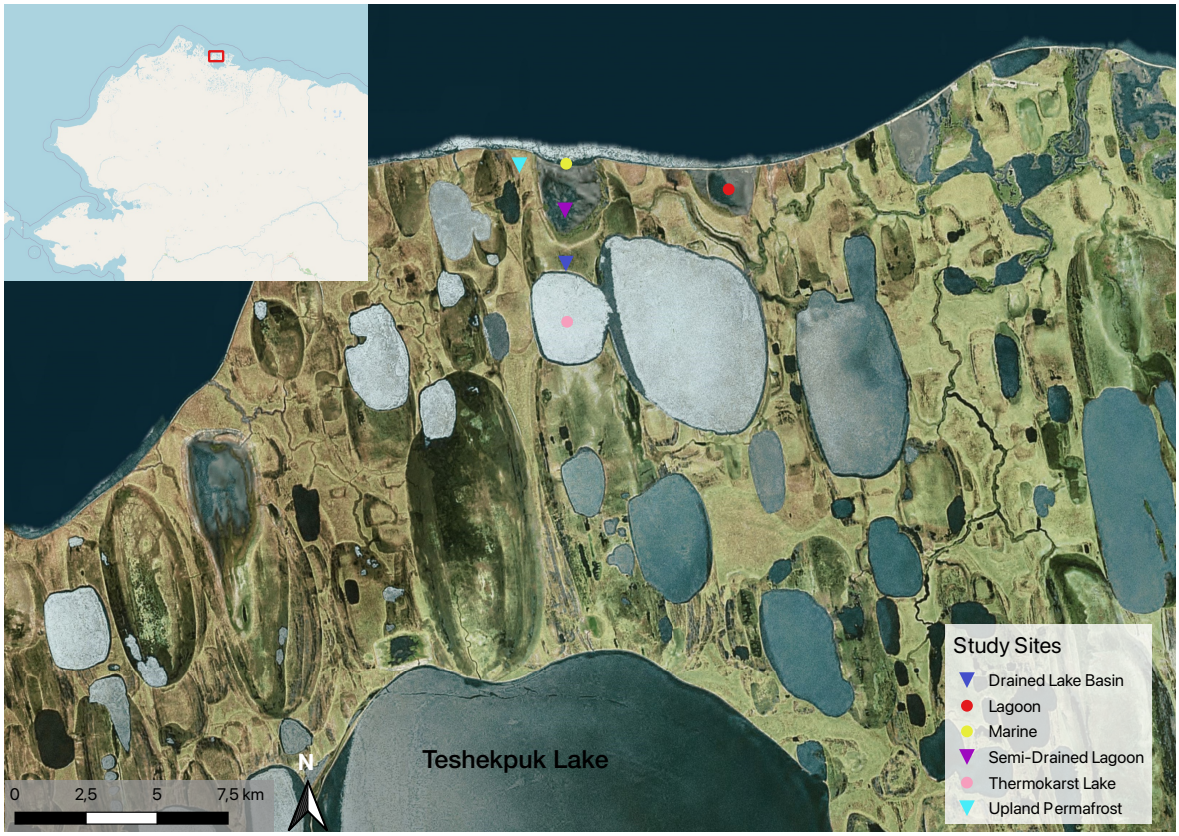

Figure 3.1: Map of the study sites

The northern coastal plain of Alaska is characterized by a predominantly flat terrain with a gentle slope towards the northern coast (Moore et al., 1994). The area is underlain by the *Colville basin*, a foreland basin of the *Cretaceous* and the *Tertiary age* (Moore et al., 1994).

The region in which the coastal plain is located is the North Slope, an area framed by the Brooks Range in the south and the Beaufort Sea in the north. The region encompasses diverse geological deposits including deposits originated in the North American craton, passive margin sediments, rift sediments, pelagic sediments, volcaniclastics and deposits from the foreland basin (Jorgenson et al., 2011).

Deposits in the study area consist of glacio-marine silt, marine sand, alluvial sand, and silt and eolian sand from the Holocene and mid-Quaternary epochs (Jorgenson & Grunblatt, 2013). The landscape is continuously transformed by thawing permafrost and melting ground ice, resulting in ground subsidence, the formation of new thermokarst lake basins,

lake drainage, and coastal erosion leading to the formation of lagoons and embayments (Jorgenson & Shur, 2007).

The climate of the region is cold and arid, with long winters lasting 8-9 months, persistent winds and mean annual temperature around -12 °C (Jorgenson et al., 2011). Despite the low mean annual precipitation of approximately 115 mm per year, which would make the area a desert, a productive wetland can be found, since the presence of continuous permafrost prevents subsurface drainage of the water and thereby shapes the hydrological conditions of the area (Jorgenson et al., 2011, Wendler et al., 2014). The highest monthly precipitation occurs in August and a seasonal snow cover persists from September/ October to May/June (Jorgenson et al., 2011).

The soil composition in the area is intrinsically tied to the presence of permafrost, with an interplay of low temperatures, impeded drainage, freeze-thaw dynamics, cryoturbation, and ground ice aggregation, collectively shaping its characteristic. Moreover, the region's high wetland productivity leads to the accumulation and sequestration of organic carbon in the soil (Jorgenson et al., 2011).

The study area exhibits a very diverse range of Flora and Fauna. It is covered by a mosaic of vegetation types, affected, and shaped by lacustrine processes, basin drainage, ice aggregation, fluvial processes, salinisation, and marine processes (Jorgenson et al., 2011). Vegetation types that can be found in the study area include coastal Barrens, lowland and coastal Wet Sedge Meadows, coastal Grass and Shrub Tundra, lowland moist Sedge Shrub Tundra and patches of upland Dryas Dwarf Shrub Tundra, as well as riverine Wet Sedge Tundra (Jorgenson & Heiner, 2003). Plant species that can be found are for example Alaska cotton gras [*Eriophorum angustifolium*], oval leaf willow [*Salix ovalivolia*] and tealeaf willow [*Salix pulchra*]. Large animals that occur at the coast of northern Alaska and therefore characterize it are for example Caribous, Wolves, Polar bears as well as many migratory birds (Pearce et al., 2018).

4. Methods

This study involved fieldwork, a laboratory analysis, and a statistical analysis, which are further explained in the following chapters. In total six sediment cores from a land-to-sea transect located in northern Alaska, from upland permafrost, a thermokarst lake, a drained lake basin, a semi-drained lagoon, an intact lagoon, and a marine setting were analysed.

4.1. Fieldwork

The fieldwork was performed during the expedition *Perma-X Lagoon Alaska 2022* to the *Teshekpuk Lake Area* in Alaska in April 2022. The expedition was joined by members of the *University of Alaska Fairbanks* and of the *Alfred Wegener Institute [AWI]* in Potsdam. For this master project six cores, that were drilled during the expedition, were chosen, located in a transect from the inland to the coast (figure 3.1). All chosen sample sites have different landscape features of coastal thermokarst landscapes (table 4.1).

Table 4.1: Characteristics of the study sites, core length, coordinates, and number of samples

Core ID	Landscape	Core length	Coordinates	Number of Samples
TES22-UPL1-02	Upland permafrost ground, frozen	203 cm	70.8851416667° N, 153.708283333° W	11
TES22-TKL1-02	Thermokarst lake, unfrozen	50 cm	70.8361944444° N, 153.662805556° W	7
TES22-DLB1-01	Drained thermokarst lake basin, frozen	219 cm	70.854375° N, 153.663944444° W	13
TES22-LAG1-01	Semi-drained lagoon basin, frozen	183 cm	70.8709944444° N, 153.664761111° W	14
TES22-LAG2-01	Lagoon [outside the transect], unfrozen	31 cm	70.8776° N, 153.5088° W	2
TES22-MAR1-02	Marine ground, unfrozen	12 cm	70.8855861111° N, 153.663691667° W	1
Total Sample size				**48**

In total three of the cores were unfrozen and the other three were frozen.

The three unfrozen cores were sampled using a *Push Corer* [Ø 6 cm]. Their length varied between 12-50 cm. The cores were stored in plastic tubes and maintained at a cool temperature of approximately 4 °C during the transport and until further analysis at *AWI Potsdam*.

Figure 4.1: Impressions of the fieldwork during the expedition Perma-X Lagoon Alaska, April 2022; images from Maren Jenrich.

The three frozen cores were drilled using a *SIPRE Corer* [Ø 7,6 cm]. These frozen cores were all around 200^{+-20} cm long. The cores were transported in shorter segments of approximately 50 cm and placed in core foil. The soil remained frozen during the drilling process and the cores were kept frozen during the transport and the storage at *AWI Potsdam* until further analysis.

4.2. Laboratory Analysis

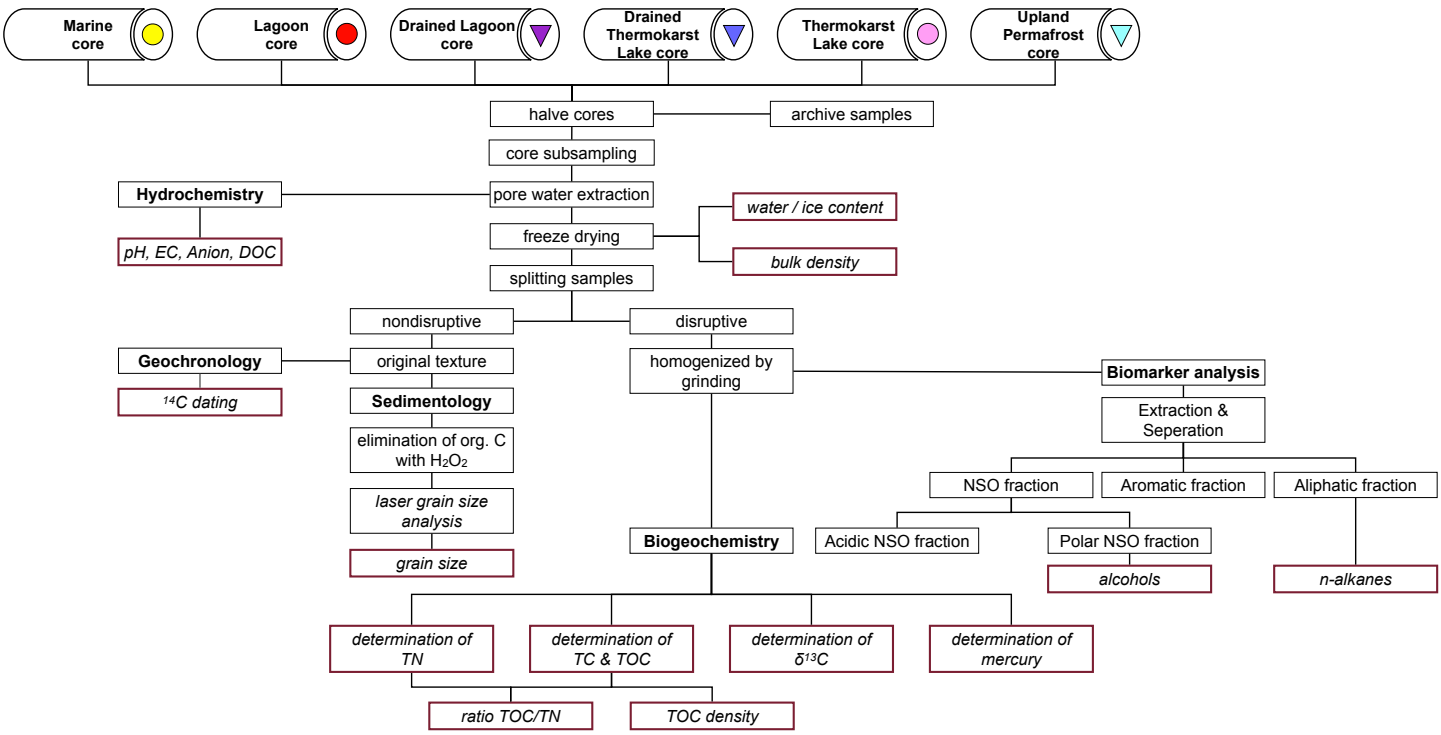

Figure 4.2: Flowchart of the laboratory analysis of the cores; red framed boxes represent data output.

To achieve the abovementioned aims of this mater thesis, a multi-proxy approach was used, encompassing a hydrochemical, a geochronological, a sedimentological, a biogeo-

chemical, and a lipid-biomarker analysis. In Figure 4.1 a flowchart with the workflow of all the used laboratory methods is shown.

4.2.1. Core Subsampling

The three frozen cores were subsampled in the *AWI Climate Chamber,* where temperatures were maintained at around -8 °C. Initially, each core was cut lengthwise into two halves using a *Makita Band Saw.* After that, both halves were cleaned at the artificially thawed edges caused by the sawing, photographed, and sedimentologically and cryolithologically described.

While one of the halves was put back into a narrow plastic bag and kept as an archive sample for potential further work, the other half was subsampled. To ensure comprehensive coverage of all features and stratigraphical layers within the core, subsamples for sedimentological and biogeochemical analysis were taken at intervals of 5-10 cm. Depending on the visible ice content, the length of the sample pieces varied between 2-12 cm. The subsamples were collected in small whirl packs and maintained in a frozen state until further analysis.

For the biomarker analysis a subset of at least three samples of each core, in the upper, middle, and lower part of the cores, were taken (two middle-part-samples of the *drained thermokarst lake (DLB) core*). The biomarker samples were stored in clean, combusted glass containers until further analysis.

In case of the unfrozen cores, the plastic tubes containing the soil were sawed into halves, and the sediment was cut with a nylon string. The halves were than cleaned at the edges, photographed, and sedimentologically described. One of the core halves was kept as an archive sample, except for the marine core, which was completely subsampled due to its short length.

The selection and further processing of the subsamples of the unfrozen cores was the same as for the frozen cores. However, due to their short length, only one biomarker sample was taken from the marine core, and two samples from the other two cores. All subsamples were frozen and stored in a frozen state until further analysis.

4.2.2. Hydrochemical Porewater Analysis

A hydrochemical analysis of the porewaters was performed using the uppermost sample of each core in case of the unfrozen cores, while for the frozen cores, samples from the top, middle and bottom sections were selected.

This part of the analysis can for example provide relevant information about the origin and flow direction of the porewater. Measured parameters of this analysis were the electric conductivity, pH-values, content of anions, and dissolved organic carbon (DOC).

4.2.2.1. Porewater Extraction

The selected samples were thawed at room temperature overnight, to prepare them for the porewater extraction. The porewater was taken the next day, using Rhizons (RHIZONS MOM 5 and 10 cm, Rhizospheres Research Products). Therefore, the Rhizons were inserted into the soil samples and a vacuum was created using plastic syringes. The extracted water was than distributed into different vials for the different hydrochemical measurements.

4.2.2.2. pH Value and Electrical Conductivity

The measurement of pH values and electrical conductivity (EC) of the soil samples can provide key information about the chemical and physical properties of the soil. While the pH affects the nutrient availability and microbial activity, the EC as a measure of soil salinity can indicate the presence of contaminations and can provide information on the degree of marine influence on the particular sample site and soil depth (Alam et al., 2020).

The pH value and EC were measured one day after the pore water extraction with a *WTW Multilab 540* using 4 ml of porewater.

4.2.2.3. Anions

The concentration of anions in the porewater can provide different information, like the availability and mobility of nutrients, as well as a potential risk of anion accumulation leading to soil degradation. In this study, the chloride and sulfate concentrations are of particular interest, as they provide information on the degree of acidification and salinization and can thus indicate the extent to which the sample sites are influenced by the ocean.

For the measurement of anions 5 ml of the pore water of every sample was filled into an 8 ml LDPE-Bottle. Samples with a high electrical conductivity were diluted in ratio of 1:25, 1:50 or 1:100, where applied the higher the electrical conductivity the higher the dilution ratio. The Anions were measured using a *Thermo ICS2100*.

4.2.2.4. DOC Content

For the analysis of the DOC content in the porewater 10-20 ml of each sample was filled into a glass vial. To preserve the samples until further analysis they were acidified with 50 μl of 30 % hydrochloric acid (HCL) and stored at 4 °C. The measurement was carried out using a *Shimadzu Total Organic Carbon Analyzer (TOC-VCPH)*. The results of three to five injections were used as an average to determine the total DOC content. The detection limit was 0.25 mg/L and the uncertainty ranged between ±10 % for measured values higher than 1.5 mg/L and ±15-20 % for values lower than 1.5 mg/L.

4.2.3. Sedimentological Analysis

The sedimentological analysis was performed as a non-destructive approach and included the measurement of the water-/ice content, the bulk density, and the grain size.

4.2.3.1. Water-/ Ice Content & Bulk Density

To determine the ice content of the frozen samples and the water content of the unfrozen samples, all samples were weighed directly after subsampling. The next step was to freeze-dry all samples in a *Zirbus Subliminator 3-4-5* at -40 °C and 0.2 bar for 48 h. For organic rich samples this step had to be repeated, to get the samples completely dry. The dried samples were weighed again, and the ice-/water content was calculated using the following equation (1):

$$\frac{\text{Netto Wet Weight [g]} - \text{Netto Dry Weight [g]}}{\text{Netto Wet Weight [g]}} * 100 = \text{Absolute Water Content [wt\%]} \quad [1]$$

In addition to the determination of the water content, the bulk density (BD) of the soil was also calculated. The BD refers to the mass of soil per unit volume [g/cm^3], encompassing both solid particles and pore spaces. It serves as an indicator of soil compaction and porosity.

For the unfrozen core samples, measuring 3 cm^3 in volume, the BD was calculated using the following equations [2a, 2b]:

$$\frac{\text{Netto Wet Weight [g]}}{\text{Volume [cm}^3\text{]}} = \text{Wet Bulk Density [g/cm}^3\text{]} \quad [2a]$$

$$\frac{\text{Netto Dry Weight [g]}}{\text{Volume [cm}^3\text{]}} = \text{Dry Bulk Density [g/cm}^3\text{]} \quad [2b]$$

As the volume of the frozen samples was not measured, the BD was calculated, based on three assumptions. Firstly, it was assumed that samples with an ice content of ≥ 20 % were ice saturated (Strauss et al., 2012). Secondly, the density of dry minerals was considered to be 2.65 g/cm^3 (Rowell 1994). Lastly, the ice density at a temperature of -10 °C was assumed to be 0.918 g/cm^3 (Harvey, 2019). By incorporating these three assumptions, the bulk density could be calculated using the following equations (3a, 3b, 3c):

$$\frac{\text{Netto Dry Weight [g]}}{\text{Density of the solid fraction (2.65) [g/cm}^3\text{]}} = \text{Volume of solid particles [cm}^3\text{]} \quad [3a]$$

$$\frac{\text{Netto Wet Weight [g] - Netto Dry Weight [g]}}{\text{Density of ice (0.917) [g/cm}^3\text{]}} = \text{Pore Volume [cm}^3\text{]} \quad [3b]$$

$$\frac{\text{Netto Dry Weight [g]}}{\text{Volume of solid particles [cm}^3\text{] + Pore Volume [cm}^3\text{]}} = \text{Dry Bulk Density [g/cm}^3\text{]} \quad [3c]$$

4.2.3.2. Grain Size Analysis

A grain size analysis was carried out, to provide information about the physical properties of the soil. This is a basis to understand soil behaviour, reconstruct and predict soil movement in the study area and therefor the origin of deposits, including the medium of transport and conditions during the deposition.

The first step of the analysis was the preparation of the samples, by removing the contained organic matter. Therefore, a solution of 100 ml 3 % hydrogen peroxide [H_2O_2] and 4 ml 25 % ammonia [NH_3] were added to the freeze-dried samples. They were then placed on a shaker for approximately four weeks to allow for thorough mixing and reaction of the solution with the samples. During the period of four weeks, 10 ml of 30 % H_2O_2 were added to the samples daily during weekdays, while monitoring the pH to ensure it remained between 6 and 8. If the pH fell outside of this range, it was adjusted accordingly with either ammonia or concentrated acetic acid.

The next step was to rinse the samples with purified water, to remove the H_2O_2, followed by centrifugation. The supernatant liquid was then decanted, and the remaining sediment was freeze-dried and manually homogenized. For each sample, 1 g of the homogenized material was placed into a plastic container, to which 0.5 g of tetra-sodium pyrophosphate [$Na_4P_2O_7$] and 0.0001 % ammonia solution [NH_3] were added to disperse the soil particles and prevent them from settling during the subsequent analysis. The sample container was then placed on a "Gerhard Laboshake overhead shaker" for 24 hours to allow for complete dispersion of the added solution. Each sample was than split into eight subsamples with a particle concentration of 5-15 % by a rotary cone sample divider. Simultaneously all particles > 1 mm were sieved out before analysis, weighed, and included in the results at the end. The grain size measurement was carried out using a *Malvern Mastersizer 3000* with a *Malvern Hydro LV wet-sample dispersion Unit.*

The international ISO 14688-1:2017 scale was used for the grain size classification. The ranges specified there are ≤ 2 µm for clay, 2 µm to 63 µm for silt and 63 µm to 2 mm for sand (ISO 14688-1:2017, 2017). All statistics of the grain size distribution were calculated using the software GRADISTAT (Blott & Pye, 2001)

4.2.4. Geochronology

A geochronological analysis was conducted, to determine the age of the soil and its components, since it provides information about the timing of soil formation, past environmental changes, influence of geological processes on soil development, and the reconstruction of landscape dynamics. Overall, this analysis is the basis for comprehensive understanding of the soil's depositional history and its interaction with the surrounding environment.

In total 10 samples were selected for the geochronological age determination. For the short cores obtained from the marine site and the lagoon, one sample was chosen from the middle section of each core. For the longer cores, two samples were selected, with one in the upper part and one in the lower part of each core.

After freeze-drying all the selected samples were picked for macro-organic under the microscope. The samples were sent to the *AWI Bremerhaven*. For samples with little macro-organic, milled samples from the same depth were additionally sent in for a bulk analysis. The radiocarbon dating was performed at *AWI Bremerhaven*, using a *Mini Carbon Dating System [MICADAS]*, a miniaturized acceleration mass spectrometer *[AMS]*. The determined radiocarbon ages were then calibrated with the *IntCal13* calibration curve, using the *CALIB 7.1 software* (Reimer et al., 2013).

4.2.5. Biogeochemical Analysis

The measured parameters of the biogeochemical analysis provide information about organic matter and microbial activity. Due to that it is possible to trace nutrient cycles and changes between the different stages of landscape development in the costal thermokarst landscape and to reconstruct paleoenvironmental conditions and processes.

The first step of the biogeochemical analysis was to homogenize all samples, to ensure that the required small amounts of samples for the analysis were representative. Therefore, the freeze-dried samples were milled using a planetary mill *[FRITSCH pulverisette 5]* for 8 minutes at 360 rotations per minute.

4.2.5.1. Total Carbon

The amount of the total carbon (TC) and the total organic carbon (TOC) is of special interest and importance in permafrost soils, since they contain a vast amount of organic carbon that has been accumulated and stored in the soils for thousands of years. The measurement of total organic carbon [TOC] is a quantification of the organic compounds of the total carbon content [TC] in the soil samples.

The determination was carried out using the elemental analyser *ELEMENTAR soliToC cube*, measuring TOC and total inorganic carbon (TIC). The first step for the measurement was the preparation of a control block, compromising two blank samples, three stainless steel capsules containing 20 mg $CaCO_3$ 6 %, three capsules with 50 mg IVA 2176, one capsule with 15 mg $CaCO_3$ 12 %, and one capsule with 100 mg EDTA (5:45). Following the control block the actual samples were processed in duplicate. Therefore 50 mg of each sample was weighed into stainless steel capsules twice. After 37 samples a second control block was placed into the measuring device consisting of one capsule with 15 mg $CaCO_3$ 12 %, one capsule with 100 mg EDTA 5:45, followed by two blank samples at the end. Using a temperature ramping program to distinguish between TOC and TIC the device was heating up to 400 °C as the first temperature step and held for 230 seconds. The next temperature step was 600 °C, held for 120 seconds and the last temperature was 900 °C, held for 150 seconds.

4.2.5.2. Carbon Density

The carbon density of each sample was determined using the measured values of the bulk density and the TOC content. It was calculated using the following equation (4) (Strauss et al., 2015).

$$BD\ [kg/m^3] \times \frac{TOC\ [wt\%]}{100} = TOC_{vol}\ [kg/m^3] \quad [4]$$

4.2.5.3. Total Nitrogen

The total nitrogen (TN) content was measured using the *ELEMENTAR rapid MAX N exceed*. As for the measurement of TC, for the measurement of the TN content the preparation of a control block was required. It consisted of two blank samples, four samples with 50 mg edta 5:45, one sample of 50 mg bs 1, one sample of 50 mg bs 2, 1 sample of 50 mg iva 2150 and one sample of 50 mg of iva 2156, all weighed into stainless steel capsules. Then 50 mg of 37 soil samples were weighed in in duplicates, followed by another control block and one blank sample at the end. Depending on the measured TOC content two different methods were used. All samples with TC contents > 15 wt% were measured with an oxygen flux of 160 ml/min, whereas the samples with a TC content < 15 wt% were measured with an oxygen flux of 120 ml/min. The temperature maximum of the combustion was for both methods 900 °C.

4.2.5.4. TOC/TN Ratio

From the measured TOC and TN contents the TOC/TN ratio was calculated. This ratio provides information on the sources and the degradation level of the organic matter (OM) in the sediment, with high values indicating a higher share of terrestrial sources or well-preserved OM and low values indicating a higher share of aquatic sources or a high level of degradation (Andersson et al., 2012; Meyers, 1997).

4.2.5.5. Total Mercury

The mercury content in sediments was measured to indicate for example the anthropogenic impact on the soils and the sampling sites.

The measurement of the mercury content was carried out using the *Direct mercury analyzer DMA-80 EVO.* Therefore, 50 mg of every sample was weighed into stainless steel capsules as duplicates. The subsequent drying and thermal decomposition in the measuring device was carried out under an oxygen atmosphere. The first phase of the process was the release of mercury, along with other combustion products, followed by the elimination of all interfering substances by passing them through the catalyst. The mercury was then selectively sequestered through amalgamation. Finally, the mercury was thermally

desorbed by heating of the amalgamation and quantitatively measured in multiple measurement cells of an optical spectrometer by the atomic absorption at 253.65 nm.

4.2.5.6. Stable Carbon Isotopes

The measurement of the $\delta^{13}C$ ratio, as a paleoenvironmental indicator, provides information on ancient biogeochemical processes and the degree of decomposition of OM. It is mainly determined by photosynthetic processes, but also by other factors like atmospheric CO_2, temperature, and water stress (Andersson et al., 2012).

The analysis started with the removal of carbonate from the samples. Therefor they were treated with 20 ml hydrogen chloride (HCL) for three hours at 97.7 °C, washed with purified water, filtered over a glass microfiber filter, and dried at 50 °C. To determine the required sample weight for the analysis 20 was divided by the TOC content [wt%]. The measurement was carried out using a *ThermoFisher Scientific Delta-V-Advantage gas mass spectrometer* with a *FLASH elemental analyser EA 2000* and a *CONFLO IV* gas mixing system. The samples were combusted in the device at 1020 °C. During the process the organic carbon in the sediments converted into CO_2. Subsequently, the isotope ratio [‰] was determined in relation to the established standard from the Vienna Pee Dee Belemnite [VPDB].

4.2.6. Biomarker Analysis

The identification and analysis of lipid biomarkers in the sediment samples can point out the original sources of the organic matter (OM), as well as the quality and level of degradation of the OM contained in the deposits (Schwarzbauer & Jovančićević, 2016).

In total 15 samples were selected for the biomarker analysis. In case of the shortest core, the marine site, only one sample was taken. In case of the unfrozen medium length cores from the lagoon and the thermokarst lake two samples, one from the upper and one from the lower part of the core, were picked. In case of the long, frozen cores three samples, respectively four in case of the longest core from the drained lake basin, were taken, from the upper, middle, and lower sections of the cores.

4.2.6.1. Measurement

The first step of the Biomarker analysis was freeze-drying the samples using a Zirbus Sublimator 3-4-5 at -40 °C and 0.2 bar for 48 h. To ensure sample homogenization, the samples were milled using a planetary mill *[FRITSCH pulverisette 5]* for 8 minutes at 360 rotations per minute.

Lipid biomarkers were then extracted using accelerated solvent extraction (ASE) with dichloromethane/methanol (DCM/MeOH 99:1). Therefor approximately 8 g of each sample was applied to a *ThermoFisher Scientific Dionex ASE 350* and held in a static phase for 20 min at 75.5 °C and 5 MPa. To remove the liquid residue of the solvent, a *Genevac SP Scientific Rocket Synergy evaporator* was used at 42 °C.

For the subsequent analysis, 8 µg of internal standards were added to all samples. Specifically, 5α-androstane as a reference for *n*-alkanes in the aliphatic fraction and 5α-androstan-17-one as a reference for *n*-alkanols in the neutral NSO-fraction. After evaporating the liquid solvent residues again, all samples were dissolved in 500 µl of *n*-hexane, and 300 µl of this solution was applied on a medium pressure liquid chromatograph (MPLC) (Radke et al., 1980). Within the MPLC, the components were separated into aliphatic, aromatic and NSO fractions. Furthermore, the NSO components were additionally separated into an acidic and neutral fraction by a manual column separation. In preparation for the measurement the neutral NSO fraction was silylated by adding 50 µl DCM and 50 µl N-Methyl-N-(trimethylsilyl)trifluoroacetamide (MSTFA) and heating it at 75 °C for one hour.

The measurement of *n*-alkanes in the aliphatic fraction and *n*-alkanols in the neutral NSO fraction was performed using gas chromatography-mass spectrometry (GC-MS). The specific device used was the *Thermo Scientific ISQ 7000 Single Quadrupole Mass Spectrometer* with a *Thermo Scientific Trace 1310 Gas Chromatograph*. The MS system was operated with a transfer line temperature of 320 °C and an ion source temperature of 300 °C. Ionization was achieved using an ionization energy of 70 eV at 50 µA. The full scan mass spectra (m/z 50 to 600 Da, 2.5scanss^{-1}) was analysed using the software *XCalibur*. The *n*-alkanes and *n*-alkanols were quantified by comparing their peaks to the peaks of the applied internal standards.

4.2.6.2. Biomarker Indices

In total eight indices were calculated from the measured lipid biomarker concentrations.

Four of these indices, calculated from the *n*-alkane content, provide information on respective sources of the organic Carbon (OC).

The first two of them were the average chain length (ACL) of short chain *n*-alkanes (equation 6a), calculated for carbon numbers $C_{15\text{-}21}$, as well as the ACL of long chain *n*-alkanes (equation 6b), calculated for *n*-alkanes with a carbon number interval of $C_{23\text{-}33}$ (Poynter & Eglinton, 1990; Strauss et al., 2015). The short chain odd-numbered *n*-alkanes can indicate an aquatic influence on the OC sources since they are produced by bacteria

and algae, whereas the long chain odd-numbered *n*-alkanes are mainly produced by terrestrial higher plants like bryophytes (n-C23 & n-C25), leaf waxes (n-C27-n-C29), and grasses (n-C31-n-C33) (Haugk et al., 2021; Zech et al., 2009). A change of the ACL can suggest a change of the OC sources and thus a change of input vegetation type (Schäfer et al., 2016).

$$\frac{\sum i\, C_i}{\sum C_i} = ACL_{15\text{-}21} \qquad [6a]$$

$$\frac{\sum i\, C_i}{\sum C_i} = ACL_{23\text{-}33} \qquad [6b]$$

The third and fourth indices are the P_{aq} (equation 7a) and the P_{wax} (equation 7b), two ratios that can be used as proxies for the intensity of aquatic influence on the sediments and to differentiate between aquatic and terrestrial plant input (Thomas et al., 2023; Zheng et al., 2007). With the values of the P_{aq}, developed by Ficken et al. (2000) it is possible to distinguish between submerged and floating macrophytes, values between 0.4 and 1, emergent macrophytes, values between 0.1 and 0.4, and terrestrial plants, values < 0.1, as a source for OC in the soil (Ficken et al., 2000). Since this proxy and its thresholds were developed in tropical regions, the P_{wax} was additionally calculated for this study, as seen in Jongejans et al. (2020). The P_{wax}, developed by Zheng et al. (2007), indicates the relative proportion of waxy hydrocarbons from emergent macrophytes and terrestrial plants to total hydrocarbons (Zheng et al. 2007).

$$\frac{C_{23} + C_{25}}{C_{23} + C_{25} + C_{29} + C_{31}} = P_{aq} \qquad [7a]$$

$$\frac{C_{27} + C_{29} + C_{31}}{\sum \text{odd } C_{23\text{-}31}} = P_{wax} \qquad [7b]$$

The following four indices are used to provide information on the level of degradation of the OC in the soils.

The first three indices calculated in this category are the Carbon preference index (CPI) for short chain *n*-alkanes (CPI-alk-short), the CPI for long chain *n*-alkanes (CPI-alk-long), and the CPI for *n*-alkanols (CPI-alc). The CPI was introduced by Bray and Evans (1961). As a measure of alteration of OC, values of the CPI decrease with the degradation of OC in the soil (Marzi et al., 1993; Strauss et al., 2015). The calculation in this study was carried out using the equation introduced by Marzi et al. (1993) with a revised chain length interval of $C_{15\text{-}21}$ (equation 8a) for the short chain *n*-alkanes, an interval of $C_{23\text{-}33}$ (equation 8b) for the long chain *n*-alkanes, and a chain length interval of $C_{22\text{-}32}$ for *n*-alkanols (equation 8c).

$$\frac{\sum \text{odd } C_{15\text{-}19} + \sum \text{odd } C_{17\text{-}21}}{2 * \sum \text{even } C_{16\text{-}20}} = CPI_{15\text{-}21}\ n\text{-alkanes - short} \qquad [8a]$$

$$\frac{\sum \text{odd } C_{23\text{-}31} + \sum \text{odd } C_{25\text{-}33}}{2 * \sum \text{even } C_{24\text{-}32}} = CPI_{23\text{-}33}\ n\text{-alkanes - long} \qquad [8b]$$

$$\frac{\sum \text{even } C_{22\text{-}30} + \sum \text{even } C_{24\text{-}32}}{2 * \sum \text{odd } C_{23\text{-}31}} = CPI_{22\text{-}32}\ n\text{-alkanols} \qquad [8c]$$

The fourth index as a measure of extend of degradation of OC, introduced by Poynter (1989), is the higher plant index (HPA). As a basis of this index, it is assumed that the input ratio of *n*-alkanols and *n*-alkanes into a sedimentary environment is constant. Therefore, the ratio should depend on the extent of degradation, and since the *n*-alkanols are preferentially degraded over the *n*-alkanes the ratio decreases with ongoing degradation (Poynter & Eglinton, 1990). The index was calculated using the following equation (9) (Poynter & Eglinton, 1990).

$$\frac{\sum (n\text{-alkanols } C_{24}, C_{26}, C_{28})}{\sum (n\text{-alkanols } C_{24}, C_{26}, C_{28}) + \sum (n\text{-alkanes } C_{27}, C_{29}, C_{31})} = HPA \qquad [9]$$

4.3. Statistical Analysis

The statistical analysis of the data included the creation of a correlation matrix, a cluster analysis, as well as the analysis of the central tendencies of the different measured parameters. The implementation of these analyses is further explained in the following chapters.

4.3.1. Correlation Matrix

To test the data for existing correlations between the different measured parameters, two correlation matrices were created in R, using the packages “readxl” and “corrplot” (Appendix R-script A.1). The calculation of the correlation was carried out after Pearson. The finished plots of the correlation matrices only show correlations with a significance $p < 0.05$. In the first correlation matrix sedimentological and biogeochemical parameters were included. Due to the smaller sample size in the biomarker analysis a separate correlation matrix was created, which next to the biomarker indices also included mercury and $\delta^{13}C$, since these were the only parameters correlating significantly with the biomarker indices.

4.3.2. Cluster analysis

To test the data for existing structures an interdependency analysis in the form of a *k*-means cluster analysis was carried out. The parameters included in the analysis were mean grain size, dry bulk density, absolute water content, TOC, TN, TOC/TN ratio, $\delta^{13}C$, mercury, and TOC_{vol}. For the implementation of the cluster analysis R was used. The packages included in the analysis were “readxl”, “tidyverse”, “cluster”, “factoextra”, “broom”, and “ggplot2” (Appendix R-script A.2). The method chosen to create the distance matrix, as the base of the cluster analysis, was the *Euclidean distance*. The first step of the *k*-means clustering was the specification of the number of clusters (k), which was set to four. The algorithm then chose randomly *k* objects to be the initial centres of the clusters. All observations were than assigned to the closest centroid, according to the calculated *Euclidean distance* and for each cluster the centroid is continuously updated by calculating the new mean of the datapoints in the cluster. The algorithm reported the best out of 25 initial configurations.

4.3.3. Central Tendency Analysis

The statistical tests to compare the different sites regarding their central tendencies of the different biogeochemical parameters was only applied to the SDLAG, TKL, DLB and UPL cores, since the LAG and MAR cores had a to small sample size for the statical analysis. After testing and disproving a normal distribution of the data, the nonparametric Kruskal-Wallis rank sum test was chosen to compare the data of the four different sites. For an additional pair-wise comparison of cores the Mann-Whitney-Wilcoxon test was used. In addition, it was tested, if there are statistically significant differences between deposits that are influenced by saltwater (MAR, LAG, SDLAG) and deposits that are not influenced by saltwater (DLB, TKL, UPL) and the frozen (SDLAG, DLB, UPL) and unfrozen (MAR, LAG, TKL) cores, using the Mann-Whitney-Wilcoxon test. All tests of the central tendency analysis were carried out using R (Appendix R-script A.3).

5. Results

In the following chapter the results of the laboratory and statistical analysis are presented. It starts with the description of the cores, continuing with the results of the hydrochemical analysis, and the sedimentological analysis. It is followed by the results of the biogeochemical analysis and the biomarker analysis and ends with the last sub-chapter describing the results of the statistical analysis.

5.1. Core Description

In the following the cores will be described from the bottom to the top. The measurement of the depth below surface was started at the sediment surface for all cores, ignoring the water, ice, or snow cover at the different sites. There were three frozen and three unfrozen cores varying in their length between 12 cm and 219 cm (figure 5.1).

5.1.1. Unfrozen Cores

All three unfrozen cores are brown to dark brown in colour along their entire length and have an overall high share of silt.

The sample site of the marine core [TES22-MAR1-02], located at 70.8856° N, 153.6637° W, was covered by a 9 cm wide layer of snow, 165 cm of ice and 12 cm of water. The core has a total length of 12 cm. It has a high proportion of sand in the sediment and a thin organic band between 6 and 5.5 cm below surface level (b.s.l.).

The sample site of the core of the intact Lagoon sediment [TES22-LAG2-01], is located at 70.8776° N, 153.5088° W and was covered by a 112 cm wide layer of ice. The core is over its length of 31 cm only divided into two layers. The first one between 31 and 8 cm b.s.l. is brown coloured with visible macro-organic and different coloured inclusions. The upper layer between 8 and 0 cm b.s.l. has the same colour as the deeper layer, contains clayey silt with less visible macro-organic.

The core from the sediment beneath the thermokarst lake [TES22-TKL1-02] is with 54 cm the longest of the three unfrozen cores. It was sampled at 70.8362° N, 153.6628° W and the soil was covered by 29 cm of snow, 140 cm of ice and 80 cm of free water. It has a high silt and clay proportion and organic material in all layers. Moreover, there are peat inclusions between 50 and 28 cm b.s.l..

5.1.2. Frozen Cores

The frozen cores are longer than the unfrozen cores and have a more greyish colouring overall.

The sample site of the core of the semi-drained Lagoon basin [TES22-LAG1-01] is located at 70.8710° N, 153.6648° W and was covered with 27 cm of snow and 43 cm of ice. In total the core is 183 cm long. The deepest layers between 183 and 110.5 cm b.s.l. all consist of silt in different shades of grey and they all contain mussel shells. The ice content decreases upwards and there are oxidation spots, especially in the deeper layers. An undulated transition to the next upper layer suggests cryoturbation processes. The connecting layer between 110.5 and 97 cm b.s.l. of yellowish grey fine sand has ice veins and an organic inclusion between 103.5 and 102 cm b.s.l.. Between 97 and 77 cm b.s.l. connects an organic-rich blackish grey silt with fine sand and a few ice veins and above a yellowish grey sandy silt with no cryostructure or macro-organic. It is followed by a section of silty sediments changing from light grey to grey and yellowish grey with decreasing depth. All three layers have yellow oxidation spots and a networked ice structure. Between 63.5 and 46.5 cm b.s.l. mussel shells are visible. To it connects a dark grey, ice-poor clayey band with no cryostructure and above a 3 cm thick ice-rich organic band with structureless ice lenses. The upper part of the core is a 4 cm wide layer of light grey, ice-rich silt, passing on into a transition layer of sediment to ice.

The core from below the drained thermokarst lake basin [TES22-DLB1-01] is 219 cm long. The sample site was covered with 36 cm of snow and is located at 70.8544° N, 153.6639° W. The deepest layer, between 219 and 208 cm b.s.l. consists of grey silt with oxidation veins, is moderately ice-rich, containing ice lenses with a thickness up to 8 mm.

It is followed by a cryoturbated section of grey silt with a coarse ice structure and ice lenses with a thickness up to 2 cm mixed with material from the layer above. Above, between 198 and 191 cm b.s.l. is a layer of brown/grey silt with little ice and no visible cryostructure, but visible macro-organic. It connects to two layers of grey silt, decreasingly ice-rich between 191 and 161 cm b.s.l., with ice lenses up to 1 cm thickness, orange oxidation spots and veins, and sporadic macro-organic, followed by an orangish grey, ice-rich layer of silt with orange oxidation spots and vertical ice lenses. Between 139 and 23 cm b.s.l. layers of silt follow. They change colour and ice content from grey and very ice rich in the deeper parts to yellowish grey and moderately ice rich in the upper 7 cm. There are yellow and orange oxidation spots throughout all these layers. The cryostructure consists mainly of ice lenses with a thickness between 3 mm and 1 cm and there is a peat-inclusions between 68 and 56 cm b.s.l.. Between 23 and 21 cm b.s.l. is a layer of dark brown peat with few macro-organic and only a moderate ice content. Above are ice-rich layers of hazelnut brown peat in different decomposition states interrupted by a greyish dark brown sediment inclusion between 20 and 17 cm b.s.l.. The most upper layer is a 1.5 cm wide, greenish, ice-rich layer of moss.

The third frozen core, from the permafrost upland [TES22-UPL1-02], located at 70.8851° N, 153.7083° W, has a total length of 203 cm. The three deepest layers, between 203 and 62 cm b.s.l., all consists out of grey silt. There is a decreasing ice content, starting at approximately 90 % in the deepest layer, and the cryostructure changes from a networked cryostructure to horizontal ice lenses. In the two deepest layers sporadic macro-organic is visible and there are peat inclusions between 168 and 166 cm b.s.l. and 107.5 and 105 cm b.s.l. and in the layer above between 90 and 78 cm b.s.l.. Above connects a 12 cm thick layer of brownish dark grey silt. It is ice-poor, with few ice lenses in the direction of the silt layer. The section has visible macro-organic and organic inclusions. The upper three layers, starting at a depth of 50 cm b.s.l., consist of orange-grey silt. There is no visible cryostructure in the deeper part, but the ice content increases upwards, so the most upper layer, between 14 and 0 cm b.s.l., is the most ice-rich, including horizontal ice lenses. There is also an increase in oxidation between 50 and 24 cm b.s.l., turning over into a decrease from 24 cm b.s.l. to the soil surface.

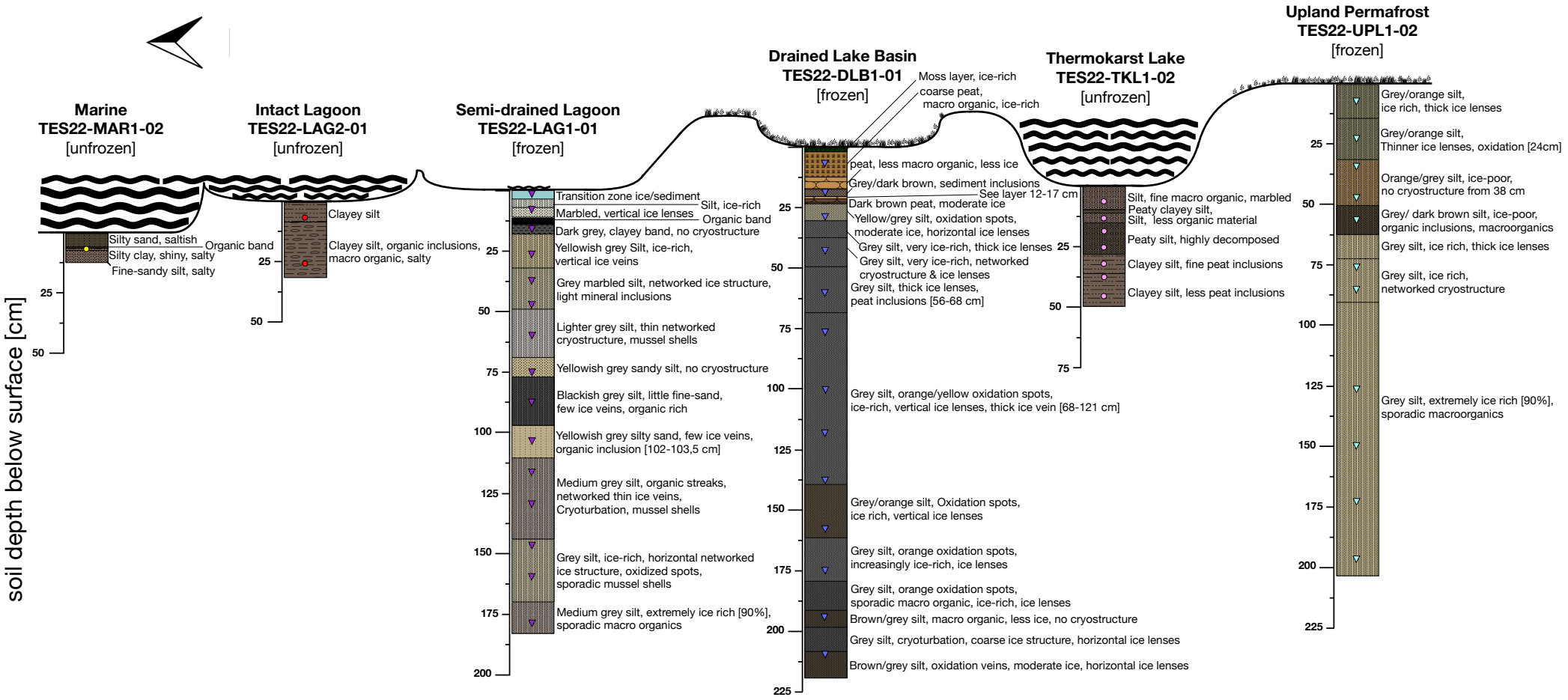

Figure 5.1: Stratigraphic core description for the UPL, TKL, DLB, SDLAG, LAG, and MAR profiles. Samples marked as points (unfrozen sediments) and Triangles (frozen sediments).

5.2. Hydrochemistry

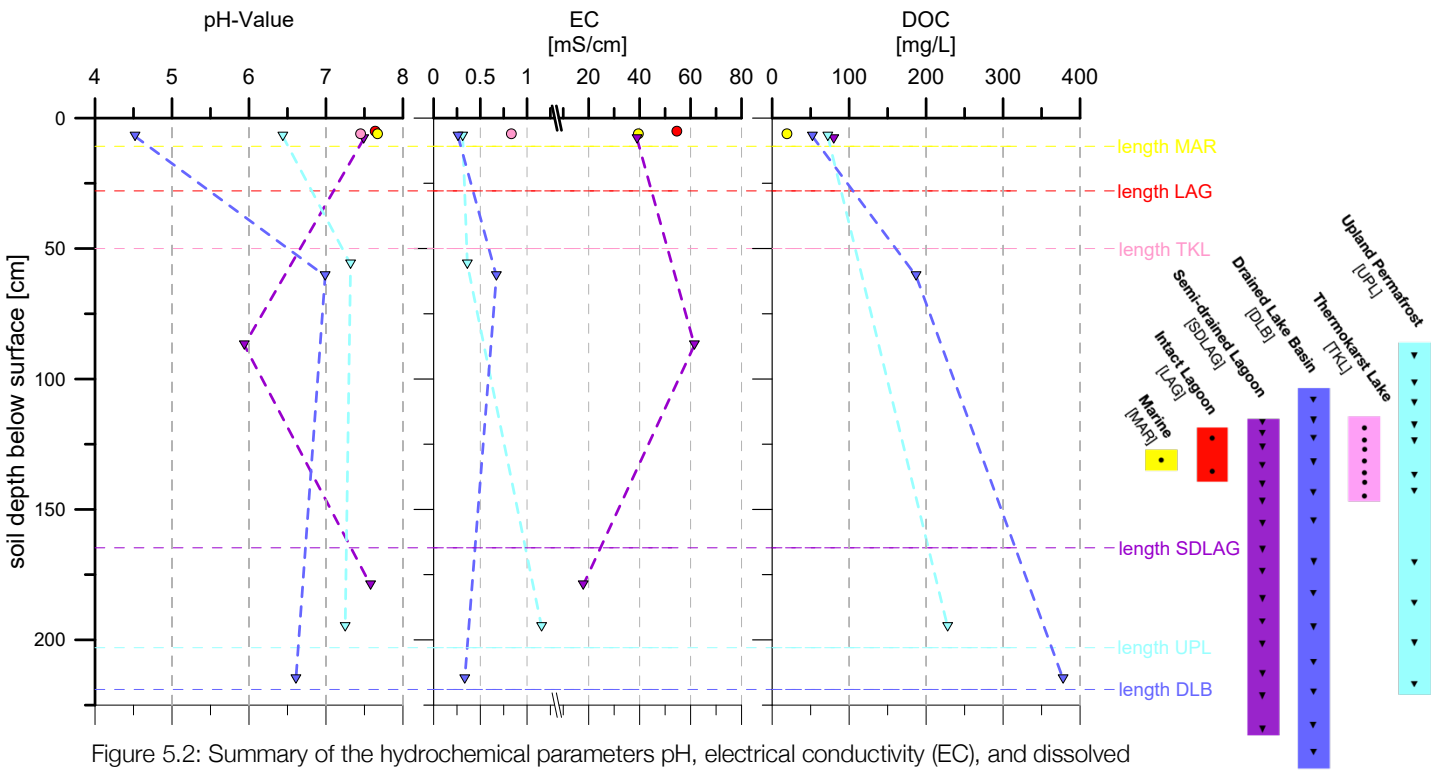

Figure 5.2: Summary of the hydrochemical parameters pH, electrical conductivity (EC), and dissolved organic carbon (DOC) for the UPL, TKL, DLB, SDLAG, LAG, and MAR profiles.

5.2.1. Hydrochemistry - Upland Permafrost (UPL)

The pH profile within the upland-core (UPL), shows distinct variations. In total three porewater samples of this core were analysed. The deepest sample, from a mean depth of 195 cm b.s.l., has a pH of 7.25, which is increasing to 7.32 in the sample from a mean depth of 56 cm b.s.l., and decreasing to the topsoil to a pH value of 6.44 (figure 5.2). Throughout the entire length of the core the electric conductivity (EC) remains low. The porewater of the deepest sample has an EC of 1156 µS/cm. This value is decreasing towards the topsoil reaching an EC of 311 µS/cm (figure 5.2). The determination of dissolved organic carbon (DOC) was limited to porewater from two samples: the deepest sample, from 195 cm b.s.l. mean depth, and the topsoil from a mean depth of 7 cm b.s.l.. The deep sample has a DOC content of 228 mg/L, representing a higher concentration compared to the topsoil sample, with a decreased DOC content of 72.3 mg/L (figure 5.2).

5.2.2. Hydrochemistry - Thermokarst Lake (TKL)

Only one porewater sample from the thermokarst lake (TKL) deposits, from a mean depth of 6 cm b.s.l., was analysed. The sampled porewater has a pH value of 7.45 (figure 5.2).

The EC is with 832 µS/cm low (figure 5.2). The DOC content could not be measured due to a shortage of porewater.

5.2.3. Hydrochemistry - Drained Lake Basin (DLB)

In total three samples were analysed from the core of the drained lake basin (DLB). The pH values in the deeper samples, at mean depths of 215 cm b.s.l. and 60.5 cm b.s.l. are with 6.61 and 6.99 relatively similar, but it decreases in the topsoil sample, at a mean depth of 6.75 cm b.s.l., and reaches an alkaline pH value of 4.52 (figure 5.2). As for the other non-marine influenced cores the EC is low over the entire length of the core. Starting by 333 µS/cm in the deepest sample, increasing to 672 µS/cm in the middle section and decreasing in the topsoil sample to 261.5 µS/cm (figure 5.2). The DOC content of the DLB core decreases throughout the length of the core. A high content of 378 mg/L was measured in the porewaters of the deepest sample, decreasing to 187 mg/L in the middle part and reaching 52.3 mg/L in the porewater of the topsoil (figure 5.2).

5.2.4. Hydrochemistry - Semi-drained Lagoon (SDLAG)

From the core of the semi-drained lagoon (SDLAG) in total three samples were analysed in the porewater analysis. The deepest sample, from a mean depth of 179 cm b.s.l., has a pH value of 7.58. It decreases in the sample of the middle part of the core to a pH value of 5.94 and increases again in the sample of the top of the core, from a mean depth of 7.75 cm b.s.l., to a pH of 7.49 (figure 5.2). The EC is lowest in the deepest sample with 17.85 mS/cm, increases to 61.6 mS/cm at a mean depth of 87 cm b.s.l. and decreases in the upper soil to 39 mS/cm (figure 5.2). The only DOC content measured, from a mean depth of 7.75 cm b.s.l., is 80.8 mg/L (figure 5.2).

5.2.5. Hydrochemistry - Intact Lagoon (LAG)

One porewater sample of the intact lagoon (LAG) was hydrochemically analysed. The porewater of the sediment from a mean depth of 5 cm b.s.l. has a pH value of 7.64 (figure 5.2). The EC is 54.6 mS/cm and DOC could not be measured due to a shortage of porewater from the sample (figure 5.2).

5.2.6. Hydrochemistry - Marine (MAR)

As for the other unfrozen cores only one porewater sample was analysed from the marine core (MAR) from a mean depth of 6.25 cm b.s.l.. The measured pH value is 7.67, the EC is 39.5 mS/cm, and the DOC content is 19.2 mg/L (figure 5.2).

5.3. Sedimentology

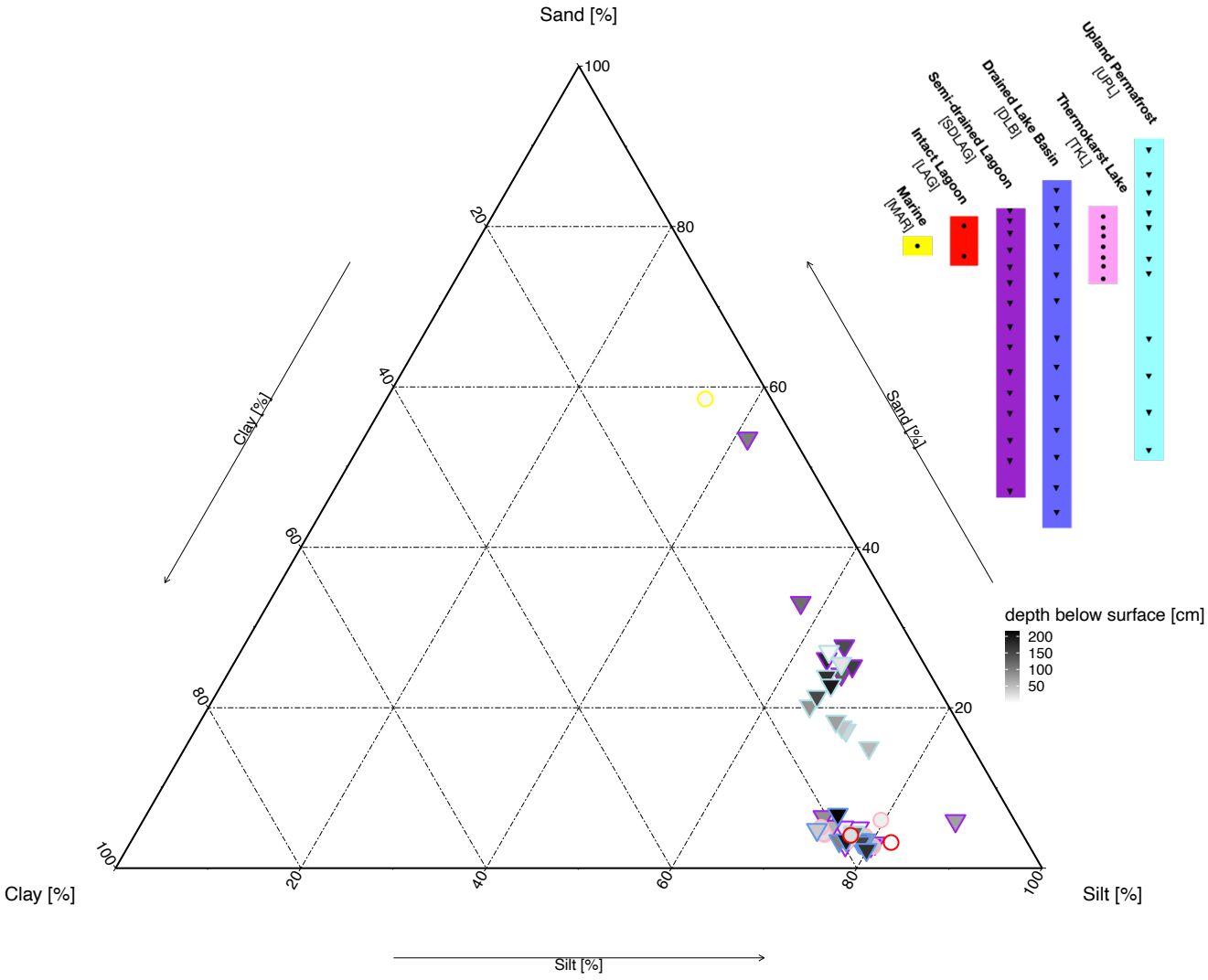

Figure 5.3: Soil triangle showing the grainsize distribution of the UPL, TKL, DLB, SDLAG, LAG, and MAR profiles, with circles for unfrozen sediments and triangles for frozen sediments and a colour gradient over depth.

5.3.1. Sedimentology - Upland Permafrost (UPL)

The upland permafrost core is generally dominated by silt, with a percentage share varying between 63.48 % and 77.5 % (figure 5.3). Except for the sample at 126 cm b.s.l. mean depth, clay has the smallest share of sediments in the samples.

The mean grain size ranges between 6.5 µm at 126 cm b.s.l. and 21.73 µm at 7 cm b.s.l. (table 5.1). It decreases between the deepest sample at 195 cm b.s.l. and the sample at 126 cm b.s.l. and then increases to the uppermost sample, intermitted by the sample at 56 cm b.s.l. mean depth in which the mean grain size decreases compared to the deeper sample (figure 5.6).

The ice content of the UPL samples has strong variations, ranging between 20.75 wt% at a mean depth of 47.5 cm b.s.l. and 67.34 wt% at a mean depth of 149.5 cm b.s.l. (table 5.2). The mean ice content of the core is 46.10 wt% (table 5.2). It is higher in the deeper samples, between 195 and 56 cm b.s.l. mean depth, being ≥ 52.89 wt% and lower in the upper samples, between 47.5 and 7 cm b.s.l. mean depth, staying ≤ 37.5 wt%.

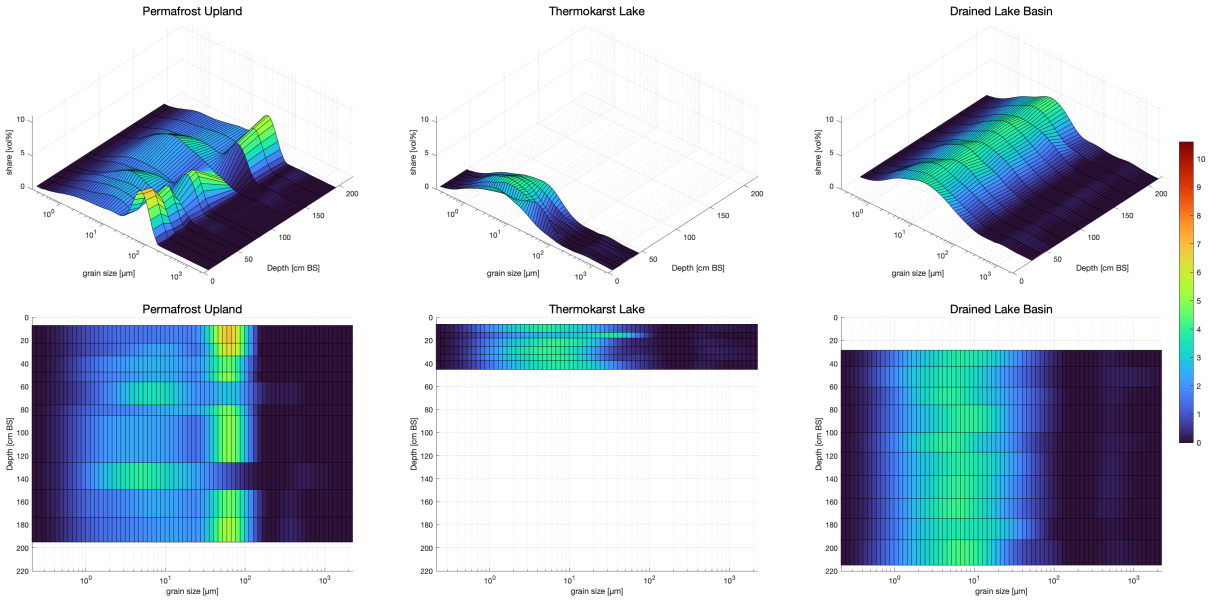

Figure 5.4: Grainsize distribution over depth in a 3D view (upper row) and in a flat view (lower row) of the UPL, TKL and DLB profiles (from left to right).

The dry bulk density is being lowest in the sample at 149.5 cm b.s.l. with 0.38 g/cm^3 and highest at 47.5 cm b.s.l. with 1.51 g/cm^3 (table 5.3). It has only little variation between samples taken between 201 and 50 cm b.s.l., ranging between 0.38 g/cm^3 and 0.59 g/cm^3 (figure 5.6). In the upper samples of the core the dry bulk density stays between 1.51 g/cm^3 and 1.03 g/cm^3 (figure 5.6). The mean dry bulk density of the UPL core is 0.83 g/cm^3 (table 5.3).

Table 5.1: Statistical parameter mean grain size [µm].

Statistical Parameter	UPL	TKL	DLB	SDLAG	LAG	MAR
maximum	21.73	9.93	6.74	45.87	6.78	33.31
minimum	6.5	5.22	5.7	5.00	6.02	N/A
mean	15.01	6.56	6.26	14.8	N/A	N/A
median	14.3	5.75	6.38	6.88	N/A	N/A

Table 5.2: Statistical parameter absolute water/ice content [wt%].

Statistical Parameter	UPL	TKL	DLB	SDLAG	LAG	MAR
maximum	67.34	51.93	95.24	53.41	41.25	19.62
minimum	20.75	37.96	27.93	3.41	36.99	N/A
mean	46.10	42.70	59.63	23.39	N/A	N/A
median	54.96	42.06	60.81	22.94	N/A	N/A

Table 5.3: Statistical parameter dry bulk density [g/cm^3].

Statistical Parameter	UPL	TKL	DLB	SDLAG	LAG	MAR
maximum	1.51	1.06	1.25	1.53	0.98	1.69
minimum	0.38	0.71	0.05	0.61	N/A	1.36
mean	0.83	N/A	0.54	1.23	N/A	N/A
median	0.59	N/A	0.48	1.32	N/A	N/A

5.3.2. Sedimentology - Thermokarst Lake (TKL)

The sediment samples of the thermokarst lake are dominated by silt, with a share ranging between 73.55 % and 80.37 % (figure 5.3). There is only a very small share of sand in all samples, varying between 2.7 % and 6 % (figure 5.3). The grain size distribution is relatively homogenous over the length of the core with a slight shift towards coarser deposits between 10 and 16 cm b.s.l. (figure 5.4). The mean grain size in the samples varies between 9.93 µm at 13 cm b.s.l. and 5.22 µm at 25.5 cm b.s.l. (table 5.1). The mean grain size of all samples of the TKL core is 6.56 µm (table 5.1).

The mean absolute water content of all TKL samples is 42.7 wt% (table 5.2). It varies between 37.96 wt% in the deepest sample at a mean depth of 45.25 cm b.s.l. and 51.93 wt% in the uppermost sample at 6 cm b.s.l. (table 5.2).

The bulk density was measured in two depths, at 3 cm b.s.l. and 49 cm b.s.l.. The deeper sample has a bulk density of 1.06 g/cm^3. It decreases in the upper sample to 0.71 g/cm^3 (figure 5.6).

5.3.3. Sedimentology - Drained Lake Basin (DLB)

The grain size analysis (gsa) of the drained thermokarst lake basin started at a mean depth of 28.5 cm b.s.l., since the upper two samples had too much organic material to perform the gsa. The highest share of sediments has silt, ranging between 73.31 % and 79.91 % and the smallest share has sand, ranging between 6.7 % and 2.3 % (figure 5.3). The mean grain size of all the samples of the core is 6.26 µm (table 5.1). As shown in figure 5.4 the grain size distribution has only very little variation throughout the core, with mean grain sizes varying between 5.7 µm at a mean depth of 193 cm b.s.l. and 6.74 µm at a mean depth of 76 cm b.s.l. (table 5.1).

The absolute ice content in the samples shows strong variations between a maximum of 95.24 wt% in the uppermost sample at a mean depth of 6.75 cm b.s.l. and a minimum of 27.93 wt% in the sample from the mean depth of 28.5 cm b.s.l. (table 5.2). It has less variation in the samples taken between 215 and 42.5 cm b.s.l., varying between 43.71 wt% and 68.25 wt%. In total the DLB core has a high mean absolute ice content of 59.63 wt% (table 5.2).

The dry bulk density is high in the samples from 215 cm b.s.l. mean depth with 0.82 g/cm^3, from 157 cm b.s.l. mean depth with 0.73 g/cm^3, and from 28.5 cm b.s.l. mean depth with 1.25 g/cm^3 (figure 5.6). It is lowest in the two uppermost samples with 0.05 g/cm^3 and 0.25 g/cm^3, as well as at 117 cm b.s.l. mean depth with 0.37 g/cm^3, and 76 cm b.s.l. mean depth with 0.39 g/cm^3 (figure 5.6). The mean dry bulk density of the sample of the DLB core is 0.54 g/cm^3 (table 5.3).

5.3.4. Sedimentology - Semi-drained Lagoon (SDLAG)

As shown in figure 5.5 the grain size distribution of the semi drained lagoon has a shift from higher shares of larger grainsizes in the deeper part of the core, up to 100 cm b.s.l., to smaller grain sizes in the upper part. Moreover, the samples taken between 181 and 103 cm b.s.l. are not clearly dominated by one soil type (figure 5.3). Except for one sample from 103 cm b.s.l. mean depth, silt has the highest share of sediment, varying between 57.35 % and 66.86 % (figure 5.3). The other soil type with a high share in those samples is sand, ranging between 24.2 % and 33.1 % (figure 5.3). The sample from 103 cm b.s.l. mean depth is the only sample of the core in which sand has with 53.6 % the highest share of sediments, followed by silt with 41.39 % (figure 5.3). Samples from the upper 90 cm of the core are clearly dominated by silt, having shares ranging between 73.22 % and 87.72 % (figure 5.3). In these samples, clay makes up the second largest share and sand the smallest. The mean grain size of all samples of the core is 14.8 µm, it varies between

5.0 µm at a mean depth of 1.5 cm b.s.l. and 45.87 µm at a mean depth of 103 cm b.s.l. (table 5.1).

The absolute ice content has strong variations, between 3.41 wt% at 36.5 cm b.s.l. mean depth and 53.41 wt% at 7.75 cm b.s.l. mean depth (table 5.2). The mean absolute ice content of all samples of SDLAG is 23.39 wt% (table 5.2).

The dry bulk density was only calculated for 9 out of 14 samples, since the ice content does not meet the requirement of the calculation to be ≥ 20 wt% in 5 samples. There is only little variation in the bulk density, except for the uppermost sample at 7.75 cm b.s.l. mean depth with 0.61 g/cm^3 (figure 5.6). The dry bulk density for the rest of the samples varies between 1.06 g/cm^3 and 1.53 g/cm^3 (figure 5.6).

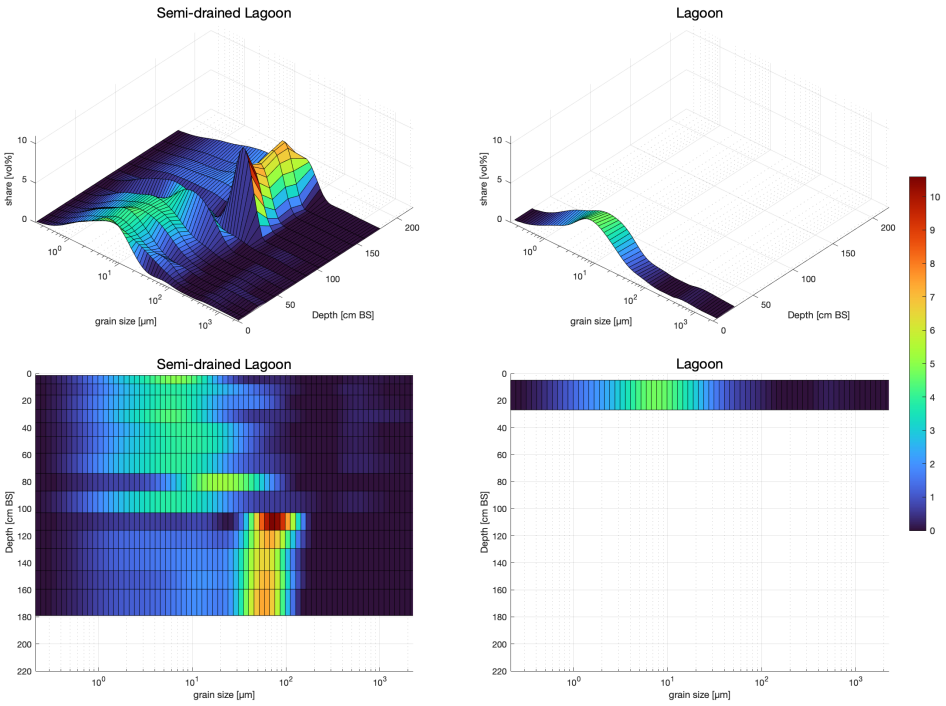

Figure 5.5: Grainsize distribution over depth in a 3D view (upper row) and in a flat view (lower row) of the SDLAG, and LAG profiles (from left to right).

5.3.5. Sedimentology - Intact Lagoon (LAG)

Only two samples of the lagoon core, from 5 and 27 cm b.s.l. mean depth, were sedimentologically analysed. As shown in figure 5.5 both samples are similar in their grain size distribution, with silt having the highest share of sediments in both samples (figure 5.3). The mean grain size is 6.02 µm in the deeper sample and 6.78 µm in the higher sample (table 5.1).

The absolute water content is with 36.99 wt% lower in the deeper sample than in the upper sample with 41.25 wt% (table 5.2).

The dry bulk density, measured in one sample at 8.25 cm b.s.l. mean depth, is 0.98 g/cm^3 (table 5.3).

5.3.6. Sedimentology - Marine (MAR)

Due to the short length of the marine core only one sample of the marine core was sedimentologically analysed from a mean depth of 6.25 cm b.s.l.. Sand has with 58.5% the highest share of the sediments, followed by silt with 34.42%, and clay with 7.13% (figure 5.3). The mean grain size is 33.31 µm (table 5.1).

The measured absolute water content of the sample is 19.62 wt% (table 5.2).

The bulk density, measured within two samples, is 1.69 g/cm^3 in the deeper sample at 9.5 cm b.s.l. and 1.36 g/cm^3 at 1 cm b.s.l. mean depth (table 5.3).

5.4. Biogeochemistry

The results of the biogeochemical analysis include the TOC content [wt%], the calculated TOC density [$kg_{TOC}m^{-3}$], the TN content [wt%], the TOC/TN ration, the $\delta^{13}C$ ratio [‰ vs. VPDB], the measured mercury content [µg/kg], and the results of the radiocarbon dating [cal yr BP].

5.4.1. Biogeochemistry - Upland Permafrost (UPL)

The TOC content in the upland permafrost core has the strongest variation between 100 and 40 cm b.s.l. (figure 5.6). It starts with 1.26 wt% in the deepest sample and stays below 2.5 wt% to a depth of 100 cm b.s.l. (figure 5.6). It fluctuates in the next upper centimetres and reaches a peak of 20.42 wt% at a depth of 56 cm b.s.l. (figure 5.6). After the peak the TOC content decreases rapidly towards the top of the soil and stays between 3.3 wt% and 2.5 wt% in the upper 30 cm of the core (figure 5.6). The mean TOC content of the core is 4.66 wt% (table 5.4).

The TOC density follows the same trend as the TOC content with a stronger decrease between the samples in 23 cm b.s.l. and the top sample in a depth of 7 cm b.s.l. (figure 5.6). The range of the TOC density is 6.79 $kg_{TOC}m^{-3}$ to 119.67 $kg_{TOC}m^{-3}$ (table 5.5).

The TN content of the UPL core also follows a similar pattern as the TOC content, varying between < 0.1 wt% and 1.2 wt% (figure 5.6).

The TOC/TN ratio is with 11.4 low in the deepest sample and has a peak of 30.64 just above at a depth of 173.5 cm b.s.l. (figure 5.6). Above 125 cm b.s.l. there is only little variation in the ratio, varying between 16.8 and 21.4 (figure 5.6).

The $\delta^{13}C$ ratio continuously decreases from the deepest sample towards the upper soil (figure 5.6). There is a stronger decrease from 195 to 150 cm b.s.l. and between 55 and 30 cm b.s.l. (figure 5.6). The values vary in a range between -26.1 ‰ vs. VPDB and -29.03 ‰ vs. VPDB, with a mean of -27.75 ‰ vs. VPDB (table 5.8).

The mercury content is lower in the deeper samples between 195 and 76 cm b.s.l. mean depth, ranging between 25.9 µg/kg and 36.34 µg/kg, and higher in the upper samples, ranging between 66.24 µg/kg and 48.51 µg/kg (figure 5.6). The mean mercury content of all samples is 40.16 µg/kg (table 5.9).

The radiocarbon dating was carried out for two samples of the core. At a mean depth of 195 cm b.s.l. an age of 9000 cal yr BP was determined. The deposits of the upper sample, from a mean depth of 22.5 cm b.s.l., are classified as recent.

Table 5.4: Statistical parameter TOC content [wt%].

Statistical Parameter	UPL	TKL	DLB	SDLAG	LAG	MAR
maximum	20.42	6.23	37.62	4.62	4.68	1.3
minimum	1.26	4.63	2.94	0.72	4.09	N/A
mean	4.66	5.37	7.57	2.37	N/A	N/A
median	3.20	5.31	3.26	2.79	N/A	N/A

Table 5.5: Statistical parameter TOC density [$kg_{TOC}m^{-3}$].

Statistical Parameter	UPL	TKL	DLB	SDLAG	LAG	MAR
maximum	119.67	62.01	51.88	49.87	45.70	19.83
minimum	6.79	33.02	11.48	9.2	39.99	N/A
mean	36.66	46.31	25.06	26.36	N/A	N/A
median	26.38	44.46	16.97	21.34	N/A	N/A

Table 5.6: Statistical parameter TN content [wt%].

Statistical Parameter	UPL	TKL	DLB	SDLAG	LAG	MAR
maximum	1.2	0.42	0.99	0.33	0.36	< 0.1
minimum	< 0.1	0.34	0.22	< 0.1	0.31	N/A
mean	0.29	0.37	0.36	0.25	N/A	N/A
median	0.17	0.37	0.25	0.26	N/A	N/A

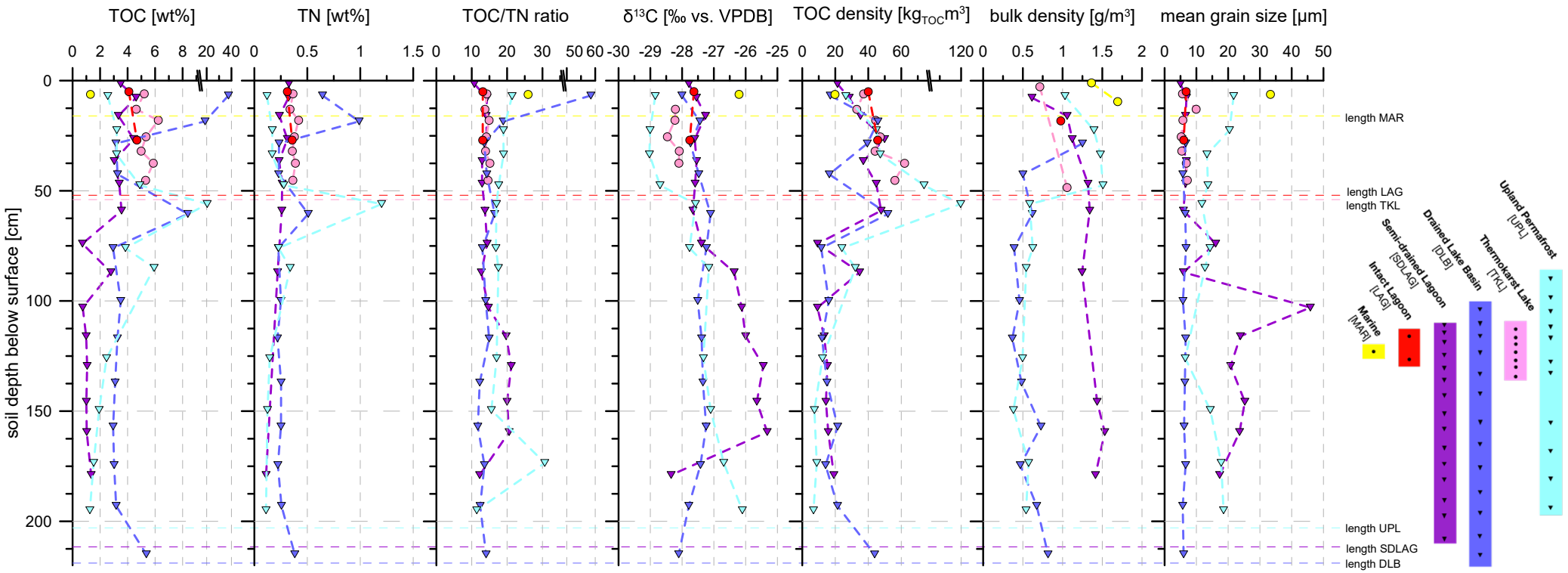

Figure 5.6: Summary of the biogeochemical parameters of the UPL, TKL, DLB, SDLAG, LAG, and MAR profiles, with circles for unfrozen sediments and triangles for frozen sediments.

5.4.2. Biogeochemistry - Thermokarst Lake (TKL)

The TOC content of the core of the thermokarst lake sediment shows an alternation of decreasing and increasing values over the whole length of the core (figure 5.6), but within a small range between 4.63 wt% and 6.23 wt% and a mean of 5.37 wt% (table 5.4).

The highest TOC density is 62.01 $kg_{TOC}m^{-3}$ in the sample of a depth of 37.5 cm b.s.l. (table 5.5). The lowest TOC densities have the two samples from the top, at 13 cm b.s.l. and 6 cm b.s.l., containing 33.02 $kg_{TOC}m^{-3}$ and 37.18 $kg_{TOC}m^{-3}$ (figure 5.6).

The general pattern of the TN content follows the pattern of the TOC content and ranges between 0.34 wt% and 0.42 wt% (table 5.6).

The same applies to the TOC/TN ratio following the trend of the TOC and the TN content, but only varying in the small range between 13.73 and 15.14 (table 5.7).

$\delta^{13}C$ was only measured between 13 and 37.5 cm b.s.l.. This parameter also shows only little variation, with values varying between -28.09 ‰ vs. VPDB and -28.46 ‰ vs. VPDB and a mean of -28.22 ‰ vs. VPDB (table 5.8).

The TKL samples have a high mercury content with only little variation (figure 5.6). The minimum concentration of 64.1 µg/kg was measured at a mean depth of 13 cm b.s.l. and the maximum concentration of 77.85 µg/kg was measured in the uppermost sample at 6 cm b.s.l. mean depth. The mean mercury content of the TKL core is 70.74 µg/kg (table 5.9).

The radiocarbon determination was carried out for two samples relatively close to each other at mean depths of 37.5 cm b.s.l. and 13 cm b.s.l., resulting in similar ages of 4240 cal yr BP and 4600 cal yr BP.

Table 5.7: Statistical parameter TOC/TN ratio.

Statistical Parameter	UPL	TKL	DLB	SDLAG	LAG	MAR
maximum	30.64	15.14	58.46	21.18	13.14	25.93
minimum	11.42	13.73	11.72	10.73	13.1	N/A
mean	18.45	14.39	17.5	15.23	N/A	N/A
median	17.54	14.28	13.95	14.26	N/A	N/A

Table 5.8: Statistical parameter $\delta^{13}C$ [‰ vs. VPDB].

Statistical Parameter	UPL	TKL	DLB	SDLAG	LAG	MAR
maximum	-26.1	-28.09	-27.1	-25.32	-27.63	-26.21
minimum	-29.03	-28.46	-28.11	-28.34	-27.76	N/A
mean	-27.75	-28.22	-27.52	-26.91	N/A	N/A
median	-27.58	-28.21	-27.44	-27.39	N/A	N/A

Table 5.9: Statistical parameter Mercury [µg/kg].

Statistical Parameter	UPL	TKL	DLB	SDLAG	LAG	MAR
maximum	66.24	77.85	103.55	102.17	70.67	30.68
minimum	25.9	64.1	48.78	15.57	66.63	N/A
mean	40.16	70.74	69.87	52.18	N/A	N/A
median	36.34	70.63	68.9	61.14	N/A	N/A

5.4.3. Biogeochemistry - Drained Lake Basin (DLB)

The soil core of the drained thermokarst lake basin has a wide range of the TOC content, with values varying between 2.94 wt% and 37.62 wt% (table 5.4). After the deepest sample at 215 cm b.s.l., with a TOC content of 5.36 wt%, the TOC content decreases and stays between 2.94 wt% and 3.5 wt% between 193 and 25 cm b.s.l., with an outlier at a depth of 60.5 cm b.s.l. where it increases to 8.38 wt% (figure 5.6). High TOC contents of 37.62 wt% and 18.71 wt% were measured in the upper 20 cm of the soil (figure 5.6).

The TOC density follows in the deeper layers the same trend as the TOC content (figure 5.6). There is a decrease from 43.84 $kg_{TOC}m^{-3}$ to 21.37 $kg_{TOC}m^{-3}$ between 215 and 193 cm b.s.l. (figure 5.6). It is followed by the part with only little variation, between 21.37 $kg_{TOC}m^{-3}$ and 11.99 $kg_{TOC}m^{-3}$, with the outlier at a depth of 60.5 cm b.s.l. where TOC density reaches 51.88 $kg_{TOC}m^{-3}$ (figure 5.6). In contrast to the TOC content is there an increase of the TOC density in the sample from a depth of 28.5 to 18.5 cm b.s.l. to values of 39.42 $kg_{TOC}m^{-3}$ and 45.88 $kg_{TOC}m^{-3}$ followed by a decrease in the uppermost sample to 16.97 $kg_{TOC}m^{-3}$ (figure 5.6).

The same is true for the TN content, following the pattern of the TOC content, with the difference that it decreases in the uppermost sample, at a mean depth of 6.75 cm b.s.l. (figure 5.6). The range is between 0.22 wt% and 0.99 wt%, with a mean of 0.36 wt% (table 5.6).

The TOC/TN ratio also follows the pattern of the TOC content, but stays in a relatively narrow range, between 11.72 and 18.92, except for the uppermost sample were the ratio strongly increases to 58.46 (figure 5.6).

The $\delta^{13}C$ values decrease slightly in the deepest 70 cm from -28.11 ‰ vs. VPDB to -27.24 ‰ vs. VPDB (figure 5.6). In the following 140 cm is only little variation with values staying between -27.73 ‰ vs. VPDB and -27.10 ‰ vs. VPDB and a slight decrease in the shallowest sample to -28.01 ‰ vs. VPDB (figure 5.6).

The DLB core has a very high maximum concentration of mercury of 103.55 µg/kg at 18.5 cm b.s.l. mean depth and a minimum concentration of 48.78 µg/kg in the uppermost

sample at 6.75 cm b.s.l. mean depth (table 5.9). The mercury content in the samples below shows only little variations ranging between 63.87 µg/kg and 72.14 µg/kg (figure 5.6). The mean mercury concentration of the DLB deposits is 69.87 µg/kg (table 5.9).

The determined age of the deposits from mean depth of 193 cm b.s.l. is 645 cal yr BP and at a mean depth of 21.5 cm b.s.l. the deposits are classified as recent.

5.4.4. Biogeochemistry - Semi-drained Lagoon (SDLAG)

The TOC content in the core of the semi-drained lagoon is low with only little variation, between 1.35 wt% and 0.74 wt%, in the deepest 70 cm of the core (figure 5.6). Between a depth of 100 and 50 cm b.s.l. it shows more variation ranging between 0.72 wt% and 3.56 wt% (figure 5.6). The upper 50 cm of the core shows a generally higher TOC content than the deeper layers with values ranging from 3.03 wt% to 4.62 wt% (figure 5.6). The calculated mean TOC content in the core is 2.37 wt% (table 5.4).

The TOC density in the core follows the same pattern as the TOC content, but with the difference that it continuously decreases in the upper 30 cm, from 49.87 $kg_{TOC}m^{-3}$ to 21.34 $kg_{TOC}m^{-3}$ (figure 5.6). Over the complete length of the core values vary between 9.2 $kg_{TOC}m^{-3}$ and 49.87 $kg_{TOC}m^{-3}$ with a mean TOC density of 26.36 $kg_{TOC}m^{-3}$ (table 5.5).

The TN content is in 6 out of the 15 samples lower than 0.1 wt%. In general, the progression over the length of the core is the same as for the TOC content, with the narrow range of < 0.1 wt% to 0.33 wt% (table 5.6).

Following a TOC/ TN ratio of 12.24 in the deepest sample, at a depth of 179 cm b.s.l., the ratio increases and stays between 19.73 and 21.18 in the 50 cm above (figure 5.6). In the next upper layer, it decreases again, varying between 12.7 and 14.72, until the uppermost sample for which the lowest value of 10.73 was calculated.

The $\delta^{13}C$ ratio also shows a strong increase between the deepest sample and the one above from -28.24 ‰ vs. VPDB to -25.32 ‰ vs. VPDB (figure 5.6). In the further course of the core it continuously decreases, with slight deviations into the other direction, until it reaches -27.79 ‰ vs. VPDB in the uppermost sample.

The mercury content in the SDLAG samples has strong variations ranging between 19.6 µg/kg at a mean depth of 159.5 cm b.s.l. and 102.17 µg/kg at a mean depth of 26.5 cm b.s.l. (figure 5.6). The mean mercury content of all SDLAG samples is 52.18 µg/kg (table 5.9).

The radiocarbon determination of the SDLAG deposits resulted in an age determination of 41962 cal yr BP at a mean depth of 179 cm b.s.l. and a classification as recent for deposits of a mean depth of 16 cm b.s.l..

5.4.5. Biogeochemistry - Intact Lagoon (LAG)

The TOC content decreased from the deeper sample, at a mean depth of 27 cm b.s.l. to the upper sample at a mean depth of 5 cm b.s.l., from 4.68 wt% to 4.09 wt%. TOC density and TN content follow the same pattern as the TOC content, with the density decreasing from 45.7 $kg_{TOC}m^{-3}$ to 39.99 $kg_{TOC}m^{-3}$ and the TN decreasing from 0.36 wt% to 0.31 wt% (figure 5.6). The TOC/TN ratio is very slightly increasing from the deeper sample to the top, from 13.1 to 13.14 (figure 5.6). Same accounts for $\delta^{13}C$ ratio, changing from -27.76 ‰ vs. VPDB to -27.63 ‰ vs. VPDB in the upper sample. Mercury concentration is higher in the deeper sampler with 70.67 µg/kg and decreases in the upper sample to 66.63 µg/kg. The deposits of the LAG core at a mean depth of 11.25 cm b.s.l., have a determined age of 2410 cal yr BP.

5.4.6. Biogeochemistry - Marine (MAR)

The TOC content of the marine sample, from a mean depth of 6.25 cm b.s.l., is with 1.3 wt% rather low (figure 5.6). Same applies to the TOC density of 19.83 $kg_{TOC}m^{-3}$, the TN content of < 0.1 wt%, and the mercury concentration of 30.68 µg/kg (figure 5.6). In contrast the TOC/TN ratio of 25.93, as well as the $\delta^{13}C$ value of -26.21 ‰ vs. VPDB are relatively high compared to samples of the other cores from a similar depth (figure 5.6). The radiocarbon determination was carried out with a sample from a mean depth of 6 cm b.s.l. and resulted in an age of 16061 cal yr BP.

5.5. Biomarker Analysis

Due to the small data set of 15 samples in total for the biomarker analysis, the following chapter is not divided into sub-chapters describing the individual cores, but the results of all cores are described together.

The highest total concentration of *n*-alkanes is 1090.31 $\mu g/g_{TOC}$ and was measured in the deepest analysed sample of the drained thermokarst lake basin (DLB) at a depth of 208 cm b.s.l. (figure 5.9). The lowest concentration of *n*-alkanes of 61.89 $\mu g/g_{TOC}$ was measured in the marine (MAR) sample at a depth of 6.25 cm b.s.l. (figure 5.9). For the samples of the lagoon (LAG), the thermokarst lake (TKL), and the DLB a decreasing trend of total *n*-alkane concentration from the deepest to the uppermost sample is visible (figure 5.9). The semi-drained lagoon (SDLAG) and the upland permafrost (UPL) core have higher concentrations in the deeper samples than in the upper ones (figure 5.9).

5.5.1. Average Chain Length

All values for the average chain length for short chain *n*-alkanes (ACL-short) across the cores, are in a very narrow range (figure 5.7). The highest value for the index has the deep sample of the LAG core with 20.11 and the lowest value of 19.49 was calculated for the deepest UPL sample, in a mean depth of 165.5 cm b.s.l. (figure 5.7). Also, within the individual cores, there is not much variation (figure 5.7).

The average chain lengths of long chain *n*-alkanes (ACL-long) are highest in the three samples of the UPL core, with the highest value of 28.73 in the sample from the middle part (figure 5.7). Lowest values have the LAG and the MAR samples, with the lowest at a depth of 6.25 cm b.s.l. from the MAR core with 26.2 (figure 5.7). All cores with more than one sample show a decrease of the ACL-long from the samples taken between 100 and 25 cm b.s.l., to the samples in the uppermost 10 cm b.s.l. (figure 5.7).

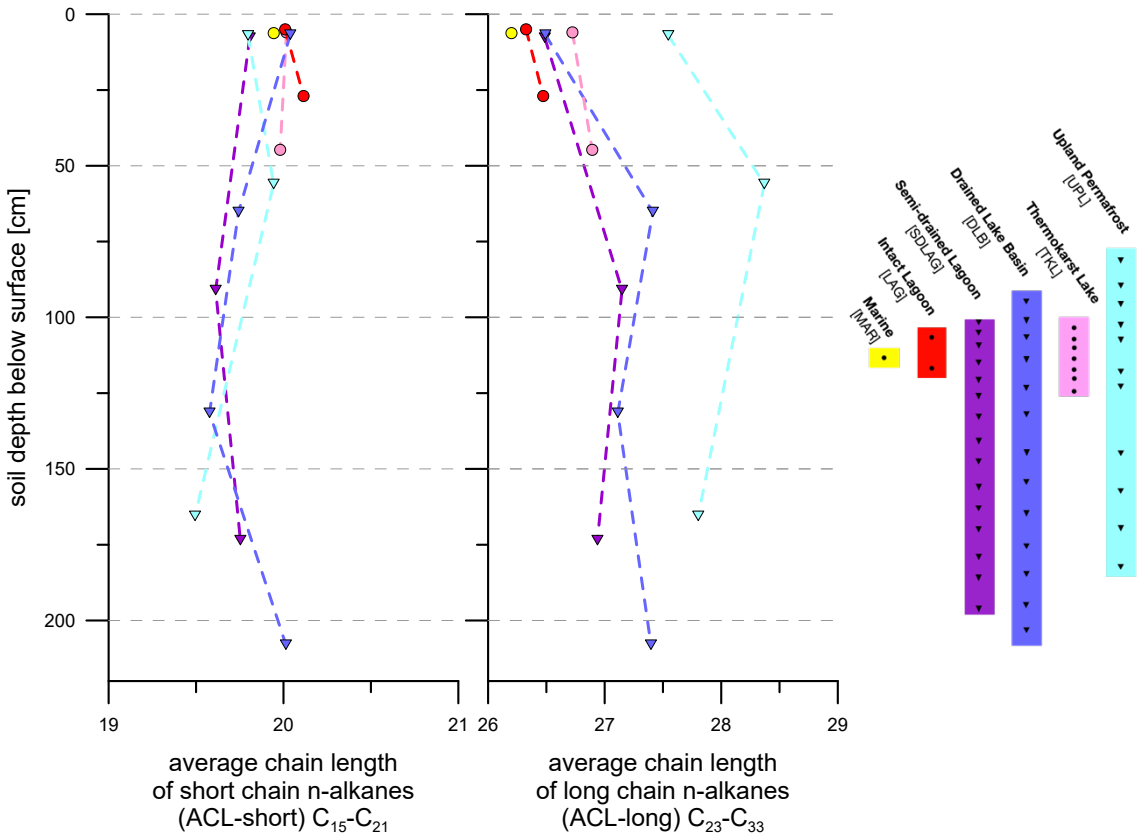

Figure 5.7: Average chain length of *n*-alkanes short (C_{15}-C_{21}) and long (C_{23}-C_{33}) of the UPL, TKL, DLB, SDLAG, LAG, and MAR profiles, with circles for unfrozen sediments and triangles for frozen sediments.

5.5.2. P_{aq} & P_{wax}

As shown in figure 5.8 the highest P_{aq} values were measured in the MAR sample and the uppermost DLB sample, both having a P_{aq} of 0.66. The MAR sample also has the lowest

P_{wax} of 0.52 indicating an aquatic influence (figure 5.8). Also, the uppermost DLB sample shows a relatively low P_{wax} of 0.56 (figure 5.8). Other samples with high P_{aq} and low P_{wax} are both LAG samples, with a P_{aq} between 0.61 and 0.64 and a P_{wax} between 0.54 and 0.55, and the uppermost SDLAG sample with a P_{aq} of 0.62 and a P_{wax} of 0.53 (figure 5.8).

The highest P_{wax} values were calculated for all UPL samples, ranging between 0.76 and 0.74 (figure 5.8). At the same time, they show the lowest P_{aq} values, varying between 0.31 and 0.39 (figure 5.8). Another sample with a high P_{wax} of 0.73 and a low P_{aq} of 0.41 is the DLB sample from a mean depth of 65.25 cm b.s.l. (figure 5.8).

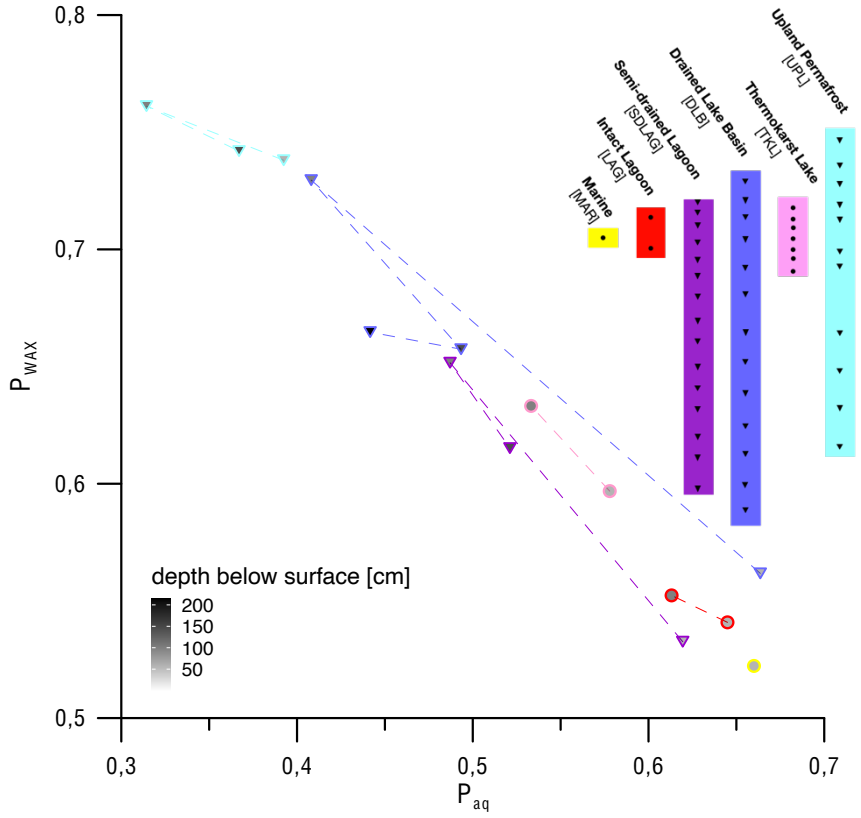

Figure 5.8*: n*-alkane indices for aquatic (P_{aq}) and terrestrial (P_{wax}) OM input of the UPL, TKL, DLB, SDLAG, LAG, and MAR profiles, with circles for unfrozen sediments, triangles for frozen sediments and a colour gradient over depth.

5.5.3. Carbon Preference Index - *n*-alkanes

The carbon preference index of short chain *n*-alkanes (CPI-alk-short) is with 5.26 highest in the uppermost sample of the DLB core (figure 5.9). The samples of the DLB core also show the widest range with a difference of 3.51 from the lowest to the highest value (figure 5.9). The lowest values for the CPI-alk-short were calculated for the deepest sample of the UPL core and the deepest as well as the middle part sample of the SDLAG core, varying between 1.43 and 1.4 (figure 5.9).

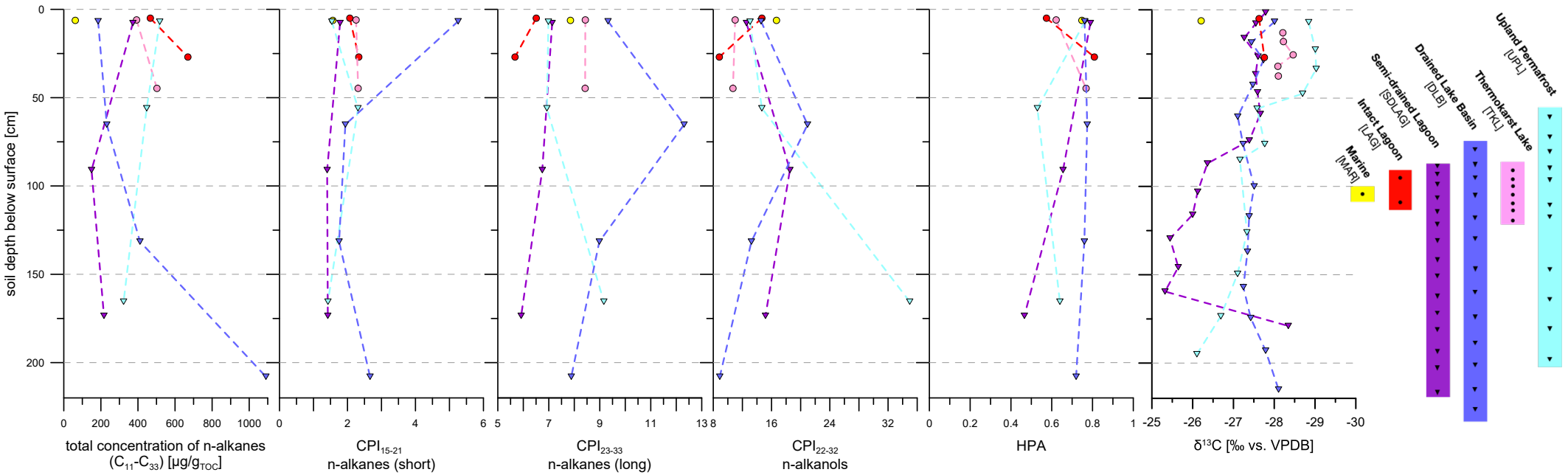

Figure 5.9: Summary of the biomarker indices and $\delta^{13}C$ ratios for the UPL, TKL, DLB, SDLAG, LAG, and MAR profiles, with circles for unfrozen sediments and triangles for frozen sediments. All diagrams (except for total concentration of n-alkanes) show more degraded samples on the left and less degraded samples on the right (descending x-axis of $\delta^{13}C$).

The long chain *n*-alkanes (CPI-alk-long) also shows the widest range in the samples of the DLB core, ranging between 7.88 in the deepest sample and the overall highest value of 12.31, calculated for the sample from a depth of 65.25 cm b.s.l. (figure 5.9). The lowest CPI-alk-long values has the LAG core in both samples with 5.67 in the deeper sample at 27 cm b.s.l. and 6.51 in the upper sample (figure 5.9).

5.5.4. Carbon Preference Index – *n*-alkanols

The pattern of the CPI of the *n*-alkanols (CPI-alc) follows for all cores the same general pattern as the CPI-alk-long (figure 5.9). The highest value of the samples in the uppermost 10 cm of the cores has the MAR sample with 16.68, but the highest value overall was calculated for the deepest UPL sample with 34.97 (figure 5.9). The lowest CPI-alc of 8.83 was calculated in the LAG sample from a depth of 27 cm b.s.l. and the deepest DLB sample with 8.89 (figure 5.9).

5.5.5. Higher Plant Index

The higher plant index (HPA) varies between 0.46 in the deepest SDLAG sample, and 0.81 in the deeper LAG sample (figure 5.9). The samples of the DLB, having wide ranges for the other indices, are all close together for the HPA, ranging between 0.72 and 0.77 (figure 5.9). The patterns of UPL, DLB and SDLAG are like the pattern of the CPI-alk-long (figure 5.9). The patterns of TKL and LAG in comparison are reversed, with an increasing value from the deeper sample to the uppermost one (figure 5.9).

5.6. Statistics

5.6.1. Correlation Matrix

Figure 5.10 shows two correlation matrices. The left one includes sedimentological as well as biogeochemical data, while the right one includes the biomarker indices, as well as the biogeochemical parameters mercury and $\delta^{13}C$, since these two are the only parameters correlating with the biomarker indices.

Parameters with strong positive correlations (> 0.5) are TN and TOC, TN and TOC_{vol}, TOC and TOC/TN ratio, CPI-alc and $\delta^{13}C$, CPI-alc and mercury, and P_{wax} and ACL (figure 5.10). Strong negative correlation (< -0.5) were found between absolute water content and dry bulk density, mercury, and mean grain size, CPI-alc and mercury, P_{aq} and ACL, and P_{wax} and P_{aq} (figure 5.10).

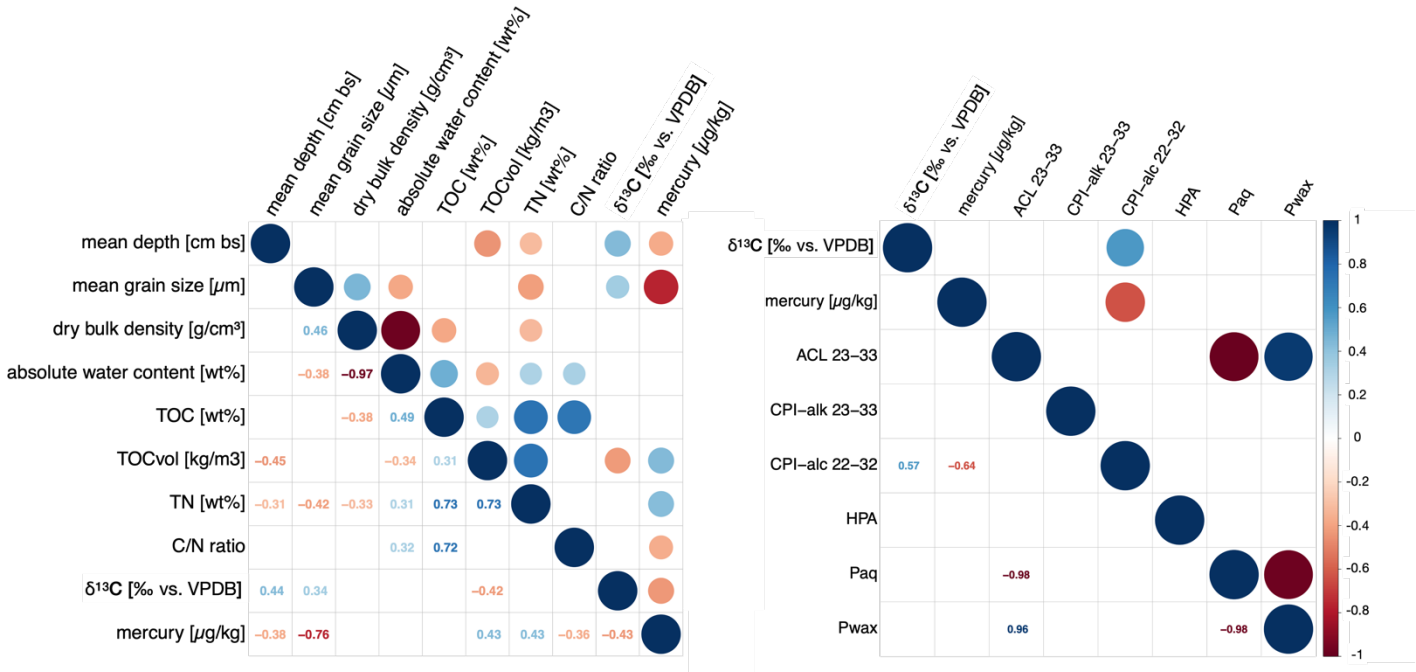

Figure 5.10: Correlation matrices of the sedimentological and biogeochemical parameters (left) and the biomarker indices with $\delta^{13}C$ and mercury (right). Strong positive correlations in dark blue, strong negative correlations in dark red.

5.6.2. Cluster Analysis

The results of the cluster analysis are shown in figure 5.11.

The first cluster (red) includes the two peat samples of the DLB core, and the sample from a mean depth of 56 cm b.s.l. of the UPL core, which is also from an organic band (figure 5.11).

The second cluster (green) includes almost all samples from the surface layers of the soils down to 45-60.5 cm b.s.l from the cores except for the marine core. Also, the deepest samples of SDLAG (179 cm b.s.l.) and DLB (215 cm b.s.l.) are included in the green cluster (figure 5.11).

The third cluster (blue) comprises the MAR sample and the samples of SDLAG from a mean depth between 74 and 159.5 cm b.s.l. (figure 5.11).

The fourth group (purple) is composed of the deeper samples of the UPL core (195-76 cm b.s.l.) and the deeper samples of the DLB core (193-76 cm b.s.l.) (figure 5.11). Moreover, the SDLAG sample from a mean depth of 7.75 cm b.s.l. and the DLB sample from a mean depth of 42.5 cm b.s.l. are assigned to this group (figure 5.11).

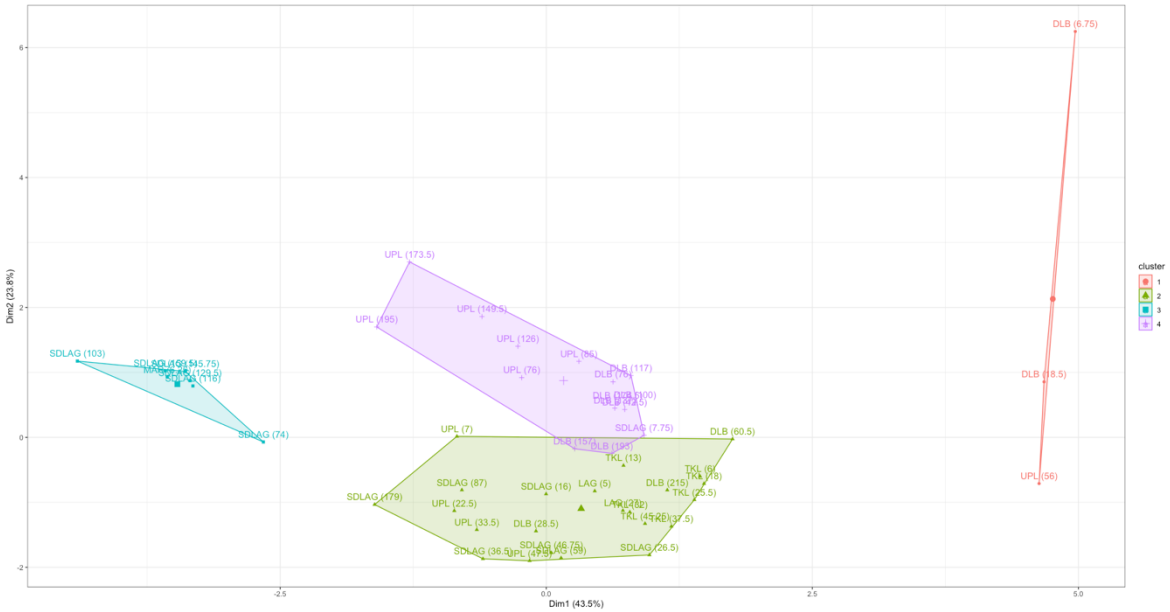

Figure 5.11: Display of the cluster analysis with four means.

5.6.3. Central Tendency Analysis

For the first analysis the nonparametric Kruskal-Wallis-Test was used to assess the presence of statistically significant differences in central tendencies among the data from four of the sample sites: SDLAG, DLB, TKL and UPL. The results reveal significant distinctions for all parameters ($p < 0.05$), except for the TOC density, were the observed p-value is 0.0822 (figure 5.12).

Through the subsequent pairwise comparisons of the four sediment cores, carried out using the Mann-Whitney-Wilcoxon test, it is possibly to see more precisely where the significant differences lie. The results show that specifically the SDLAG and TKL deposits, as well as the TKL and UPL deposits, have the most differences. In both of these pairs, significant differences are evident in four out of the six tested parameters (figure 5.12). Conversely, the SDLAG and UPL cores are the most similar, as evidenced by the absence of statistically significant differences in all measured biogeochemical parameters (figure 5.12). Additionally, a relatively high degree of similarities is shown between the SDLAG and the DLB samples, with significant differences only in the TOC content (figure 5.12).

To statistically verify possible differences between the saltwater influenced cores (MAR, LAG, SDLAG) and the cores that are not influenced by salt water (DLB, TKL, UPL), as well as differences between the frozen (SDLAG, DLB, UPL) and the unfrozen sites (MAR, LAG, TKL), also the non-parametric Mann-Whitney-Wilcoxon test was used.

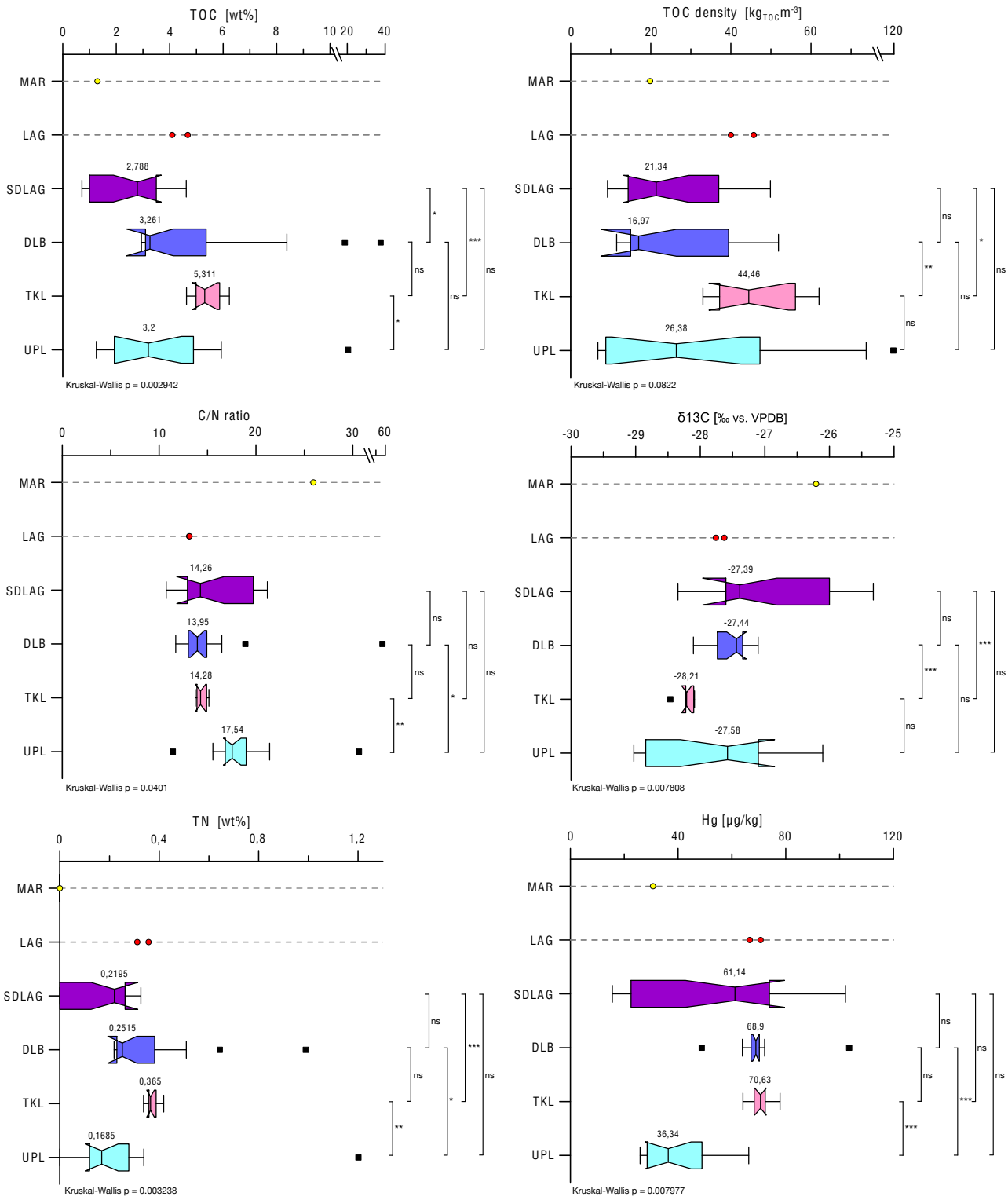

Figure 5.12: Boxplots of the biogeochemical parameters of the SDLAG, DLB, TKL, and UPL profile. (MAR and LAG as individual samples). The whiskers display the data range (outliers as black points) and the boxes show the interquartile range (25-75 %). The black vertical line marks the median and the notches represent the 95 % confidence interval. The bars left of the boxes show the statistical significance of differences between the profiles (ns for not significant, * for $p < 0.05$, ** for $p < 0.01$, and *** for $p < 0.001$).

Between the saltwater influenced deposits and the deposits not influenced by saltwater a statistically significant differences were calculated within the biogeochemical parameters for TOC ($p = 0.005452$) and TN ($p = 0.01832$) with the saltwater influenced sites having lower contents (mean TOC = 2.53 wt%; mean TN = 0.18 wt%) than the sites not influenced by saltwater (mean TOC = 6.04 wt%; mean TN = 0.33 wt%), and the $\delta^{13}C$ ratio ($p = 0.02019$), being significantly lower in the deposits not influenced by saltwater (mean $\delta^{13}C$ = -27.76 ‰ vs. VPDB) than in the saltwater influenced deposits (mean $\delta^{13}C$ = -26.96 ‰ vs. VPDB) (figure 5.13).

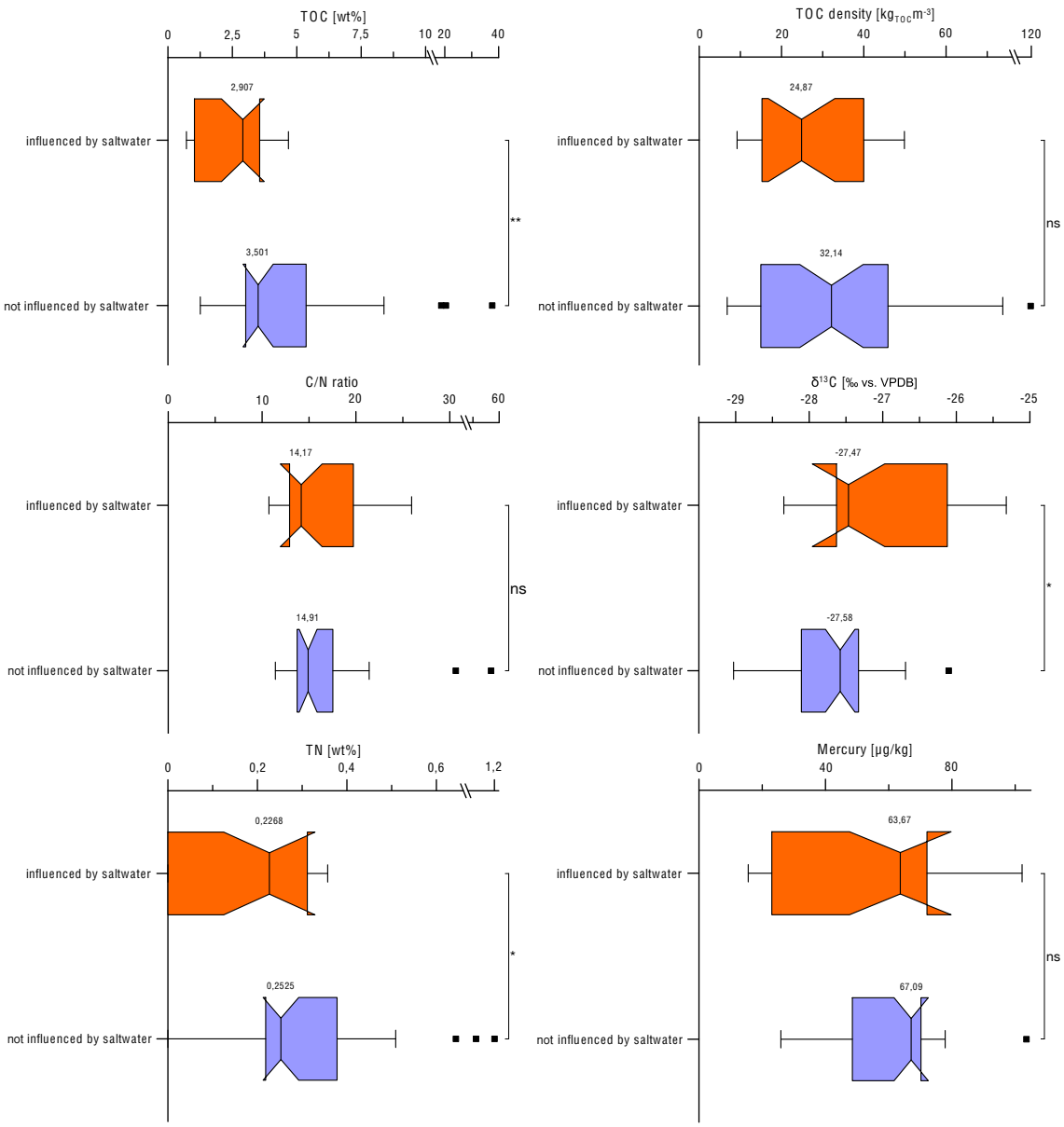

Figure 5.13: Boxplots of the biogeochemical parameters of profiles influenced by saltwater (orange) and profiles not influenced by saltwater (blue). The whiskers display the data range (outliers as black points) and the boxes show the interquartile range (25-75 %). The black vertical line marks the median and the notches represent the 95 % confidence interval. The bars left of the boxes show the statistical significance of differences between the groups (ns for not significant, * for $p < 0.05$, ** for $p < 0.01$, and *** for $p < 0.001$).

There is no significant difference of the central tendency between the two groups for TOC density, Mercury, and the TOC/TN ratio ($p > 0.05$) (figure 5.13). The biomarker indices for which the groups are statistically significantly different from each other are ACL-long ($p = 0.018$), CPI-alk ($p = 0.005$), and P_{wax} ($p = 0.008$), with all indices being lower in the saltwater influenced profiles.

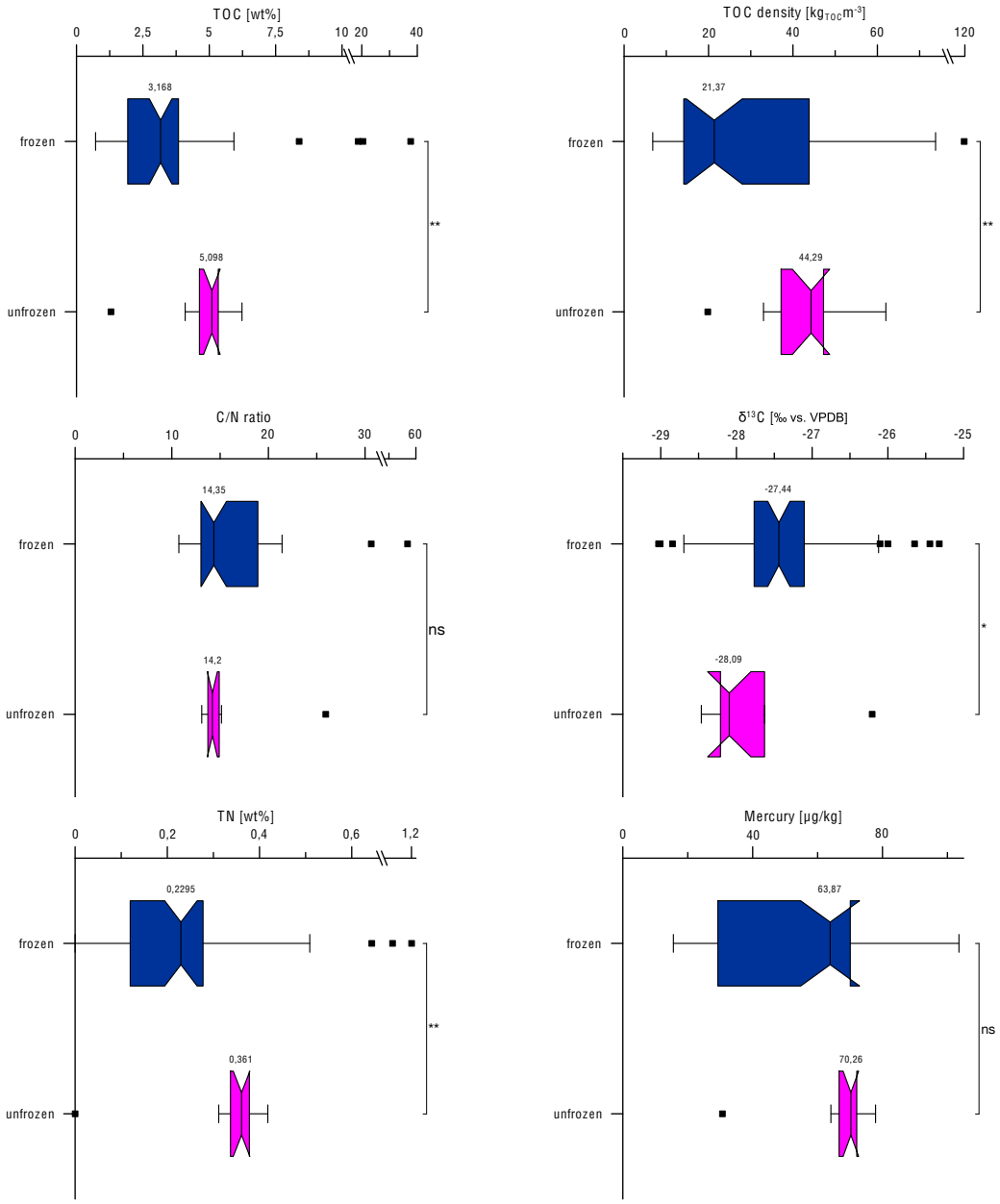

Figure 5.14: Boxplots of the biogeochemical parameters of frozen profiles (dark blue) and unfrozen profiles (pink). The whiskers display the data range (outliers as black points) and the boxes show the interquartile range (25-75 %). The black vertical line marks the median and the notches represent the 95 % confidence interval. The bars left of the boxes show the statistical significance of differences between the groups (ns for not significant, * for $p < 0.05$, ** for $p < 0.01$, and *** for $p < 0.001$).

The unfrozen and frozen cores have statistically significant differences in the TOC content ($p = 0.008$), the TOC_{vol} ($p = 0.01$), and the TN content ($p= 0.005$), with the frozen cores

having significantly lower concentrations (mean TOC = 4.75 wt%; mean TN = 0.26 wt%; mean TOC_{vol} = 28.83 kg_{TOC}/m^3) than the unfrozen cores (mean TOC = 4.76 wt%; mean TN = 0.33 wt%; mean TOC_{vol} = 42.97 kg_{TOC}/m^3), and in the $\delta^{13}C$ ratio (p-value = 0.01), being lower in the unfrozen cores (mean $\delta^{13}C$ = -27.9 ‰ vs. VPDB) than in the frozen ones (mean $\delta^{13}C$ = -27.35 ‰ vs. VPDB) (figure 5.14).

Biomarker indices show significant differences between the frozen and unfrozen cores for the ACL-long (p-value = 0.008), the P_{aq} (p-value = 0.04), and the P_{wax} (p-value = 0.028), with the ACL-long and P_{wax} being lower and the P_{aq} being higher in the unfrozen profiles than in the frozen ones.

6. Discussion

In the subsequent chapters, differences between the six analysed landforms are discussed, with a focus on their carbon pools, categorized into organic carbon storage (6.1), organic carbon source (6.2), and organic carbon degradation (6.3), as well as their depositional processes (6.4), and their Mercury content (6.5). Special attention is directed towards differences between the sites influenced by saltwater (SDLAG, LAG, MAR) and those unaffected by saltwater (UPL, TKL, DLB), as well as differences between the frozen (UPL, DLB, SDLAG) and unfrozen (TKL, LAG, MAR) deposits.

6.1. Organic Carbon Storage

The organic carbon storage is discussed on the basis of the measured TOC content [wt%] across the different sites and depths, and the calculated TOC volume [$kg_{TOC}m^{-3}$] stored in the soils at the sites, addressing the first research question how much organic carbon the different landscape units store in comparison to one another.

As expected, the total range of TOC contents in the samples is relatively wide (0.72-37.62 wt%) compared to other studies (0.2-24 wt%; Strauss et al., 2015). This was probably due to the diverse initial material from the different features of the permafrost/ thermokarst landscape, as well as the inclusion of more landscape units from the land to marine realm. Within one core the deposits from the DLB show the largest range of the TOC content (2.94-37.62 wt%). This might be due to the mixed permafrost and thermokarst lake features of the core. Also, the post-thermokarst-lake peat accumulation influences especially the high TOC contents in the upper soil of the DLB (Jongejans et al., 2020; Lenz et al., 2016). The large, often flat-bottomed DLBs provide perfect conditions for the formation of wetlands, through which most DLBs become vegetated in 5-10 years after the drainage event and accumulate peat 10-20 years after (Jones et al., 2012).

In both freshwater-influenced thermokarst deposits (DLB and TKL) the measured TOC content is significantly higher than in the SDLAG profile, and in case of the TKL deposits also higher than in the UPL profile. Although the highest mean TOC content was measured in the deposits of the DLB (mean 7.57 wt%), it should not be over interpreted, since the median TOC content of the DLB core is with 3.26 wt% much lower than the mean value. This high mean is strongly influenced by the high TOC contents of the narrow peat layer in the upper centimetres of the core. As already mentioned, it is common that DLB sediment recover quickly after drainage, initializing post-lake peat growth, which sequesters carbon from the atmosphere and increases the carbon content in the basin sediments (Schirrmeister et al., 2011a; Strauss et al., 2015). The TOC content measured in this study is nevertheless comparable to other studies. For example, Fuchs et al. (2019) distinguished between a mean for the upper 100 cm of a DLB core, which was 16 wt% and is 11.08 wt% in the present study, and a mean for samples between 100 and 200 cm b.s.l., which was 3.5 wt% and is 3.48 wt% in the present study. In addition, the TKL profile shows high TOC contents (mean 5.37 wt%). It is a little lower than literature values of 6.5 wt% (Strauss et al., 2013), 5.6 wt% (Fuchs et al., 2019), and 7.0 wt% (Lenz et al., 2016), but significantly higher than the TOC content in the SDLAG and UPL profiles measured in this study. This is likely due to a high input of Holocene organic Carbon (OC), primary productivity in the lake stimulated by nutrient release of thawing permafrost and accumulation of organic matter (OM), further accelerated by slow decomposition due to a cold and anaerobic lake environment (Strauss et al., 2015). The measured TOC content of the UPL permafrost deposits is with a mean of 4.66 wt% a little higher compared TOC contents from previous permafrost studies with 3.0 wt% (Strauss et al. 2013) and 2.4 wt% (Strauss et al. 2015), but much lower than the mean TOC content in permafrost of 29 wt% measured by Fuchs et al. (2019) in the Teshekpuk lake region. The lowest mean TOC content (2.37 wt%), measured in the SDLAG deposits, might be influenced by a decrease of the primary productivity with the transition from the thermokarst lake to the lagoon, due to the strong seasonal fluctuations of the salt content, the lowered, fluctuating water level to almost drainage, and the bedfast ice formation in winter, which shortens the period of biological production. Therefore, it could be expected that there is less primary productivity in the SDLAG compared to the TKL and the DLB. Decomposition processes probably take place in soil of SDLAG only in summer, since at least in the year of sampling there was no talik underlying the bedfast ice of the SDLAG. There might was decomposition all year round when the lagoon had more water or rather was in the state of a thermokarst lake, which also could have led to a decreased TOC content. This probably also be a cause for the significantly lower TOC contents in the profiles of the saltwater influenced sites (mean 2.53

wt%) than in the profiles of the sites not influenced by saltwater (mean 6.04 wt%). In case of the marine sample also the coarser grain size and the different deposition processes might influence the low TOC content. Moreover, there is a significant difference between the frozen and unfrozen sites, with unfrozen sites having significantly higher TOC contents (mean 4.76, median 5.1) than the frozen sites (mean 4.75, median 3.17). This difference, as well as the difference between the TKL and UPL, indicate a higher primary productivity and OM accumulation in the unfrozen deposits in contrast to the frozen sites, in despite of a probably accelerated degradation of OM in the unfrozen deposits.

The organic carbon storage in the soils at the different sites was calculated as the TOC_{vol} [$kg_{TOC}m^{-3}$]. In contrast to other studies the mean TOC_{vol} of the UPL deposits is with 36.66 $kg_{TOC}m^{-3}$ relatively high. Strauss et al. (2013 & 2015) found that the TOC_{vol} in thermokarst is with means of 33 $kg_{TOC}m^{-3}$ (2013) and 24 $kg_{TOC}m^{-3}$ (2015) higher than in the UPL deposits with means of 19 $kg_{TOC}m^{-3}$ (2013) and 14 $kg_{TOC}m^{-3}$ (2015). Fuchs et al. (2019) found higher TOC_{vol} in UPL than in thermokarst deposits. In this study the unfrozen sites have significantly higher mean TOC_{vol} (42.97 $kg_{TOC}m^{-3}$) than the frozen sites (28.83 $kg_{TOC}m^{-3}$). Moreover, the mean TOC_{vol} in the deposits of the TKL (46.31 $kg_{TOC}m^{-3}$) is significantly higher than the two lowest mean TOC_{vol} in the deposits of the SDLAG (26.36 $kg_{TOC}m^{-3}$) and the DLB (25.06 $kg_{TOC}m^{-3}$). Since the TKL deposits also have a high TOC content, the TOC_{vol} is likely influenced by the input of TOC due to primary production in the lake, and relocation of OM e.g., due to erosion, leading to OC accumulation in the basin, but also by thaw subsidence progression due to ground ice loss (Lenz et al., 2016; Strauss et al., 2015). The low TOC_{vol} in the refrozen thermokarst features in comparison might be influenced by ground ice accumulation after the drainage of the water bodies and in case of the SDLAG deposits also by a low primary productivity.

To answer the question if the different landforms of a thermokarst landscape are whether a sink of carbon or a source of greenhouse gas emissions, it is important to also look at the source of the OM, as well as at the level of degradation.

6.2. Organic Carbon Source

To assess the degradability of OC stored in the soils it is of great interests where the OM in the soils comes from. Therefore, the following chapter answers the second research question of the potential sources of the OC and the differences across the landscape units, based on the TOC/TN ratio, the stable carbon isotopes, and the biomarker distributions.

A low TOC/TN ratio can indicate an aquatic influence, from algae and bacteria on the OM decomposition in soils (Meyers, 1997). This is might the case for the TKL deposits with the

lowest mean TOC/TN ratio of 14.39. In combination with the low mean $\delta^{13}C$ ratio of -28.22 ‰ vs. VPDB it is likely that the aquatic OM in the TKL deposits is of lacustrine origin (Meyers, 1997). In contrast the highest mean TOC/TN ratio (18.45) was measured in the UPL samples, indicating a stronger terrestrial influence on the OM composition. The largest variation of the TOC/TN ratio within the interquartile range show the SDLAG samples, indicating different sources of OM during the different stages of the thermokarst lagoon transition. It is also shown in figure 5.8 that the OM in samples of the SDLAG have a fluctuating aquatic and terrestrial influence over depth. The largest variation between all samples was measured in the deposits of the DLB, which also indicates different sources of the OM in the different stages of the thermokarst lake evolution, also shown in the fluctuating P_{wax} and P_{aq} over depth (figure 5.8). Since the TOC/TN and the $\delta^{13}C$ ratio are also parameters for the degradation of OM, these variations can also result from different degrees of degradation of the OM with depth, a topic further discussed in the following chapter.

The biomarker analysis shows that the samples of the UPL core have the strongest terrestrial influence, indicated by the highest ACL-long values and a high P_{wax} in all three samples. The strongest aquatic influence was detected in the OM of the marine sample, with the lowest ACL-long and a high P_{aq}. It is also shown in figure 5.7 and 5.8 that all thermokarst deposits are stronger influenced by aquatic OM than the UPL samples, since all samples have lower ACL-long and P_{wax} values. Moreover, both figures show that there is a change of source in the SDLAG, DLB and UPL profiles from the upper soil compared to the samples between 50 and 100 cm b.s.l. and between 100 and 200 cm b.s.l. (figure 5.7 & 5.8). Starting with low ACL-long values and thus a stronger aquatic influence in the upper soil. The ACL-long is higher, accompanied by higher P_{wax} and lower P_{aq}, between 50 and 100 cm b.s.l., indicating a more terrestrial influence, and again lower between 100 and 200 cm b.s.l., accompanied by higher P_{aq} and lower P_{wax} values indicating a stronger aquatic influence. This course could be due to more than one thermokarst lake generation at the SDLAG and DLB site, but since it is also shown in the UPL deposits it might indicate changed hydrological conditions at the time of deposition or is influenced by relocation of OM, for example due to cryoturbation or roots.

Significant differences were determined in the ACL-long and the P_{wax} between the saltwater influenced cores (mean ACL-long: 26.6; mean P_{wax}: 0.57) and those that are not influenced by saltwater (mean ACL-long: 27.31; mean P_{wax}: 0.68), as well as between the unfrozen (mean ACL-long: 26.52; mean P_{wax}: 0.57) and the frozen (mean ACL-long: 27.27; mean P_{wax}: 0.67) cores. Those differences in the *n*-alkane distribution can also be seen in figure 6.1. All unfrozen cores and the uppermost sample of the SDLAG, tend to have more of a

double peak in the *n*-alkane distribution at *n*-C_{23} and *n*-C_{27}, indicating a dominating input of bryophytes (*n*-C_{23}) and leaf waxes (*n*-C_{27}) (Haugk et al., 2021; Zech et al., 2009). In contrast the UPL, DLB and deeper SDLAG samples tend to have a peak at *n*-C_{27} and in case of the UPL samples a double peak at *n*-C_{27} and *n*-C_{31}, indicating a dominating input of leaf waxes (*n*-C_{27}) and grasses (*n*-C_{31}) (Haugk et al., 2021; Zech et al., 2009). The indication that there is a stronger tendency to an aquatic influence on the OM composition in the deposits under waterbodies (unfrozen) is also supported by the significant difference in the P_{aq} between unfrozen (mean 0.61) and the frozen (mean 0.47) sites.

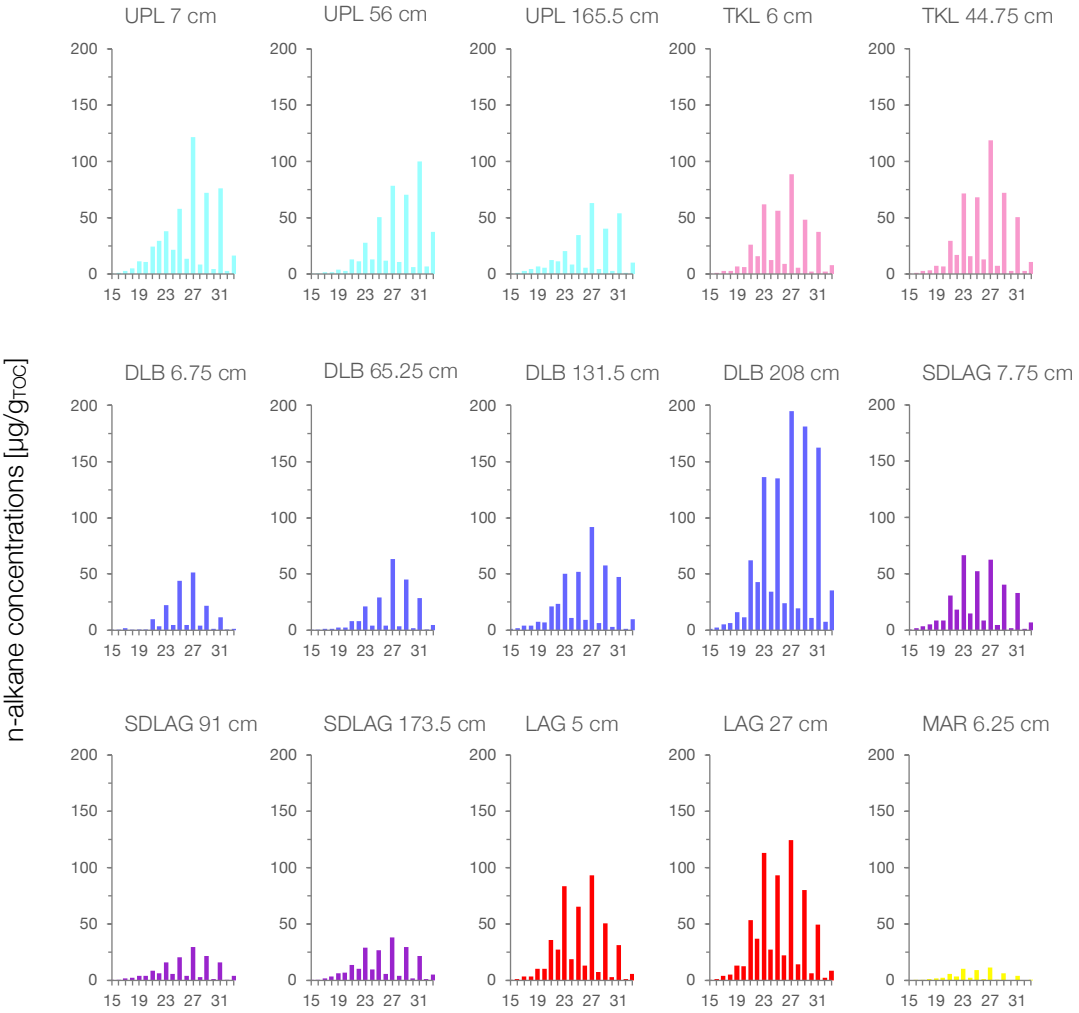

Figure 6.1: *n*-alkane distributions of UPL (ice blue), TKL (pink), DLB (electric blue), SDLAG (purple), LAG (red), and MAR (yellow).

In summary the data discussed in this chapter shows that there are different sources of OM in the different deposits, with parameters such as salinity, temperature, and water availability likely to influence the composition of the accumulated OM.

6.3. Organic Carbon Degradation

On the basis of the TOC/TN and the $\delta^{13}C$ ratios, as well as the biomarker indices CPI-alk-long, CPI-alk-short, CPI-alc, and HPA the level of degradation of the OM stored in the soils is discussed in the following chapter, answering the third research question about the quality of organic carbon in the deposits and the distinctions in the level of degradation across the landscape units.

Since decomposition releases Carbon from the soils to the atmosphere and Nitrogen to the soils, deposits containing further degraded OM have lower TOC/TN ratios than those containing fresh OM (Andersson et al., 2012; Weintraub & Schimel, 2005). Significant differences of the TOC/TN ratio were determined between the TKL and UPL, and the DLB and UPL profiles, with the UPL samples having significantly higher TOC/TN ratios than the thermokarst deposits. Additionally, the LAG samples, not included in the statistical analysis due to the small sample size, show very low TOC/TN ratios. It is therefore likely that the thermokarst deposits contain stronger degraded OM than the UPL profile. The mean TOC/TN ratio of the UPL (18.45) is in the lower range of the ratios measured by Routh et al. (2014) in Arctic peat soils (15-25) and a little lower than the mean TOC/TN measured by Fuchs et al. (2019) in upland permafrost samples in the Teshekpuk region (21.3). However, they are higher than the mean TOC/TN ratio measured by Haugk et al. (2021) in Siberia (13.24). The mean TOC/TN ratios in the TKL (14.39) and the DLB (17.5) profiles are slightly higher than those measured by Fuchs et al. (2019) with a mean TOC/TN ratio in the upper 100 cm of the soils of 12.6 in TKL deposits and 16.6 of DLB deposits. The rather high values of all profiles indicate a high preservation and good quality of the accumulated OM and therefore a vulnerability to decomposition after thaw.

$\delta^{13}C$ values show in theory the best-preserved OM in the TKL samples and the most degradation in SDLAG samples. Since the biomarker indices referring to the source of OM, like the ACL-long with a range between 26.2 and 28.37, indicates different sources of OM between the sites, the variation of $\delta^{13}C$ should be rather interpreted as a signal for origin than a proxy for degradation of the OM.

The CPI, both CPI-alk-long and CPI-alk-short, show higher values in the DLB and TKL deposits, compared to the UPL samples (figure 5.9). In contrast to the TOC/TN ratio this indicates stronger degraded OM in the UPL profile. The CPI-alk-long as well as the CPI-alc of the UPL deposits is low in the upper samples and increasing to 9.16 (CPI-alk-long) and 34.97 (CPI-alc) in the deepest sample. This implies fewer degraded OM in the deeper layers and ongoing degradation in the upper soil. With ongoing climate warming and thawing of the deeper permafrost layers the preserved OM of good quality could become

available to decomposition, leading to increased emissions of greenhouse gases. The saltwater influenced profiles have significantly lower CPI-alk-long (mean 6.64), than the profiles not influenced by saltwater (mean 8.71), indicating more degradation in the SDLAG, LAG, and MAR deposits, than in the DLB, UPL, and TKL deposits.

Although the mean TOC/TN ratios of the different sites indicate that OM in the UPL deposits is less degraded than in the thermokarst features, the CPI-alk suggests a higher level of degradation in the UPL samples compared to DLB and TKL. Furthermore, both HPA and CPI-alc reveal less degraded OM in the DLB core than in the UPL deposits, at least in the uppermost samples. This could indicate an increased input and accumulation of Holocene OC, past or present, to the thermokarst deposits, balancing out the increased degradation of OM in thawed sediments. When interpreting these parameters, it is important to keep in mind that they represent composite signals also influenced by other properties of the OM, such as its composition.

6.4. Depositional Processes

The grainsize distribution (g.s.d.) of the sediments and its shifts over the depth of a core can indicate different stages of the thermokarst development at the sampling sites. The following chapter discusses the fourth research question about the predominant depositional processes that characterize the different landscape features, and where similarities and differences in these processes exist.

The g.s.d. of the UPL deposits is dominated by a peak in the area of fine sands and silts, indicating fluvial deposition processes (Strauss et al., 2012). There are two shifts in the core towards finer grained deposits (150-130 cm b.s.l., 75-55 cm b.s.l). Since the surface structure of the area is dominated by a polygonal tundra, the shift in the grain size distribution in the profile might be due to a shift of the polygon at the time, for example due to a lift or lowering of the polygon rim or a spread of the polygon. Also changed hydrological conditions, like a change in the water level, could have caused those shifts.

The thermokarst soils all have lacustrine deposits, with a peak in the grainsize distribution between silt and clay. This fine mean grainsize indicates aeolian and low velocity fluvial deposition (Strauss et al., 2012). In case of the short cores of the LAG and TKL, but also in case of the DLB they determine the g.s.d. over the entire length of the core. The SDLAG core in contrast shows a shift from coarser material in the deeper layers to finer material in the upper layers. In the deeper layers (180-100 cm b.s.l.) the grain size has a peak, similar to the UPL deposits, between fine sand and silt, indicating that those are the initial permafrost deposits, not influenced by the thermokarst. Above (100-0 cm b.s.l.), lacustrine

sediments are found, showing a similar peak in the g.s.d. as the TKL, LAG and DLB, most likely deposited during the thermokarst lake and lagoon state of the site. The mussels that were found throughout the whole length of the core are most likely no recent deposits, but part of the marine sediments in the region, attributed to a series of marine transgressions (Farquharson et al., 2018; Rawlinson, 1990).

6.5. Mercury Content

Since permafrost soils have the potential to accumulate mercury bound in OM over centuries, the differences of the mercury content in the different landscape units are discussed in the following chapter, addressing the fifth research question, as well as the sixth research question if there is a correlation between permafrost degradation and the accumulation of mercury in the soil profiles.

The mercury content analysis of the different cores of this study shows that the thermokarst deposits have higher Hg concentrations compared to the UPL deposits. Significant differences in the Hg content were observed between the DLB and UPL, as well as between the TKL and UPL deposits. The median Hg content of the TKL samples (70.63 µg/kg) is nearly twice as high as the median of the UPL samples (36.34 µg/kg). Furthermore, the Hg levels of the two samples of the LAG core are consistent with the TKL samples. The SDLAG profile has no significant differences to the other cores and shows the largest variations in the Hg content across the samples. As for the findings of the g.s.d. the mercury content in the deeper layers of the SDLAG (180-100 cm b.s.l.) is akin to the content found in UPL samples and is thus relatively low (15.57-48.65 µg/kg). In contrast, the upper layers (100-0 cm b.s.l.) have much higher Hg concentrations, which are quite similar to the concentrations in the other thermokarst samples (20.27-102.17 µg/kg).

All cores show a higher mean Hg content than measured in deeper deposits by Rutkowski et al. (2021) in Siberia (mean 9.72 µg/kg). The median Hg content measured for upland permafrost samples from the North Slope, Alaska by Schuster et al. (2018) of 43 µg/kg, is slightly higher than in the UPL samples of this study, with a median of 36.34 µg/kg.

Sources of the Hg accumulated in Arctic soils can be both, natural and anthropogenic. Natural sources contributing increased atmospheric Hg and subsequent deposition into soils include boreal forest fires and volcanic activity (Schuster et al., 2018). Anthropogenic input has significantly intensified due to industrialization and expanding anthropogenic land use (Jonsson et al., 2017). Obrist et al. (2017) found that approximately 70 % of the Hg in the Arctic tundra derived from gaseous elemental Hg, which is ubiquitously present in the atmosphere, and only minor contribution of deposition via precipitation or atmospheric

mercury depletion events. This is important, since the deposition of the gaseous elemental Hg is strongly influenced by the uptake of vegetation (Obrist et al., 2017). Sites with a higher primary productivity, which accumulate OM in the soils, also potentially accumulate higher levels of Hg bond in the vegetation. Furthermore, thawing permafrost affects the distribution and accumulation of Hg in specific deposits. Previously freeze-looked Hg-containing OM in the soil releases Hg upon decomposition (Schuster et al., 2018). Thermokarst erosion and increased soil water movement, triggered by permafrost thaw, increase the transport of Hg from the soils to Arctic surface water, resulting in higher Hg concentrations in lake- and post-lake sediments, which is also indicated by the data of this study (Rydberg et al., 2010).

7. Conclusion

In this study sediment cores from six different landscape features of a dynamic coastal thermokarst landscape were analysed: upland permafrost, a thermokarst lake, a drained thermokarst lake basin, a semi-drained lagoon, an intact lagoon, and marine deposits. The findings have shown the complex interplay of environmental factors, landform characteristics, and impacts of climate change on these Arctic landscapes.

Concerning the first objective of my master thesis, the **quantification and characterization of organic carbon**, and particularly the first addressed question regarding the **quantity** of organic carbon, I found strong variations in the TOC content within and across the different landforms, with the DLB profile showing the broadest range. This variation can be most likely attributed to the mixed source signals of initial permafrost and thermokarst lake features in the core. The DLB and the TKL profiles show the highest mean TOC contents, indicating a Holocene OC input and increased primary productivity in the freshwater influenced thermokarst features. This is supported by the analysis of the **quality** of organic carbon, which shows fresh undegraded organic matter in both profiles, indicated by high CPI-alk-long values. The SDLAG profile has significantly lower TOC contents than the TKL and DLB deposits and in addition, all saltwater influenced profiles show significantly lower TOC contents than those not influenced by saltwater. This could be attributed to a lower primary productivity and thus less input of organic matter, after the saltwater intrusion to the soils. This is also displayed by a significantly lower CPI-alk-long in the saltwater influenced profiles compared to those not influenced by saltwater, indicating more degraded organic matter. Moreover, the unfrozen deposits have a significantly higher TOC_{vol} than the frozen profiles. The analysis of the carbon **sources** showed a varying degree of aquatic influence across the different landforms, displayed by significant difference in the source indicating biomarker indices between the saltwater

influenced profiles and those not influenced by saltwater, as well as across the unfrozen and frozen deposits. Moreover, the significantly higher TOC/TN ratio in the TKL and DLB profiles in contrast to the UPL profiles, indicates a stronger aquatic influence on the organic matter composition in the thermokarst features.

The second aim, the **sedimentological and depositional characterization** of the profiles and the raised question of the **dominant depositional processes** and the **differences** across the landscape units, can be conclusively answered as followed: The analysis of the grain size distribution showed different characteristics across the different soil profiles, reflecting different stages of thermokarst development. The coarser grain size in UPL deposits is indicative for fluvial deposition, while the thermokarst deposits are dominated by finer grained lacustrine deposits, indicating aeolian and low-velocity fluvial deposition. The SDLAG profile clearly shows a shift from initial permafrost deposits in the deeper layers and lacustrine deposits in the upper layers.

Concerning my last objective, the **quantification of mercury** and the differences between the soil profiles, I found higher **mercury contents** in the thermokarst deposits than in the UPL profile, with the TKL profile having a median mercury content (70.63 µg/kg) almost twice as high as in the UPL deposits (36.34 µg/kg). Regarding the **correlation** of permafrost degradation and the accumulation of mercury, I found that it is likely that sediments with a higher input of OM have higher accumulation rates of mercury. Moreover, the thawing of permafrost and the associated processes potentially lead to an accumulation of mercury in lake environments.

In summary, this study contributes valuable data to our understanding of the dynamics within a changing coastal thermokarst landscape. With ongoing climate change and anticipated permafrost thaw in the future, Arctic environments will continue to change, including the expansion of thermokarst landscapes. It is therefore crucial to further investigate and monitor changes of the characteristic and processes of different landscape units, associated with those landscape changes, to predict future impacts and the development of adaptation and mitigation strategies.

8. References

Alam, S. I., Hammoda, H., Khan, F., Al Enazi, R., Goktepe, I. (2020): Electrical Conductivity, pH, Organic Matter and Texture of Selected Soils around the Qatar University campus. *Agriculture, Livestock and Fisheries*, vol. 7, (3), pp. 403- 409, Doi: 10.3329/ralf.v7i3.51359.

Andersson, R. A., Meyers, P., Hornibrook, E., Kur, P., Mörth, C. (2012): Elemental and isotopic carbon and nitrogen records of organic matter accumulation in a Holocene permafrost peat sequence in the East European Russian Arctic. *Journal of Quaternary Science*, vol. 27, (6), pp. 545-552, Doi: 10.1002/jqs.2541.

Angelopoulos, M., Overduin, P., Jenrich, M., Nitze, I., Günther, F., Strauss, J., Westermann, S., Schirrmeister, L., Kholodov, A., Krautblatter, M., Grigoriev, M. N., Grosse, G. (2021): Onshore Thermokarst Primes Subsea Permafrost Degradation. *Geophysical Research Letters*, vol. 48, (20), Doi: 10.1029/2021GL093881.

Arp, C. D., Jones, B. M., Urban, F. E., Grosse, G. (2011): Hydrogeomorphic processes of thermokarst lakes with grounded-ice and floating-ice regimes on the Arctic coastal plain, Alaska. *Hydrological Processes*, vol. 25, (15), pp. 2422-2438, Doi: 10.1002/hyp.8019.

Blott, S. J. & Pye, K. (2001): GRADISTAT: A grain size distribution and statistics package for the analysis of unconsolidated sediments. Earth *Surface Processes and Landforms*, vol. 26, (11), pp. 1237-1248, Doi: 10.1002/esp.261.

Bray, E. E. & Evans, E. D. (1961): Distribution of *n*-paraffins as a clue to recognition of source beds. *Geochimica et Cosmochimica Acta*, vol. 22, (1), pp. 2-15, Doi: 10.1016/0016-7037(61)90069-2.

Cohen. J., Zhang, X., Francis, J., Jung, T., Kwok, R., Overland, J., Ballinger, T. J., Bhatt, U. S., Chen, H. W., Coumou, D., Feldstein, S., Gu, H., Handorf, D., Henderson, G., Ionita, M., Kretschmer, M., Laliberte, F., Lee, S., Linderholm, H. W., Maslowski, W., Peings, Y., Pfeiffer, K., Rigor, I., Semmler, T., Stroeve, J., Taylor, P. C., Vavrus, S., Vihma, T., Wang, S., Wendish, M., Wu, Y., Yoon, J. (2020): Divergent consensuses on Arctic amplification influence on midlatitude severe winter weather. *Nature Climate Change*, vol. 10, (1), pp. 20-29, Doi: 10.1038/s41558-019-0662-y.

Coulombe, S., Fortier, D., Bouchard, F., Paquette, M., Charbonneau, S., Lacelle, D., Laurion, I., Pienitz, R. (2022): Contrasted geomorphological and limnological properties of thermokarst lakes formed in buried glacier ice and ice-wedge polygon terrain. *The Cryosphere*, vol. 16, (7), pp. 2837-2857, Doi: 10.5194/tc-16-2837-2022.

Dixon J. C. (2013): Response of Periglacial Geomorphic Processes to Global Change. Shroder, J. [editor in Chief.], James, L. A., Harden, C. P., Claque, J. J. [eds.], *Treatise on Geomorphology*, Academic press, San Diego, CA, vol. 13, Geomorphology of Human Disturbances, Climate Change, and Natural Hazards, pp. 177-189, Doi: 10.1016/B978-0-12-374739-6.00351-1.

Farquharson, L., Mann, D., Rittenour, T., Groves, P., Grosse, G., Jones, B. (2018): Alaskan marine transgressions record out-of-phase Arctic Ocean glaciation during the last interglacial. The Geological Society of America, vol. 46, (9), pp. 783-786, Doi: 10.1130/G40345.1.

Ficken, K. J., Li, B., Swain, D. L., Eglinton, G. (2000): An n-alkane proxy for the sedimentary input of submerged/floating freshwater aquatic macrophytes. *Organic Geochemistry*, vol. 31, (7-8), pp. 745-749, Doi: 10.1016/S0146-6380(00)00081-4.

French, H. M. (2007): *The Periglacial Environment*. 3rd ed., John Wiley & Sons Ltd, West Sussex, England, Doi: 10.1002/9781118684931.

French, H. M. (2011): Periglacial Environments. *The SAGE Handbook of Geomorphology*, SAGA Publications Ltd, London, pp. 393-411, Doi: 10.4135/9781446201053.

Fuchs, M., Lenz, J., Jock, S., Nitze, I., Jones, B. M., Strauss, J., Günther, F., Grosse, G. (2019): Organic Carbon and Nitrogen Stocks Along a Thermokarst Lake Sequence in Arctic Alaska. *Journal of Geophysical Research: Biogeosciences*, vol. 124, (5), pp. 1230-1247, Doi: 10.1029/ 2018JG004591.

Gilichinsky, D., Rivkina, E., Bakermans, C., Shcherbakova, V., Petrovskaya, L., Ozerskaya, S., Ivanushkina, N., Kochkina, G., Laurinavichius, K., Pecheritsina, S., Fattakhova, R., Tiedje, J. M. (2005): Biodiversity of cryopegs in permafrost. *FEMS Microbiology Ecology*, vol. 53, (1), pp. 117-128, Doi: 10.1016/j.femsec.2005.02.003.

Grosse G., Jones, B., Arp, C. (2013): Thermokarst Lakes, Drainage, and Drained Basins. Shroder, J. [editor in Chief.], James, L. A., Harden, C. P., Claque, J. J. [eds.], *Treatise on Geomorphology*, Academic press, San Diego, CA, vol. 8, Glacial and Periglacial Geomorphology, pp. 325-353, Doi: 10.1016/B978-0-12-374739-6.00216-5.

Grosse, G., Romanovsky, V., Jorgenson, T., Walter Anthony, K., Brown, J., Overduin, P. P. (2011): Vulnerability and Feedbacks of Permafrost to Climate Change*. EOS, Transactions, American Geophysical Union*, vol. 92, (9), pp. 73-80, Doi: 10.1029/2011EO090001.

Harris, C. M., McClelland, J. W., Connelly, T. L., Crump, B. C., Dunton, K. H. (2017): Salinity and Temperature Regimes in Eastern Alaskan Beaufort Sea Lagoons in Relation to Source Water Contributions. *Estuaries and Coasts*, vol. 40, pp. 50-62, Doi: 10.1007/s12237-016-0123-z.

Harvey, A. (2019): Properties of Ice and Supercooled Water. *CRC Handbook of Chemistry and Physics*, CRC Press, Boca Raton, FL, [online] https://tsapps.nist.gov/publication/get_pdf.cfm?pub_id=926353, accessed 29.06.2023.

Haugk, C., Jongejans, L. L., Mangelsdorf, K., Fuch, M, Ogneva, O., Palmtag, J., Mollenhauer, G., Mann, P. J., Overduin, P. P., Grosse, G., Sanders, T., Tuerena, R. E., Schirrmeister, L., Wetterich, S., Kizyakov, A., Karger, C., Strauss, J. (2021): Organic matter characteristics of a rapidly eroding permafrost cliff in NE Siberia (Lena Delta, Laptev Sea region). *Biogeosciences - Discussions*, Doi: 10.5194/bg-2021-331.

Hinkel, K. M., Jones, B. M., Eisner, W. R., Cuomo, C. J., Beck, R. A., Frohn, R. (2007): Methods to assess natural and anthropogenic thaw lake drainage on the western Arctic coastal plain of northern Alaska. *Journal of Geophysical Research Atmospheres*, vol. 112, (F02S16), Doi: 10.1029/ 2006JF000584.

Hugelius, G., Strauss, J., Zubrzycki, S., Harden, J. W., Schuur, E. A. G., Ping, C. L., Schirrmeister, L., Grosse, G., Michaelson, G. J., Koven, C. D., O'Donell, J. A., Elberling, B., Mishra, U., Camill, P., Yu, Z., Palmtag, J., Kuhry, P. (2014): Estimated stocks of circumpolar permafrost carbon with quantified uncertainty ranges and identified data gaps. *Biogeosciences*, vol. 11, (23), pp. 6573-6593, Doi: 10.5194/bg-11-6573-2014.

Hughes, P. D. (2013): Quaternary-Pleistocene glacial and periglacial environments. Shroder, J. [editor in Chief.], James, L. A., Harden, C. P., Claque, J. J. [eds.], Tr*eatise on Geomorphology,* Academic press, San Diego, CA, vol. 8, Glacial and Periglacial Geomorphology, pp. 30–44, Doi: 10.1016/B978-0-12-374739-6.00192-5.

IPCC (2022): *Climate Change 2022: Impacts, Adaptation and Vulnerability. Contribution of Working Group II to the Sixth Assessment Report of the Intergovernmental Panel on Climate Change*. [Pörtner, H.-O., Roberts, D.C., Tignor, M., Poloczanska, E.S., Mintenbeck, K., Alegría, A., Craig, M., Langsdorf, S., Löschke, S., Möller, V., Okem, A., Rama, B. (eds.)]. Cambridge University Press. Cambridge University Press, Cambridge, UK and New York, NY, USA, 3056 pp., Doi:10.1017/9781009325844.

IPCC (2019*): IPCC Special Report on the Ocean and Cryosphere in a Changing Climate*. [Pörtner, H.-O., Roberts, D. C., Masson-Delmotte, V., Zhai, P., Tignor, M., Poloczanska, E., Mintenbeck, K., Alegría, A., Nicolai, M., Okem, A., Petzold, J., Rama, B., Weyer, N. M. (eds.)]. Cambridge University Press, Cambridge, UK and New York, NY, USA, 755 pp., Doi: 10.1017/9781009157964.

ISO 14688-1:2017 (2017): Geotechnical investigation and testing - identification and classification of soil - Part 1: Identification and description. *ISO/TC 182 Geotechnics,* [online] https://www.iso.org/obp/ui/en/#iso:std:iso:14688:-1:ed-2:v1:en, accessed 01.05.2023.

Jenrich, M., Angelopoulos, M., Grosse, G., Overduin, P. P., Schirrmeister, L., Nitze, I., Biskaborn, B. K., Liebner, S., Grigoriev, M., Murray, A., Jongejans, L. L., Strauss, J. (2021): Thermokarst Lagoons: A Core-Based Assessment of Depositional Characteristics and an Estimate of Carbon Pools on the Bykovsky Peninsula. *Frontiers Earth Science*, vol. 9, 637899, Doi: 10.3389/feart.2021.637899.

Jones, M. C., Grosse, G., Jones, B. M., Walter Anthony, K. (2012): Peat accumulation in drained thermokarst lake basins in continuous, ice-rich permafrost, northern Seward Peninsula, Alaska*. Journal of Geophysical Research*, vol. 117, (G00M07), Doi: 10.1029/2011JG001766.

Jonsson, S., Andersson, A., Nilsson, M. B., Skyllberg, U., Lundberg, E., Schaefer, J. K., Åkerblom, S., Björn, E. (2017): Terrestrial discharges mediate trophic shifts and enhance methylmercury accumulation in estuarine biota*. Sciences Advances*, vol. 3, (1), Doi: 10.1126/sciadv.1601239.

Jongejans, L. L., Mangelsdorf, K., Schirrmeister, L., Grigoriev, M. N., Maksimov, G. M., Biskaborn, B. K., Grosse, G., Strauss, J. (2020): n-Alkane Characteristics of Thawed Permafrost Deposits Below a Thermokarst Lake on Bykovsky Peninsula, Northeastern Siberia. *Frontier Environmental Science*, vol. 8, (118), Doi: 10.3389/fenvs.2020.00118.

Jorgenson, M.T. & Grunblatt J. (2013): *Landscape-Level Ecological Mapping of northern Alaska and Field Site Photography.* Final Report for: Arctic Landscape Conservation Cooperative, U.S. Fish and Wildlife Service, Fairbanks, Alaska, [online] https://catalog.northslopescience.org/dataset/8e2d5a71-7808-4ea2-b60b-c2b615fceaa8/resource/7aead4d6-4fe9-4914-bc38-a1e072ff6030/download/n-alaska-landscape-mapping-and-field-site-photography-2013.pdf, accessed 20.04.2023.

Jorgenson, M. T. & Heiner, M. (2003): Ecosystems of Northern Alaska. 1:2.5 million-scale map produced by ABR, Inc., Fairbanks, AK and The Nature Conservancy, Anchorage, AK.

Jorgenson, M.T., Romanovsky, V., Harden, J., Shur, Y., O'Donnell, J., Schuur, E. A. G., Kanevskiy, M., Marchenko, S. (2010): Resilience and vulnerability of permafrost to climate change. *Canadian Journal of Forest Research,* vol. 40, (7), pp. 1219–1236, Doi: 10.1139/X10-060.

Jorgenson, M.T. & Shur, Y. (2007): Evolution of lakes and basins in northern Alaska and discussion of the thaw lake cycle. *Journal of Geophysical Research*, vol. 112, (F02S17), Doi: 10.1029/2006JF000531.

Jorgenson, M. T., Shur, Y., Osterkamp, T., Ping, C., Kanevskiy, M. (2011): Part 1: Environment of the Beaufort Coastal Plain. Jorgenson, T. [ed.], *Coastal Region of Northern Alaska - Guidebook to Permafrost and related features*. Division of Geological & Geophysical Surveys [pub.], Guidebook 10-1, pp. 1-39, Doi: 10.14509/22782.

Kokelj, S. V. & Jorgenson, M. T. (2013): Advances in Thermokarst Research. *Permafrost and Periglacial Processes*, vol. 24, (2), pp. 108-119, Doi: 10.1002/ppp.1779.

Lenz, J., Jones, B. M., Wetterich, S., Tjallingii, R., Fritz, M., Arp, C. D., Rudaya, N., Grosse, G. (2016): Impacts of shore expansion and catchment characteristicson lacustrine thermokarst records in permafrost lowlands, Alaska Arctic Coastal Plain. *Arktos*, vol. 2, (25), Doi: 10.1007/s41063-016-0025-0.

Lijedahl, A. K., Boike, J., Daanen, R. P., Fedorov, A. N., Frost, G. V., Grosse, G., Hinzmann, L. D., Iijma, Y., Jorgenson, J. C., Matveyeva, N., Necsoiu, M., Raynolds, M. K., Romanovsky, V. E., Schulla, J., Tape, K. D., Walker, D. A., Wilson, C. J., Yabuki, H., Zona, D. (2016): Pan-Arctic ice-wedge degradation in warming permafrost and its influence on tundra hydrology. *Nature Geoscience*, vol. 9, pp. 312-318, Doi: 10.1038/ngeo2674.

Marzi, R., Torkelson, B. E., Olson, R. K. (1993): A revised carbon preference index. *Organic Geochemistry*, vol. 20, (8), pp. 1303-1306, Doi: 10.1016/0146-6380(93)90016-5.

Meyers, P. A. (1997): Organic geochemical proxies of paleoceanographic, paleolimnologic, and paleoclimatic processes. *Organic Geochemistry*, vol. 27, (5-6), pp. 213-250, Doi: 10.1016/S0146-6380(97)00049-1.

Miesner, F., Overduin, P. P., Grosse, G., Strauss, J., Langer, M., Westermann, S., Schneider von Deimling, T., Brovkin, V., Arndt, S. (2023): Subsea permafrost organic carbon stocks are large and of dominantly low reactivity. *Scientific Reports*, vol. 13, (9425), Doi: 10.1038/s41598-023-36471-z.

Miner, K. R., Turetsky, M. R., Malina, E., Bartsch, A., Tamminen, J., McGuire, A. D., Fix, A., Sweeney, C., Elder, C. D., Miller, C. E. (2022): Permafrost carbon emissions in a changing Arctic. *Nature Reviews Earth & Environment*, vol. 3, pp. 55-67, Doi:10.1038/ s43017-021-00230-3.

Moore, T. E., Wallace, W. K., Bird, K. J., Karl, S. M., Mull, C. G., & Dillon, J. T. (1994): Geology of northern Alaska. Plafker, G., and Berg, H. C. [eds.], *The Geology of Alaska*, Geological Society of America, v. G-1, pp. 49–140.

Murton, J. B. (2021): What and where are periglacial landscapes? *Permafrost and Periglacial Processes*, vol. 32, pp.186-212, Doi: 10.1002/ppp.2102.

Obrist, D., Agnan, Y., Jiskra, M., Olson, C. L., Colegrove, D. P., Hueber, J., Moore, C. W., Sonke, J. E., Helmig, D. (2017): Tundra uptake of atmospheric elemental mercury drives Arctic mercury pollution. *Nature*, vol. 547, pp. 201-204, Doi: 10.1038/nature22997.

Obu, J., Westermann, S., Bartsch, A., Berdnikov, N., Christiansen, H. H., Dashtseren, A., Delaloye, R., Elberling, B., Etzelmüller, B., Kholodov, A., Khomutov, A., Kääb, A., Leibman, M. O., Lewkowicz, A. G., Panda, S. K., Romanovsky, V., Way, R. G., Westergaard-Nielsen, A., Wu, T., Yamkin, J., Zou, D. (2019): Northern Hemisphere permafrost map based on TTOP modelling for 2000–2016 at 1 mm^2 scale. *Earth-Science* Reviews, vol. 193, pp. 299–316. Doi: 10.1016/j.earscirev.2019.04.023.

Olefeldt, D., Goswami, S., Grosse, G., Hayes, D., Hugelius, G., Kuhry, P., McGuire, A. D., Romanovsky, V. E., Sannel, A. B. K., Schuur, E. A. G., Turetsky, M. R. (2016): Circumpolar distribution and carbon storage of thermokarst landscapes*. Nature Communications*, vol. 7, (13043), Doi: 10.1038/ncomms13043.

Pearce, J. M., Flint, P. L., Atwood, T. C., Douglas, D. C., Adams, L. G., Johnson, H. E., Arthur, S. M., Latty, C. J. (2018): Summary of Wildlife-Related Research on the Coastal Plain of the Arctic National Wildlife Refuge, Alaska 2002-17. *Geological Survey Open-File Report*, 2018-1003, Doi: 10.3133/ofr20181003.

Poynter, J. (1989): *Molecular stratigraphy: The recognition of paleo-climatic signals in organic geochemical data,* PhD, School of Chemistry, University of Bristol, Bristol, 324 pp.

Poynter J. & Eglinton G. (1990): 14. Molecular composition of three sediments from hole 717C: the bengal fan. *Proceeding of the Ocean Drilling Program, Scientific Results*, vol. 116, pp. 155-161.

Radke, M., Willsch, H., Welte, D. H. (1980): Preparative hydrocarbon group type determination by automated medium pressure liquid chromatography. *Analytical chemistry*, vol. 52, (3), pp. 406-411, Doi: 10.1021/ac50053a009.

Rantanen, M., Karpechko, A. Y., Lipponen, A., Nordling, K., Hyvärinen, O., Ruosteenoja, K., Vihma, T., Laaksonen, A. (2022): The Arctic has warmed nearly four times faster than the globe since 1979. *Communications Earth & Environment*, vol. 3, (168), Doi: 10.1038/s43247-022-00498-3.

Rawlinson, S. E. (1990): Surficial Geology and Morphology of the Alaskan Central Arctic Coastal Plain. *Alaska Division of Geological & Geophysical Surveys*, Public-data File 90-27, Doi: 10.14509/1461.

Reimer, P. J., Bard, E., Bayliss, A. J., Beck, W., Blackwell, P. G., Ramsey, C. B., Buck, C. E., Cheng, H., Edwards, R. L., Friedrich, M., Grootes, P. M., Guilderson, T. P., Haflidason, H., Hajdas, I., Hatté, C., Heaton, T. J., Hoffmann, D. L., Hogg, A. G., Hughen, K. A., Kaiser, K. F., Kromer, B., Manning, S. W., Niu, M., Reimer, R. W., Richards, D. A., Scott, E. M., Southon, J. R., Staff, R. A., Turney, C. S. M., van der Plicht, J. (2013): IntCal13 and Marine13 Radiocarbon Age Calibration Curves 0–50,000 Years Cal BP. Radiocarbon, vol. 55, (4), pp. 1869–87, Doi: 10.2458/azu_js_rc.55.16947.

Richter-Menge, J., Overland, J. E., Mathis, J. T., Osborne, E. E. (2017): *Arctic Report Card 2017*. [online] www.arctic.noaa.gov/Report-Card, accessed 06.06.2023.

Romanovskii, N., Hubberten, H.-W., Gavrilov, A.V., Tumskoy, V. E., Tipenko, G. S., Grigoriev, M. N., Siegert, Ch. (2000): Thermokarst and Land-Ocean Interactions, Laptev Sea Region, Russia. *Permafrost and Periglacial Processes*, vol. 11, (2), pp. 137-152, Doi: 10.1002/1099-1530(200004/06)11:23.0.CO;2-L.

Routh, J., Hugelius, G., Kuhry, P., Filley, T., Tillman, P. K., Becher M., Crill, P. (2014): Multi-proxy study of soil organic matter dynamics in permafrost peat deposits reveal vulnerability to climate change in the European Russian Arctic. Chemical Geology, vol. 368, pp. 104-117, Doi: 10.1016/j.chemgeo.2013.12.022.

Rowell, D. L. (1994): Soil science: Methods & applications. Longman Scientific & Technical, Longman Group UK, Doi:10.1002/jsfa.2740660423.

Rutkowski, K., Lenz, J., Lang, A., Wolter, J., Mothes, S., Reemtsma, T., Grosse, G., Ulrich, M., Fuchs, M., Schirrmeister, L., Fedorov, A., Grigoriev, M., Lantuit, H., Strauss, J. (2021): Mercury in Sediment Core Samples from Deep Siberian Ice-Rich Permafrost. *Frontiers in Earth Science*, vol. 9, (718153), Doi: 10.3389/feart.2021.718153.

Ruz, M.-H., Héquette, A., Hill, P. R. (1992): A model of coastal evolution in a transgressed thermokarst topography, Canadian Beaufort Sea. *Marine Geology*, vol. 10, (3-4), pp. 251-278, DOI: 10.1016/0025-3227(92)90133-3.

Rydberg, J., Klaminder, J., Rosén, P., Bindler, R. (2010): Climate driven release of carbon and mercury from permafrost mires increases mercury loading to sub-arctic lakes. *Science of the Total Environment*, vol. 408, (20), pp. 4778-4783, Doi: 10.1016/j.scitotenv.2010.06.056.

Schäfer, I. K., Lanny, V., Franke, J., Eglinton T., Zech, M., Vyslouzilová, B., Zech R. (2016): Leaf waxes in litter and topsoils along a European transect. *SOIL,* vol. 2, pp. 551-564, Doi: 10.5194/soil-2-551-2016.

Schirrmeister, L., Grigoriev, M. N., Strauss, J., Grosse, G., Overduin, P. P., Kholodov, A., Guenther, F., Hubberten, H.-W. (2018): Sediment characteristics of a thermokarst lagoon in the northeastern Siberian Arctic (Ivashkina Lagoon, Bykovsky Peninsula). *Arktos,* vol. 4, (13), pp. 16, Doi: 10.1007/s41063-018-0049-8.

Schirrmeister, L., Grosse, G., Wetterich, S., Overduin, P. P., Strauss, J., Schuur, E. A. G., Hubberten, H. (2011a): Fossil organic matter characteristics in permafrost deposits of the northeast Siberian Arctic. *Journal of Geophysical Research Biogeosciences*, vol. 116, (G2), Doi: 10.1029/2011JG001647.

Schirrmeister, L., Siegert, C., Strauß, J. (2011b): Permafrost ein sensibles Klimaphänomen – Begriffe, Klassifikationen und Zusammenhänge (Permafrost a sensible climate phenomenon – terms, classifications, and relationships). *Polarforschung,* vol. 81, (1), pp.3-10.

Schuster, P. F., Schaefer, K. M., Aiken, G. R., Antweiler, R. C., Dewild, J. F., Gryziec, J. D., Gusmeroli, A., Hugelius, G., Jafarov, E., Krabbenhoft, D. P., Liu, L., Herman-Mercer, N., Mu, C., Roth, D. A., Schaefer, T., Striegl, R. G., Wickland, K. P., Zhang, T. (2018): Permafrost Stores a Globally Significant Amount of Mercury. *Geophysical Research Letters*, vol. 45, (3), pp. 1463-1471, Doi: 10.1002/2017GL075571.

Schuur, E. A. G., Mack, M. C. (2018): Ecological Response to Permafrost Thaw and Consequences for Local and Global Ecosystem Services. *Annual Review of Ecology, Evolution, and Systematics*, vol. 49, pp. 279-301, Doi: 10.1146/annurev-ecolsys-121415-032349.

Schuur, E. A. G, McGuire, A. D., Schädel, C., Grosse, G., Harden, J. W., Hayes, D. J., Hugelius, G., Koven, C. D., Kuhry, P., Lawrence, D. M., Natali, S. M., Olefeldt, D., Romanovsky, V. E., Schaefer, K., Turetsky, M. R., Treat, C. C. Vonk J. E. (2015): Climate change and the permafrost carbon feedback. *Nature,* vol. 520, pp. 171-179, Doi: 10.1038/nature14338.

Schuur, E. A. G., Vogel, J. G., Crummer, K. G., Lee, H., Sickman, J. O., Osterkamp, T. E. (2009): The effect of permafrost thaw on old carbon release and net carbon exchange from tundra. *Nature*, vol. 459, pp. 556-559, Doi: 10.1038/nature08031.

Schwarzbauer, J. & Jovančićević, B. (2016): *From Biomolecules to Chemofossils. Fundamentals in Organic Geochemistry*, Springer International, Switzerland, Doi: 10.1007/978-3-319-25075-5.

Shur, Y. L., & Jorgenson, M. T. (2007): Patterns of Permafrost Formation and Degradation on Relation to Climate and Ecosystems. *Permafrost and Periglacial Processes*, vol. 18, (1), pp. 7-19, Doi: 10.1002/ppp.582.

Smith-Downey, N. V., Sunderland, E. M., Jacob, D. J. (2010): Anthropogenic impacts on global storage and emissions of mercury from terrestrial soils: Insights from a new global model. *Journal of Geophysical Research*, vol. 115, (G03008), Doi: 10.1029/2009JG001124.

Strauss, J., Abbott, B. W., Hugelius, G., Schuur, E., Treat, C., Fuchs, M., Schädel, C., Ulrich, M., Turetsky, M., Keuschnig, M., Biasi, C., Yang, Y., Grosse, G. (2021): Permafrost. *Recarbonizing global soils– A technical manual of recommended management practices, Hot spots and bright spots of soil organic carbon*, vol. 2, pp. 130-150, Doi: 10.4060/cb6378en.

Strauss, J., Schirrmeister, L., Grosse, G., Fortier, D., Hugelius, G., Knoblauch, C., Romanovsky, V., Schädel, C., Schneider von Deimling, T., Schuur, E. A. G, Shmelev, D., Ulrich, M., Veremeeva, A. (2017): Deep Yedoma permafrost: A synthesis of depositional characteristics and carbon vulnerability. *Earth-Science Reviews*, vol. 172, pp. 75-86, Doi: 10.1016/j.earscirev.2017.07.007.

Strauss, J., Schirrmeister, L., Grosse, G., Wetterich, S., Ulrich, M., Herzschuh, U., Hubberten, H. (2013): The deep permafrost carbon pool of the Yedoma region in Siberia and Alaska. *Geophysical Research Letters*, vol. 40, (23), pp. 6165-6170, Doi: 10.1002/2013GL058088.

Strauss, J., Schirrmeister, L., Mangelsdorf, K., Eichhorn, L., Wetterich, S., Herzschuh, U. (2015): Organic-matter quality of deep permafrost carbon – a study from Arctic Siberia. *Biogeosciences*, vol. 12, (7), pp. 2227-2245, Doi: 10.5194/bg-12-2227-2015.

Strauss, J. Schirrmeister, L., Wetterich, S., Borchers, A., Davydov, S. P. (2012): Grain-size properties and organic-carbon stock of Yedoma Ice Complex permafrost from the Kolyma lowland, northeastern Siberia. *Global Biogeochemical Cycles*, vol. 26, (3), Doi: 10.1029/2011GB004104.

Thomas, C. L., Jansen, B., Czerwinski, S., Galka M., Knorr, K., van Loon, E. E., Egli, M., Wiesenberg, G. L. B. (2023): Comparison of paleobotanical and biomarker records of mountain peatland and forest ecosystem dynamics over the last 2600 years in Central Germany. *Biogeosciences - Discussions*, Doi: 10.5194/bg-2023-57.

van Everdingen, R. O. [ed.] (1998): *Multi-Language Glossary of Permafrost and Related Ground-Ice Terms*, revised 2005, International Permafrost Association (IPA), [online] https://globalcryospherewatch.org/reference/glossary_docs/Glossary_of_Permafrost_and_Ground-Ice_IPA_2005.pdf, accessed 04.07.2023.

Weintraub, M. N. & Schimel, J. P. (2005): Nitrogen Cycling and the Spread of Shrubs Control Changes in the Carbon Balance of Arctic Tundra Ecosystems. *BioScience,* vol. 55, (5), pp. 408-415, Doi: 10.1641/0006-3568(2005)055[0408:NCATSO]2.0.CO;2.

Wendler, G., Moore, B., Galloway, K. (2014): Strong Temperature Increase and Shrinking Sea Ice in Arctic Alaska. *The Open Atmospheric Science Journal,* vol. 8, (1), pp. 7-15, Doi: 10.2174/1874282301408010007.

Yang, S., Anthony, S. E., Jenrich, M., in 't Zandt, M. H, Strauss, J., Overduin, P. P., Grosse, G., Angelopoulos, M., Biskaborn, B. K., Grigoriev, M. N., Wagner, D., Knoblauch, C., Jaeschke, A., Rethemeyer, J., Kallmeyer, J., Liebner, S. (2023): Microbial methane cycling in sediments of Arctic thermokarst lagoons. *Global Change Biology*, vol. 29, (10), pp. 2714-2731, Doi: 10.1111/gcb.16649.

Zech, M., Buggle, B., Leiber, K., Markovic, S., Glaser, B., Hambach, U., Huwen, B., Stevens, T., Sümegi, P., Wiesenberg, G., Zöller, L. (2009): Reconstructing Quaternary vegetation history in the Carpathian basin, SE Europe, using n-alkane biomarkers as molecular fossils. *Quaternary Science Journal,* vol. 58, (2), pp. 148-155, Doi: 10.3285/eg.58.2.03.

Zheng, Y., Zhou, W., Meyers, P. A., Shucheng, X. (2007): Lipid biomarkers in the Zoigeˆ-Hongyuan peat deposit: Indicators of Holocene climate changes in West China. *Organic Geochemistry,* vol. 38, (11), pp. 1927-1940, Doi: 10.1016/j.orggeochem.2007.06.012.

Appendix

Table A.1: Raw data sedimentological parameters

Prefix	mean depth [cm b.s.l.]	dry bulk density [g/cm³]	absolute ice/ water content [wt%]	mean grain size [µm]	clay [vol%]	silt [vol%]	sand [vol%]
TES22-MAR1-02	6.25	1.529	19.619	33.31	7.126	34.419	58.455
TES22-LAG1-01	1.5	NA	NA	5.001	19.8	77.3	2.9
TES22-LAG1-01	7.75	615	53.412	6.882	17.27	77.779	4.956
TES22-LAG1-01	16	1.058	34.258	6.6	18.90	76.015	5.086
TES22-LAG1-01	26.5	1.123	32.035	5.432	20.23	73.67	6.098
TES22-LAG1-01	36.5	NA	3.410	6.824	16.46	80.442	3.093
TES22-LAG1-01	46.75	1.321	25.847	6.608	17.028	80.144	2.827
TES22-LAG1-01	59	1.342	25.230	5.917	20.19	74.656	5.154
TES22-LAG1-01	74	NA	14.271	16.07	6.409	87.715	5.876
TES22-LAG1-01	87	1.246	28.075	5.919	20.375	73.221	6.404
TES22-LAG1-01	103	NA	15.044	45.87	4.998	41.385	53.616
TES22-LAG1-01	116	NA	14.612	23.85	9.545	57.352	33.102
TES22-LAG1-01	129.5	NA	15.181	20.79	9.571	66.263	24.166
TES22-LAG1-01	145.75	1.436	22.659	25.25	7.462	64.803	27.735
TES22-LAG1-01	159.5	1.532	20.181	23.59	7.982	66.864	25.154
TES22-LAG1-01	179	1.415	23.219	17.33	10.257	63.679	26.064
TES22-TKL1-02	6	713	51.935	5.623	21.413	74.363	4.223
TES22-TKL1-02	13	NA	43.603	9.93	14.395	79.624	5.981
TES22-TKL1-02	18	NA	44.562	5.752	19.401	77.317	3.281
TES22-TKL1-02	25.5	NA	42.050	5.224	21.379	74.342	4.278

Prefix	mean depth [cm b.s.l.]	dry bulk density [g/cm³]	absolute ice/ water content [wt%]	mean grain size [µm]	clay [vol%]	silt [vol%]	sand [vol%]
TES22-TKL1-02	32	NA	38.500	5.404	21.336	73.554	5.11
TES22-TKL1-02	37.5	NA	40.249	6.825	17.134	78.837	4.029
TES22-TKL1-02	45.25	1.057	37.958	7.155	16.9	80.365	2.729
TES22-DLB1-01	6.75	45	95.238	NA	NA	NA	NA
TES22-DLB1-01	18.5	245	77.255	NA	NA	NA	NA
TES22-DLB1-01	28.5	1.251	27.933	6.646	17.943	78.637	3.42
TES22-DLB1-01	42.5	501	59.799	5.742	21.878	73.307	4.815
TES22-DLB1-01	60.5	619	53.207	6.497	18.081	77.5	4.4191
TES22-DLB1-01	76	390	66.737	6.735	17.294	79.214	3.492
TES22-DLB1-01	100	458	62.360	5.768	20.234	76.409	3.357
TES22-DLB1-01	117	368	68.255	6.618	18.148	78.53	3.322
TES22-DLB1-01	137	484	60.812	6.381	18.028	78.521	3.452
TES22-DLB1-01	157	728	47.767	6.13	17.973	78.804	3.223
TES22-DLB1-01	174.5	468	61.756	6.621	17.793	79.91	2.298
TES22-DLB1-01	193	674	50.362	5.7	19.421	77.109	3.47
TES22-DLB1-01	215	817	43.711	5.981	18.657	74.594	6.748
TES22-UPL1-02	7	1.031	35.237	21.73	9.545	63.483	26.971
TES22-UPL1-02	22.5	1.396	23.742	20.42	8.947	65.526	25.527
TES22-UPL1-02	33.5	1.477	21.579	13.33	12.550	70.286	17.164
TES22-UPL1-02	47.5	1.509	20.753	13.64	12.754	69.633	17.612
TES22-UPL1-02	56	586	54.959	11.74	11.161	73.816	15.024
TES22-UPL1-02	76	625	52.890	14.3	13.043	68.63	18.327

Prefix	mean depth [cm b.s.l.]	dry bulk density [g/cm³]	absolute ice/ water content [wt%]	mean grain size [µm]	clay [vol%]	silt [vol%]	sand [vol%]
TES22-UPL1-02	85	542	57.396	12.71	15.042	64.772	20.186
TES22-UPL1-02	126	497	60.037	6.497	18.081	77.5	4.4191
TES22-UPL1-02	149.5	381	67.339	14.37	13.572	65.043	21.385
TES22-UPL1-02	173.5	573	55.688	17.8	11.299	64.803	23.898
TES22-UPL1-02	195	541	57.476	18.55	11.376	65.799	22.825
TES22-LAG2-01	5	NA	41.252	6.78	14.708	82.074	3.2172
TES22-LAG2-01	27	977	36.989	6.019	18.547	77.315	4.138

Table A.2: Raw data biogeochemical parameter

Prefix	mean depth [cm b.s.l.]	TC [wt%]	TOC [wt%]	TOCvol [kg/m³]	TN [wt%]	C/N ratio	δ13C [‰ vs. VPDB]	mercury [µg/kg]
TES22-MAR1-02	6.25	1.548	1.297	19.826	< 0.10	25.934	-26.208	30.68
TES22-LAG1-01	1.5	3.529	3.499	21.341	326	10.732	-27.788	66.201
TES22-LAG1-01	7.75	4.652	4.619	28.405	322	14.323	-27.549	69.869
TES22-LAG1-01	16	3.362	3.33	35.241	236	14.082	-27.263	72.095
TES22-LAG1-01	26.5	4.473	4.442	49.869	312	14.261	-27.603	102.168
TES22-LAG1-01	36.5	3.05	3.026	36.968	234	12.931	-27.543	73.913
TES22-LAG1-01	46.75	3.42	3.393	44.816	263	12.925	-27.59	80.988
TES22-LAG1-01	59	3.587	3.56	47.783	259	13.743	-27.659	82.112
TES22-LAG1-01	74	733	718	9.288	< 0.10	14.354	-27.388	20.268
TES22-LAG1-01	87	2.816	2.788	34.745	0.22	12.704	-26.361	61.135

Prefix	mean depth [cm b.s.l.]	TC [wt%]	TOC [wt%]	TOCvol [kg/m³]	TN [wt%]	C/N ratio	δ13C [‰ vs. VPDB]	mercury [µg/kg]
TES22-LAG1-01	103	1.188	736	9.2	< 0.10	14.72	-26.122	15.572
TES22-LAG1-01	116	1.524	986	13.267	< 0.10	19.727	-26	22.517
TES22-LAG1-01	129.5	1.408	1.059	15.25	< 0.10	21.18	-25.445	24.601
TES22-LAG1-01	145.75	1.453	999	14.347	< 0.10	19.986	-25.647	23.025
TES22-LAG1-01	159.5	1.549	1.028	15.752	< 0.10	20.565	-25.321	19.603
TES22-LAG1-01	179	1.477	1.352	19.13	111	12.236	-28.345	48.653
TES22-TKL1-02	6	5.275	5.211	37.182	365	14.278	NA	77.852
TES22-TKL1-02	13	4.692	4.629	33.024	337	13.735	-28.211	64.101
TES22-TKL1-02	18	6.302	6.232	44.462	418	14.909	-28.225	72.072
TES22-TKL1-02	25.5	5.386	5.338	47.243	378	14.121	-28.463	69.887
TES22-TKL1-02	32	5.04	4.985	44.12	359	13.905	-28.09	68.262
TES22-TKL1-02	37.5	5.926	5.868	62.007	388	15.144	-28.1	72.363
TES22-TKL1-02	45.25	5.362	5.311	56.112	364	14.609	NA	70.627
TES22-DLB1-01	6.75	37.729	37.618	16.973	644	58.458	-28.006	48.781
TES22-DLB1-01	18.5	18.83	18.707	45.88	0.99	18.906	-27.44	103.546
TES22-DLB1-01	28.5	3.181	3.152	39.421	233	13.528	-27.735	72.143
TES22-DLB1-01	42.5	3.3118	3.27	16.371	0.23	14.25	-27.476	70.067
TES22-DLB1-01	60.5	8.465	8.384	51.88	509	16.471	-27.104	72.108
TES22-DLB1-01	76	2.989	2.941	11.477	226	13.015	-27.235	63.873
TES22-DLB1-01	100	3.566	3.501	16.043	251	13.948	-27.508	67.547
TES22-DLB1-01	117	3.321	3.261	11.991	219	14.924	-27.385	66.208
TES22-DLB1-01	137	3.148	3.095	14.969	253	12.258	-27.344	67.095

Prefix	mean depth [cm b.s.l.]	TC [wt%]	TOC [wt%]	TOCvol [kg/m³]	TN [wt%]	C/N ratio	δ13C [‰ vs. VPDB]	mercury [µg/kg]
TES22-DLB1-01	157	2.993	2.946	21.451	252	11.715	-27.243	67.994
TES22-DLB1-01	174.5	3.058	3.0186	14.13	222	13.597	-27.423	69.814
TES22-DLB1-01	193	3.199	3.168	21.367	256	12.374	-27.789	70.186
TES22-DLB1-01	215	5.42	5.363	43.839	382	14.057	-28.106	68.904
TES22-UPL1-02	7	2.581	2.559	26.377	0.12	21.412	-28.84	48.506
TES22-UPL1-02	22.5	3.243	3.214	44.853	0.17	18.96	-29.007	49.836
TES22-UPL1-02	33.5	3.228	3.2	47.264	169	18.993	-29.028	47.874
TES22-UPL1-02	47.5	4.935	4.889	73.782	278	17.618	-28.695	48.88
TES22-UPL1-02	56	20.512	20.421	119.669	1.202	16.997	-27.578	66.244
TES22-UPL1-02	76	4.056	3.841	24.003	228	16.829	-27.766	33.253
TES22-UPL1-02	85	6.175	5.929	32.136	338	17.54	-27.1588	36.344
TES22-UPL1-02	126	3.184	2.47	12.263	145	17.032	-27.33	28.515
TES22-UPL1-02	149.5	2.608	1.929	7.352	124	15.553	-27.101	29.268
TES22-UPL1-02	173.5	2.417	1.532	8.772	< 0.10	30.639	-26.69	27.196
TES22-UPL1-02	195	2.192	1.256	6.789	0.11	11.416	-26.103	25.898
TES22-LAG2-01	5	4.123	4.092	39.987	312	13.137	-27.628	66.629
TES22-LAG2-01	27	4.71	4.676	45.697	357	13.099	-27.758	70.667

Table A.3: Raw Data Hydrochemistry

Prefix	mean depth [cm b.s.l.]	pH	electric conductivity [mS/cm]	DOC [mg/L]
TES22-MAR1-02	6.25	7.67	39.5	19.23
TES22-LAG1-01	7.75	7.49	39	80.8
TES22-LAG1-01	87	5.94	61.5	NA
TES22-LAG1-01	179	7.58	17.85	NA
TES22-TKL1-02	6	7.45	832	NA
TES22-DLB1-01	6.75	4.52	261	52.3
TES22-DLB1-01	60.5	6.99	672	187
TES22-DLB1-01	215	6.61	333	378
TES22-UPL1-02	7	6.44	311	72.28
TES22-UPL1-02	56	7.32	361	NA
TES22-UPL1-02	195	7.25	1.156	228
TES22-LAG2-01	5	7.64	54.6	NA

Table A.4: Calibrated radiocarbon ages

Prefix	mean depth [cm b.s.l.]	calibrated age from [yrBP]	calibrated age to [yrBP]	calibrated mean [yrBP]	uncertainty [yrBP]
TES22-MAR1-02	6	15772	16288	16061	89
TES22-LAG2-01	11.25	2289	2496	2410	41
TES22-TKL1-02	13	4532	4691	4600	29
TES22-TKL1-02	37.5	4058	4330	4240	28

Prefix	mean depth [cm b.s.l.]	calibrated age from [yrBP]	calibrated age to [yrBP]	calibrated mean [yrBP]	uncertainty [yrBP]
TES22-DLB1-01	21.5	NA	NA	recent	29
TES22-DLB1-01	193	543	653	645	34
TES22-LAG1-01	16	NA	NA	recent	32
TES22-LAG1-01	179	40465	43721	41962	1250
TES22-UPL1-02	22.5	NA	NA	recent	21
TES22-UPL1-02	195	9262	9672	9412	65

Table A.5: *n*-alkane concentrations [µg/g_{TOC}]

Prefix	mean depth [cm b.s.l.]	nC^{11}	nC^{12}	nC^{13}	nC^{14}	nC^{15}	nC^{16}	nC^{17}	nC^{18}	nC^{19}	nC^{20}	nC^{21}	nC^{22}	nC^{23}	nC^{24}	nC^{25}	nC^{26}	nC^{27}	nC^{28}	nC^{29}	nC^{30}	nC^{31}	nC^{32}	nC^{33}	Total concen-tration
TES22-MAR1-02	6.25	0	0	0	0.1	0	0.1	0.5	1	2.0	2.3	5.5	3.6	10.5	2.5	9.3	1.4	11.4	0.7	6.3	0	3.8	0	0.6	61.89
TES22-LAG2-01	5	0	0	0	0.0	0.3	1.3	3.7	3.8	10.2	10.5	36.0	27.5	83.5	19.1	65.2	13.2	93.3	7.6	50.5	2.9	31.4	1.0	5.9	466.83
TES22-LAG2-01	27	0	0	0.0	0.1	0.5	1.1	4.3	5.3	12.9	12.6	53.5	37.3	113	27.1	93.5	22.2	124	14.1	80.4	6.4	49.8	2.2	8.7	669.32
TES22-TKL1-02	6	0	0.0	0.0	0.0	0.3	0.8	2.5	3	6.9	6.2	25.8	15.9	61.8	12.5	55.9	9.3	88.3	5.8	48.4	2.0	37.5	1.9	7.7	392.55
TES22-TKL1-02	44.7	0.1	0.1	0.1	0.4	0.7	1.1	3.0	3.1	7.5	6.8	29.6	16.9	71.7	15.8	68.0	12.9	119	7.5	71.9	2.8	50.5	2.6	10.5	502.39
TES22-LAG1-01	8.75	0.1	0.1	0.0	0.4	0.7	2.1	3.7	5.4	8.8	8.4	30.8	18.4	66.8	14.7	52.5	8.7	62.6	4.6	40.3	2.1	33.0	1.5	7.2	372.8
TES22-LAG1-01	91	0	0.0	0	0	0.1	0.5	1.8	2.5	3.8	4	8.4	6.3	15.8	5.8	20.3	4.0	29.5	3.0	21.8	1.2	16.3	0.5	4.2	149.66
TES22-LAG1-01	174	0	0.1	0	0	0.1	0.5	2	3.7	6.4	6.6	13.9	10.4	28.9	9.7	26.9	5.7	37.9	4.2	29.5	1.9	21.8	1.1	5.4	216.62
TES22-UPL1-02	7	0.0	0.1	0.1	0.2	0.3	1.3	2.5	4.9	11.1	10.7	24.2	29.5	37.8	21.6	57.9	13.7	122	8.5	72.0	4.4	76.2	2.5	16.5	517.5
TES22-UPL1-02	56	0.0	0.0	0.0	0.2	0.2	0.5	1.3	1.6	3.9	3.0	13.1	11.1	27.5	13.0	50.5	11.6	78.5	10.5	70.5	6.1	99.8	6.7	37.3	447.25
TES22-UPL1-02	166	0.0	0.0	0	0.1	0.2	1.2	2.7	4.4	6.5	5.3	12.6	11.2	20.4	8.5	34.4	5.7	63.0	4.7	40.3	2.5	54.2	1.3	10.4	289.54
TES22-DLB1-01	6.75	0.0	0.0	0.0	0.0	0.1	0.1	2.1	0.4	0.8	0.9	9.6	3.8	22.2	4.6	43.8	4.6	51.2	4.0	21.9	1.2	11.5	0.7	1.5	185.09

Prefix	mean depth [cm b.s.l.]	nC^{11}	nC^{12}	nC^{13}	nC^{14}	nC^{15}	nC^{16}	nC^{17}	nC^{18}	nC^{19}	nC^{20}	nC^{21}	nC^{22}	nC^{23}	nC^{24}	nC^{25}	nC^{26}	nC^{27}	nC^{28}	nC^{29}	nC^{30}	nC^{31}	nC^{32}	nC^{33}	Total concentration
TES22-DLB1-01	65	0.0	0.0	0.0	0.2	0.3	0.5	1.0	1.4	2.7	2.1	8.1	7.9	21.4	4.3	29.4	4.2	63.4	3.7	45.2	1.6	28.5	0.9	5.0	231.89
TES22-DLB1-01	132	0.0	0.1	0.1	0.5	1.1	1.8	4.1	4.3	7.4	6.8	21.2	23.3	50.4	11.2	52.2	9.1	91.5	6.2	57.7	3.2	47.6	1.4	9.7	410.95
TES22-DLB1-01	208	0.1	0.1	0.1	0.8	1.4	2.2	5.5	6.4	16.1	11.6	62.4	43.0	136	34.1	135	24.0	195	19.5	181	11.2	162	7.4	35.7	1090.3

Table A.6: *n*-alkanol concentrations [µg/g_{TOC}]

Prefix	mean depth [cm b.s.l.]	C^{13}-OH	C^{14}-OH	C^{15}-OH	C^{16}-OH	C^{17}-OH	C^{18}-OH	C^{19}-OH	C^{20}-OH	C^{21}-OH	C^{22}-OH	C^{23}-OH	C^{24}-OH	C^{25}-OH	C^{26}-OH	C^{27}-OH	C^{28}-OH	C^{29}-OH	C^{30}-OH	Total concentration
TES22-MAR1-02	6.25	0.0	0.0	0.0	0.0	0.0	0.8	0.0	6.0	0.9	14.5	1.4	12.8	1.8	17.3	1.2	34.1	0.0	1.1	91.74
TES22-LAG2-01	5	0.0	0.0	0.0	0.1	0.0	0.3	0.0	8.6	2.1	21.1	3.6	25.2	5.2	35.6	7.0	175.5	2.9	26.8	313.95
TES22-LAG2-01	27	1.4	2.2	2.0	5.8	3,4	17.1	9.4	299.5	52.5	365.3	68.9	272.5	45.4	246.9	37.0	559.7	5.1	119.5	2113.6
TES22-TKL1-02	6	0.5	1.0	1.3	4.1	2,3	7.1	4.0	80.3	14.2	114.2	14.7	82.7	11.7	0.0	8.4	203.7	0,0	38.2	588.38
TES22-TKL1-02	44.75	0.7	1.4	1.6	4.2	2,6	7.8	5.0	118.5	20.1	204.6	32.4	188.6	26.1	186.5	23.9	425.7	10.0	86.5	1346.3
TES22-LAG1-01	8.75	0.0	0.5	0.6	3.8	1,3	11.4	4.2	148.5	16.4	145.3	18.1	107.6	14.8	107.0	12.1	295.7	5.5	51.1	943.81
TES22-LAG1-01	91	0.0	0.0	0.0	0.4	0.0	0.7	0.0	3.1	1.1	18.1	0.0	26.1	3.5	46.9	3.3	55.4	1.3	12.2	171.99
TES22-LAG1-01	173.5	0.0	0.0	0.0	0.2	0.0	0.2	0.0	0.5	0.0	4.8	1.1	10.4	1.9	22.2	3.1	45.2	0.0	12.2	101.78
TES22-UPL1-02	7	0.0	0.0	0.0	1.7	1,9	11.5	6.3	259.2	20.1	313.6	28.2	253.1	27.8	229.2	20.3	383.3	7.7	74.6	1638.6
TES22-UPL1-02	56	0.1	0.2	0.5	1.8	3,3	10.0	5.4	117.7	8.4	113.3	8.5	102.6	8.1	77.7	6.4	99.7	0.0	0.0	563.76
TES22-UPL1-02	165.5	0.0	0.5	0.0	2.9	2,3	16.4	2.0	340.3	5.3	146.4	0,0	77.9	7.0	106.9	3.6	95.2	0.0	20.3	827.00
TES22-DLB1-01	6.75	0.1	0.7	1.4	3.5	1,3	2.1	0.5	6.6	2.9	67.3	6.8	86.5	5.7	84.6	6.2	98.3	3.3	16.3	394.05
TES22-DLB1-01	65.25	0.0	0.2	0.0	0.6	0,4	5.3	1.9	117.3	4.9	77.0	6.9	83.4	8.2	85.3	11.9	300.9	0.0	58.1	762.27
TES22-DLB1-01	131.5	0.0	0.3	0.0	1.6	0,5	2.8	1.9	35.7	8.5	97.9	13.5	104.7	17.2	134.7	16.8	383.9	8.4	67.0	895.27
TES22-DLB1-01	208	0.6	1.9	1.7	11.5	2,8	18.8	6.9	273.0	40.3	360.6	67.7	364.0	58.7	374.5	49.8	640.9	21.9	201.3	2497.0

Table A.7: *n*-alkane and *n*-alkanol indices

Prefix	mean depth [cm b.s.l.]	ACL-short (C_{15-21})	ACL-long (C_{23-33})	P_{aq}	P_{wax}	CPI-alk-short (C_{15-21})	CPI-alk-long (C_{23-33})	CPI-alc (C_{22-32})	HPA
TES22-MAR1-02	6.25	19.94	26.2	0.66	0.52	1.57	7.85	16.68	0.75
TES22-LAG2-01	5	20.01	26.33	0.64	0.54	2.07	6.51	14.67	0.57
TES22-LAG2-01	27	20.11	26.47	0.61	0.55	2.33	5.67	8.83	0.81
TES22-TKL1-02	6	20.02	26.72	0.58	0.6	2.25	8.43	11.0	0.62
TES22-TKL1-02	44.75	19.98	26.89	0.53	0.63	2.31	8.43	10.7	0.77
TES22-LAG1-01	8.75	19.81	26.49	0.62	0.53	1.78	7.13	12.56	0.79
TES22-LAG1-01	91	19.61	27.15	0.49	0.65	1.4	6.74	18.52	0.66
TES22-LAG1-01	173.5	19.75	26.94	0.52	0.62	1.42	5.92	15.17	0.47
TES22-UPL1-02	7	19.8	27.55	0.39	0.74	1.54	6.98	13.05	0.76
TES22-UPL1-02	56	19.94	28.37	0.31	0.76	2.31	6.93	14.67	0.53
TES22-UPL1-02	165.5	19.49	27.8	0.37	0.74	1.43	9.16	34.97	0.64
TES22-DLB1-01	6.75	20.04	26.49	0.66	0.56	5.26	9.32	14.56	0.76
TES22-DLB1-01	65.25	19.74	27.41	0.41	0.73	1.94	12.31	20.94	0.77
TES22-DLB1-01	131.5	19.58	27.11	0.49	0.66	1.75	8.98	13.24	0.76
TES22-DLB1-01	208	20.01	27.4	0.44	0.66	2.66	7.88	8.89	0.72

R-script A.1: Correlation Matrices

```
####################################
###  Correlation Matrix ##############
####################################

## clear the environment
rm(list = ls())

## required packages
library("corrplot")
library("readxl")

# Load data
cm_data <- read_excel(“/Data/path/correlation_matrix.xlsx“)

# Create Correlation Matrix
Correlationm <- cor(cm_data)

# Create Correlation Matrix with p-value ( > 0.05)
Correlationp <- cor.mtest(cm_data)

# start the plot
pdf(file = “Data/path/correlation_matrix.pdf“,
    width = 20,
    height = 20)
```

```
# Plot with numbers
corrplot(Correlationm, method = "number", p.mat=Correlationp$p, insig = "blank",
         tl.col = "black", tl.srt = 59, tl.cex = 3,
         number.cex = 2, label.srt = 50)

# add the second half of the plot (points)
corrplot(Correlationm, p.mat=Correlationp$p, insig = "blank", type = "upper", tl.pos = "n", tl.cex =1.5, add = TRUE)

# create the plot
dev.off()
```

R-script A.2: Cluster Analysis

```
#####################################
### K-means Cluster Analysis  ############
#####################################

## clear the environment
rm(list = ls())

## required packages
library("tidyverse")
library("cluster")
library("factoextra")
library("readxl")
library("broom")
```

```
# load and prepare the data
cluster <- read_excel(“/Data/path/Cluster_analysis.xlsx“)

#converting the "Tibble" to a dataframe
cluster <- as.data.frame(cluster)

# extracting first column
name_vector <- cluster[, 1]

# remove first column from the dataframe
cluster <- cluster[, -1]

# rename the rows
rownames(cluster) <- name_vector

## Scaling/ standardizing data
cluster <- scale(cluster)
head(cluster)

## compute the distance matrix
distance <- get_dist(cluster)
fviz_dist(distance, gradient = list(low = "#00AFBB", mid = "white", high = "#FC4E07"))

## computing the k-means clustering (4 clusters)
k4 <- kmeans(cluster, centers = 4, nstart = 50)
str(k4)
k4
```

```
#plot the results
fviz_cluster(k4, data = cluster)
```

R-script A.3: Central Tendency Analysis

```
########################################
### Central Tendency Analysis ##########
########################################

########################################
# Kruskal-Wallis-Test   (SDLAG, TKL, DLB, UPL) #

## required packages
library("psych")
library("rstatix")
library("dplyr")
library("readxl")

## Load data
kw_data <- read_excel("/Data/path/kruskal-wallis.xlsx")
### Information -> 4 groups: 1. SDLAG, 2. TKL, 3. DLB, 4. UPL

###TOC
# descriptive statistic by group
describeBy(kw_data$TOC,kw_data$Prefix)
```

```
# Using Kruskal-Wallis-Test, TOC
kruskal.test(kw_data$TOC~kw_data$Prefix)
# results: Kruskal-Wallis chi-squared = 13,973, df = 3, p-value = 0.002942

###TOCvol
# descriptive statistic by group
describeBy(kw_data$TOCvol,kw_data$Prefix)

# Using Kruskal-Wallis-Test, TOCvol
kruskal.test(kw_data$TOCvol~kw_data$Prefix)
# results: Kruskal-Wallis chi-squared = 6.6974 df = 3, p-value = 0.0822

###TN
# descriptive statistic by group
describeBy(kw_data$TN,kw_data$Prefix)

#Using Kruskal-Wallis-Test, TN
kruskal.test(kw_data$TN~kw_data$Prefix)
# results: Kruskal-Wallis chi-squared = 15,625, df = 3, p-value = 0.001353

###Mercury (hg)
# descriptive statistic by group
describeBy(kw_data$hg,kw_data$Prefix)

# Using Kruskal-Wallis-Test, Hg
kruskal.test(kw_data$hg~kw_data$Prefix)
# results: Kruskal-Wallis chi-squared = 13,768 df = 3, p-value = 0.003238
```

```
###Delta13C
# descriptive statistic by group
describeBy(kw_data$Delta,kw_data$Prefix)

# Using Kruskal-Wallis-Test, Delta13C
kruskal.test(kw_data$Delta~kw_data$Prefix)
# results: Kruskal-Wallis chi-squared = 11,879 df = 3, p-value = 0,007808

### TOC/TN ratio
# descriptive statistic by group
describeBy(kw_data$`C/N ratio`,kw_data$Prefix)

# Using Kruskal-Wallis-Test, TOC/TN ratio
kruskal.test(kw_data$`C/N ratio`~kw_data$Prefix)
# results: Kruskal-Wallis chi-squared = 8.3055, df = 3, p-value = 0.0401

########################################
# Mann-Whitney-U test (each site) extract   #####

## required packages
library("psych")
library("readxl")

## information: S= SDLAG; L= TKL; D= DLB; U= UPL

## Load data (two sites per excel sheet)
data_SL <- read_excel(„/Data/path/SDLAG-TKL.xlsx“)
```

```
data_SD <- read_excel("/Data/pathSDLAG-DLB.xlsx")
data_SU <- read_excel(„/Data/path/SDLAG-UPL.xlsx")
data_LD <- read_excel(„/Data/path/TKL-DLB.xlsx")
data_LU <- read_excel(„/Data/path/TKL-UPL.xlsx“)
data_DU <- read_excel(„/Data/path/DLB-UPL.xlsx")

###TOCvol

## SDLAG <-> TKL
# calculate Mann-Whitney-U-Test
wilcox.test(TOCvol~Prefix, data = data_SL, exact = TRUE, correct = FALSE, conf.int = FALSE)
# p-value = 0.01086
## effect size
z_TOCvol_1 <- qnorm(0.01086/2)
z_TOCvol_1
# z = -2.547172
r_TOCvol_1 <- z_TOCvol_1/sqrt(49)
r_TOCvol_1
# r = 0.3638817

## SDLAG <-> DLB
# calculate Mann-Whitney-U-Test
wilcox.test(TOCvol~Prefix, data = data_SD, exact = TRUE, correct = FALSE, conf.int = FALSE)
# p-value = 1
```

```
## SDLAG <-> UPL
# calculate Mann-Whitney-U-Test
wilcox.test(TOCvol~Prefix, data = data_SU, exact = TRUE, correct = FALSE, conf.int = FALSE)
# p-value = 1

## TKL <-> DLB
# calculate Mann-Whitney-U-Test
wilcox.test(TOCvol~Prefix, data = data_LD, exact = TRUE, correct = FALSE, conf.int = FALSE)
# p-value = 0.008462
## effect size
z_TOCvol <- qnorm(0.008462/2)
z_TOCvol
# z = -2.633058
r_TOCvol <- z_TOCvol/sqrt(49)
r_TOCvol
# r = -0.3761511

## TKL <-> UPL
# calculate Mann-Whitney-U-Test
wilcox.test(TOCvol~Prefix, data = data_LU, exact = TRUE, correct = FALSE, conf.int = FALSE)
# p-value = 0.1791

## DLB <-> UPL
# calculate Mann-Whitney-U-Test
wilcox.test(TOCvol~Prefix, data = data_DU, exact = TRUE, correct = FALSE, conf.int = FALSE)
# p-value = 0.733
```

```
##############################################
# Mann-Whitney-U test (frozen/unfrozen) extract  #####

## Load data
fn_data <- read_excel(„/Data/path/frozen-unfrozen.xlsx“)

# information: group 0 = not frozen (water covered), group 1= frozen

###TOC

## descriptive statistic by groups
describeBy(fn_data$TOC,fn_data$Prefix)
# group 0: mean = 4.76 wt%, median = 5.1  ; group 1: mean = 4.75 wt%, median 3.17

## calculate Mann-Whitney-U-Test
wilcox.test(TOC~Prefix, data = fn_data, exact = FALSE, correct = FALSE, conf.int = FALSE)
# p-value = 0.007946
## effect size
z_TOC <- qnorm(0.007946/2)
z_TOC
# z = -2.654356
r_TOC <- z_TOC/sqrt(49)
r_TOC
# r = 0.3791937
```

```
##############################################
# Mann-Whitney-U test (saline/ not saline) extract  ####

## Load data
mw_data <- read_excel("/Users/friedaphilinegiest/Desktop/M_W_U_Test_sal_nsal.xlsx")

# information: group 0 = saline, group 1= not saline

###TOC

## descriptive statistic by groups
describeBy(mw_data$TOC,mw_data$Prefix)
# mean group 0 = 2.53 wt% ; group 1 = 6.04 wt%

## calculate Mann-Whitney-U-Test
wilcox.test(TOC~Prefix, data = mw_data, exact = FALSE, correct = FALSE, conf.int = FALSE)
# p-value = 0.005452
## effect size
z_TOC <- qnorm(0.005452/2)
z_TOC
# z = -2.779039
r_TOC <- z_TOC/sqrt(49)
r_TOC
#  r= 0.3970056
```

Acknowledgements

I carried out my master thesis at *Alfred Wegener Institute – Helmholtz Centre for Polar and Marine Research* and would like to start by thanking all my colleagues there, who made me feel welcome from day one and made writing my master's thesis a time that I will look back on with pleasure.

Many thanks go out to my supervisors Dr. Jens Strauss and Prof. Dr. Guido Grosse for their great support, for letting me know that I could always reach out when help was needed, and for the knowledge and experiences I was able to gain during my time at AWI.

A special thank you to my officemates: Maren Jenrich, Torben Windirsch, Fiona Giebeler and Verena Bischoff, for always supporting me mentally, but also with their expertise on minor and major issues that occurred.

Many thanks to Justin Lindemann for the introductions and help with the laboratory work.

A big thank you also to my family and friends, who have always supported me and kept up my confidence to get through difficult and stressful phases.

Eidesstattliche Erklärung

Hiermit versichere ich an Eides statt, dass ich die vorliegende Arbeit selbstständig und nur mit den angegebenen Quellen und Hilfsmitteln (z. B. Nachschlagewerke oder Internet) angefertigt habe. Alle Stellen der Arbeit, die ich aus diesen Quellen und Hilfsmitteln dem Wortlaut oder dem Sinne nach entnommen habe, sind kenntlich gemacht und im Literaturverzeichnis aufgeführt. Weiterhin versichere ich, dass weder ich noch andere diese Arbeit weder in der vorliegenden noch in einer mehr oder weniger abgewandelten Form als Leistungsnachweise in einer anderen Veranstaltung bereits verwendet haben oder noch verwenden werden. Die Arbeit wurde noch nicht veröffentlicht oder einer anderen Prüfungsbehörde vorgelegt.

Die „Richtlinie zur Sicherung guter wissenschaftlicher Praxis für Studierende an der Universität Potsdam (Plagiatsrichtlinie) - Vom 20. Oktober 2010“ ist mir bekannt.

Es handelt sich bei dieser Arbeit um meinen ersten Versuch.

Potsdam, den 15.11.2023

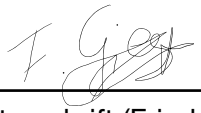

Unterschrift (Frieda Giest)

Einverständniserklärung

Ich erkläre mich damit einverstanden, meine schriftliche Arbeit (Master-) in elektronischer Form einzureichen. Ich bin damit einverstanden, dass die Arbeit mit Hilfe einer Plagiaterkennungssoftware einer Überprüfung unterzogen werden kann.

Potsdam, den 15.11.2023

Unterschrift (Frieda Giest)